Modeling of automotive structures using dynamic behaviour simulation software

André Filipe Botelho Pereira Pinto

Supervisors:

José César de Sá

Paulo Tavares de Castro

Sérgio M. O. Tavares

Faculdade de Engenharia da Universidade do Porto

A thesis submitted in partial fulfillment of the requirements for the degree of Master of Science in Mechanical Engineering

July 2013

Keywords

automotive engineering, crashworthiness, crash simulation, cross car beam, finite element method, modal analyses.

Abstract

This dissertation concerns the study of dynamical structural behaviour of cross car beams. For this purpose, the finite element method was used to assess the behaviour under impact conditions (crashworthiness) and the modal analysis of the structure, relevant for noise vibration and harshness (NVH) assessement. As a case study for this type of analyses, a real cross car beam design of a mass production car was studied in detail. The CAD file was supplied by SODECIA in the framework of joint FEUP-SODECIA research and development project.

The work begins with a discussion of the state of the art of cross car beam technology, where the several alternatives concerning materials, fabrication processes and design of strutural connections are briefly mentioned. This is followed by a concise presentation of the fundamental equations that govern the two phenomena studied. The objective of the dissertation was achieved using the PAM-CRASH software package for crashworthiness and NVH analyses. Before dealing with the real case, an effort was made to evaluate the performance of finite element method software packages, as concerns the influence of certain modeling strategies upon the quality of the computed results. In particular, the influence of mesh refinement and element type was studied using academic benchmark cases with well known theoretical solution, namely the plate with a central circular hole subjected to remote tensile loading, and the center-cracked plate also subjected to remote tensile loading. This preliminary work was carried out in Abaqus. This software was also used in initial linear elastic static analyses of simplified cross car beam conceptual designs.

For the real case studied in this dissertation there was no numerical modeling available (other than the already mentioned CAD file). The only information supplied consisted of performance requirements stated by the car manufacturer for NVH performance; no technical information was available concerning crashworthiness. In these circumstances the author of the present thesis adapted the requirements for other mass production cars of the same category, as regards dynamic loading including g-forces resulting from deceleration. Although the unavailability of published results for this particular cross car beam model prevents a comparison of the present results, the trends and order of magnitude of the several analyses performed are within expectation for this type of product. The present work is further confirmation of the interest of numerical modeling as a first step before actual experimental testing, saving time and money.

Resumo

Esta dissertação trata o problema do comportamento estrutural dinâmico de uma *cross car beam.* Para este efeito usou-se o método dos elementos finitos para avaliar o comportamento em condições de impacto (*crashworthiness*) e para levar a cabo a análise modal relevante para as avaliações NVH (*noise vibration and harshness*). Como caso de estudo para este tipo de análises foi usada uma *cross car beam* de um veículo de produção em massa. A respectiva documentação CAD foi disponibilizada pela empresa SODECIA no quadro de um projecto de investigação e desenvolvimento levado a cabo pela FEUP e pela SODECIA.

O trabalho inicia-se com uma discussão do estado da arte da tecnologia de *cross car beams* em que várias alternativas relativas a materiais, processos de fabrico e concepção de ligações estruturais são concisamente mencionadas. Segue-se uma resumida apresentação das equações fundamentais que governam os fenómenos estudados. Os objectivos da dissertação foram atingidos usando o software PAM-CRASH para as análises de impacto e NVH. Antes do tratamento do caso real de estudo, foi dedicada atenção à avaliação do desempenho de software comercial do método dos elementos finitos no que diz respeito à influência de estratégias de modelação na qualidade dos resultados. Em particular, a influência do refinamento da malha e do tipo de elemento foi examinada usando casos de comparação académicos, de solução teórica bem conhecida, designadamente a placa com furo circular central remotamente traccionada e a placa contendo uma fenda central, também sujeita a carregamento remoto de tracção. Este trabalho preliminar foi levado a cabo usando Abaqus, software com o qual também foram realizadas análises preliminares estáticas, no domínio linear elástico, de modelos conceptuais muito simplificados de *cross car beams*.

Para o caso real estudado nesta dissertação não existia um modelo numérico disponível (para além do ficheiro CAD já referido). A única informação fornecida consistiu nas especificações do fabricante da viatura relativas ao desempenho NVH; não foi fornecida qualquer informação relativa a *crashworthiness.* Nestas circunstâncias, o autor da presente tese adaptou especificações conhecidas relativas a um outro veículo da mesma gama, no tocante a carregamento dinâmico incluindo forças g resultantes da desaceleração. Embora a indisponibilidade de resultados publicados para esta *cross car beam* inviabilize comparações directas dos presentes resultados, as tendências e ordens de grandeza encontradas nas várias análises levadas a cabo estão dentro das expectataivas para este tipo de produto. O trabalho apresentado é mais uma contribuição para reforçar o interesse de simulações numéricas antes dos indespensáveis ensaios experimentais, poupando tempo e dinheiro.

Contents

Abstract v

List of Figures xi

List of Tables xvii

List of Acronyms xix

List of Symbols xxi

Chapter 1 Introduction 1
- 1.1 Product presentation . . . 1
- 1.2 Background . . . 2
  - 1.2.1 Crashworthiness . . . 2
  - 1.2.2 Crash test . . . 3
  - 1.2.3 Chronology of car crash simulation . . . 6
- 1.3 SODECIA company presentation . . . 7
- 1.4 Development and research of the cross car beam BV226 model behaviour in crash . . . 8
- 1.5 Organization and topics addressed in the present report . . . 8

Chapter 2 State of the art: engineering 9
- 2.1 General presentation of the CCB, in the context of a vehicle structure . . . 9
  - 2.1.1 Introduction . . . 9
  - 2.1.2 Load carrying car structure; the BIW (body in white) . . . 10
  - 2.1.3 The CCB . . . 13
  - 2.1.4 Crashworthiness and NVH . . . 15
  - 2.1.5 Recycling . . . 15
- 2.2 Concise reference to materials of interest for CCB's . . . 15
  - 2.2.1 Materials . . . 15
  - 2.2.2 Steels . . . 18
  - 2.2.3 Aluminium . . . 18
  - 2.2.4 Magnesium . . . 19
  - 2.2.5 Metallic Foams . . . 21
  - 2.2.6 Plastics . . . 22
  - 2.2.7 Composites . . . 23
- 2.3 Brief reference to some of the relevant technologies . . . 24
  - 2.3.1 Hydroforming . . . 24
  - 2.3.2 Welding . . . 24
- 2.4 Industrial engineering aspects and LCA . . . 24
  - 2.4.1 Inspection . . . 24
  - 2.4.2 LCA – recycling . . . 25
  - 2.4.3 Supply chain management . . . 26

Chapter 3 Theoretical focus: related literature **27**
3.1 Crash analysis . . . 27
3.1.1 Dynamic equations . . . 28
3.1.2 Response history: direct integration methods . . . 29
3.1.3 Explicit analysis *vs* implicit analysis . . . 30
3.1.4 Explicit simulation . . . 31
3.2 Modal analysis . . . 34
3.2.1 Implicit simulation . . . 34
3.2.2 Free dynamic vibration - real eigenvalues . . . 34
3.2.3 Eigen extraction with implicit analysis . . . 36
3.3 Shell elements . . . 37
3.3.1 Reduced and selective integration . . . 37
3.3.2 Hourglassing . . . 37
3.4 PAM-CRASH constraints . . . 38
3.4.1 Rigid bodys . . . 38
3.4.2 Multiple to one node constraint . . . 38

Chapter 4 FEM Software **39**
4.1 Abaqus . . . 39
4.1.1 Benchmark cases . . . 40
4.1.2 Cross car beam concepts analysis . . . 53
4.2 PAM-CRASH . . . 60
4.2.1 Solution phase . . . 61
4.2.2 Crash analysis . . . 64
4.2.3 Modal analysis . . . 64
4.2.4 Benchmark cases . . . 65
4.2.5 PAM-CRASH pre- and post-processing software . . . 65

Chapter 5 Case study **69**
5.1 Case study description . . . 69
5.2 Background information . . . 70
5.3 Problem data and description . . . 70
5.3.1 Parts list . . . 70
5.4 Model pre-processing . . . 71
5.4.1 Shell mesh generation in ANSA . . . 73
5.4.2 Weld beads generation . . . 79
5.4.3 Constraints definition . . . 81
5.4.4 Loads and boundary conditions definition . . . 83
5.4.5 Material law definition . . . 88
5.4.6 Control cards . . . 90
5.4.7 Modal analysis model: explicit to implicit advisor . . . 92

Chapter 6 PAM-CRASH Results **103**
6.1 Crash simulation results . . . 103
6.2 Modal analysis results . . . 116

Chapter 7 Concluding remarks and suggestions for future work **123**

References **125**

List of Figures

1.1 Cross car beam assembly, [1]. 2
1.2 Cross car beam from Brazilian Ford Fiesta, [2]. 2
1.3 Audi Q3, 64 km/h frontal impact with offset deformable barrier, [3]. 3
1.4 EuroNCAP frontal impact test, [4]. 4
1.5 Small overlap fronteal test configuration, [5]. 4
1.6 EuroNCAP pole side impact test, [6]. 5
1.7 Audi Q3 pole side impact at 29 km/h, [3]. 5
1.8 EuroNCAP car to car side impact, [7]. 6
1.9 Audi Q3 side impact with mobile deformable barrirer at 50 km/h, [3]. . . . 6
1.10 1984 Volkswagen Polo, [8]. 7
1.11 25000 elements model, [8]. 7
1.12 2001 Audi A4 model, [8]. 7

2.1 Material composition of the average typical instrument panel of a midsized vehicle, [9]. 10
2.2 Simplified model of the structure of a standard sedan (saloon), [10]. 11
2.3 Load cases for the global structure, [11]. 12
2.4 Body steel selection for GM Chevrolet Sonic, [12]. 16
2.5 Cross car beam of a FIAT Marea, [13]. 20
2.6 Dash board panel carrier of a Mini (a BMW product), [13]. 21
2.7 Design of the magnesium IP cross car beam and console top, [14]. 21
2.8 The hydroforming principle, [15]. 24
2.9 Instrument panel carrier for automotive dashboards; source Havrilla, 2010. 25
2.10 Stamped steel CCB; the zoom shows a close up of one of 46 clips, [16]. . . 25

3.1 Renault Megane crash simulation. [17] 27
3.2 Explicit time integration, [8]. 32
3.3 Shell element time steps, [17]. 34
3.4 Shell element stringent time steps, [17]. 34

4.1 Plate dimensions in mm. 40
4.2 Plate boundary conditions. 41
4.3 Plate first 10 mode shapes. 42
4.4 Wall dimensions in m. 43
4.5 Wall boundary conditions and load applied. 43
4.6 Dynamic Load amplitude definition in Abaqus. 44
4.7 Wall points displacement magnitude during the blast. 45
4.8 The three modes of cracking, [18]. 46
4.9 Center-cracked plate with finite width W, loaded in mode I. 46
4.10 Loads and boundary conditions of the 1/4 plate model. 47
4.11 Shell mesh used in analysis n°5. 47
4.12 Infinite Plate with collinear cracks, [18]. 48
4.13 Stresses on the edges of strip cut from infinite plate with collinear cracks, [18]. 48
4.14 Finite width corrections for center cracked plate, [18]. 49
4.15 Percentage difference evolution with mesh configuration of the finite center-cracked plate stress intensity factor determined by FEA in Abaqus, logaritmic scale. 49
4.16 Percentage difference evolution with mesh configuration of the finite center-cracked plate stress intensity factor determined by FEA in Abaqus. 50
4.17 Plate dimensions in mm. 50
4.18 Schematic illustration of the stress concentration factor in an infinite plate with a central circular hole, subjected to a traction load in the y-drirection, [19]. 51
4.19 Load, boundary conditions and seeds guidelines of the 1/4 plate model. . . 51
4.20 1/4 central hole plate shell mesh. 52
4.21 1/4 central hole plate stress distribution in y-direction. 52
4.22 1/4 central hole plate stress distribution in x-direction. 53
4.23 Refined zone of the 1256 shell elements mesh. 53
4.24 Refined zone of the 26506 shell elements mesh. 54
4.25 Elements defined by 2 pairs of seeds with equal length (highlighted). . . . 54
4.26 Stress values percent error behaviour with mesh configuration for the present plate with a hole example. 55

4.27 Results percent error in function of the greatest length of the elements located in points *A* and *B*. 56
4.28 Simplified concept geometry and dimensions. 56
4.29 First model solid mesh. 57
4.30 Loads and boundary conditions of the solid meshed model. 57
4.31 von Mises stress distribution (Pa) along the first model solid meshed structure. 58
4.32 First model shell mesh. 58
4.33 Loads and boundary conditions of the shell meshed model. 59
4.34 von Mises stress distribution (Pa) along the first model shell meshed structure. 59
4.35 Second concept model of the cross car beam. 60
4.36 Second model solid mesh. 60
4.37 Loads and boundary conditions of the second model concept. 61
4.38 von Mises stress distribution (Pa) along the second concept structure - isometric view. 61
4.39 von Mises stress distribution (Pa) along the second concept structure - frontal view. 62
4.40 von Mises stress distribution (Pa) along the second concept structure -top view. 62
4.41 Natural shapes of the first four natural modes of the second model concept. 63
4.42 PAM-CRASH simulation,[3]. 63
4.43 PAM-CRASH solution phase, [8]. 64

5.1 BV226 CCB, source: SODECIA. 69
5.2 FEP 13 hardening curve. 71
5.3 First step. 73
5.4 Quality criteria window. 74
5.5 Material definition. 75
5.6 Part manager. 75
5.7 Geometry check. 76
5.8 Irregular cross interference. 77
5.9 Hole feature usefull help in meshing. 78
5.10 Hole correction. 78

5.11 A-PILLAR LHS meshing steps. 80
5.12 Seam Lines of all CCB structure. 80
5.13 Weld bead mesh definition. 81
5.14 Steering column COG. 83
5.15 Steering wheel-airbag assembly COG. 83
5.16 Heaterbox COG. 84
5.17 Fixing points of the heaterbox to the CCB. 84
5.18 Passenger's airbag rigid body. 86
5.19 Steering column *MTOCO*. 87
5.20 CCB constraints. 87
5.21 CCB boundary conditions location. 88
5.22 Fixed elements of the bolted area. 88
5.23 A-pillar y-direction load. 89
5.24 A-pillar moment. 90
5.25 Steering wheel loading. 91
5.26 HVAC loading point of application. 91
5.27 HVAC loading. 92
5.28 SMBC loading point of application. 92
5.29 HVAC loading. 93
5.30 Passenger's airbag loading. 94
5.31 FE model material law definition in PAM-CRASH. 94
5.32 Control cards. 95
5.33 TCTRL card. 95
5.34 Crash simulation model. Rigid bodys are defined in blue, fixed boundary conditions are defined in green and *MTOCO*s are defined in pink as well as loads vectors. 98
5.35 *Explicit to Implicit Advisor* window. 99
5.36 Four nodal points spring's direction definition. 99
5.37 6 DOF spring with linear stiffness boundary condition setting. 100
5.38 Spring material editor. 101
5.39 Modal analysis model. 101
5.40 EIGEN control card. 102

6.1 Nodal displacement magnitude during crash simulation. 107

6.2 von Mises stress distribution during crash simulation. 111
6.3 Maximum plastic strain during crash simulation. 115
6.4 CCB global energy balance during crash simulation. 116

List of Tables

2.1 Material property comparisons, [20]. 17
2.2 Comparative properties of Al alloys and SMC composites, [20]. 17
2.3 Comparison of basic data for several steels (DP – dual phase; HSLA - precipitation hardened HSLA high-strength low-alloy steels), [21]. 18

4.1 Data and results of the stress intensity factor determination for a finite width center-cracked plate by FEA in Abaqus. 66
4.2 Study of the plate with hole stress values percent error behaviour with mesh configuration - data and results. 67

5.1 FEP13 steel plastic behaviour, [22]. 71
5.2 BV226 parts list. 72
5.3 Passenger's airbag assembly COG, first cardan coordinates and A-pillar LHS loading point of application. 82
5.4 Mass and inertia properties of all the relevant attached components to CCB structure considered in the present analysis. 85
5.5 A-pillar loading. 86
5.6 Steering wheel loading. 89
5.7 First cardan loading. 96
5.8 HVAC loading. 97
5.9 SMBC loading. 97
5.10 Passenger's airbag loading. 97
5.11 CCB accelaration fields. 98
5.12 Localized body stiffness, ... 98

6.1 CCB model with localized stiffness first two modal shapes. 117
6.2 CCB model with localized body stiffness third and fourth modal shapes. . 118
6.3 CCB model with fixed boundary conditions first two modal shapes. 119
6.4 CCB model with fixed boundary conditions third and fourth modal shapes. 120

List of Acronyms

ABS	acrylonitrile butadiene styrene
AMLS	automated multilevel substructuring
AVI	automated visual inspection
BFI	body frame integral
BIW	body in white
BMC	bulk molding compound
BOF	body on frame
BRIC	Brasil, Russia, India, China
CAD	computer aided design
CAE	computer aided engineering
CCB	cross car beam
CFRP	carbon fiber reinforced polymers
CIRP	College International pour la Recherche en Productique
COG	center of gravity
CPU	central processing unit
DOF	degrees of freedom
ELV	end-of-life vehicle
EuroNCAP	European New Car Assessment Program
FBHP	front body hinge pillars
FE	finite element
FEA	finite element analysis
FEM	finite element method
FEUP	Faculdade de Engenharia da Universidade do Porto
FMVSS	Federal Motor Vehicle Safety Standards
FRP	fiber-reinforced polymer
GFRP	glass-fiber reinforced polymer
HDPE	high density polyethylene
HSLA	high-strength low-alloy steel
HVAC	heating, ventilation, and air conditioning
IP	instrument panel

IRAM	implicitly restarted Arnoldi method
LCA	life cycle analysis
LDPE	low density polyethylene
LHS	left hand side
NCAP	New Car Assessment Program
NVH	noise, vibration and harshness
OEM	original equipment manufacturer
PC	polycarbonate
PC GFlO	polycarbonate glass fiber 10% by weight
PET TS	polyethylene terephthalate thermoset
PF TS	phenol-formaldehyde thermoset
PNGV	Partnership for a New Generation of Vehicles
PP	polypropylene
PP GF30	polypropylene glass fiber 30% by weight
PPE	polyphenylene ether
PU	polyurethane foam
PVC	polyvinylchloride
QREN	Quadro de Referência Estratégica Nacional
RHS	right hand side
SAE	Society of Automotive Engineers (USA)
SMA	styrene maleic anhydride
SMC	sheet molding compound
SRIM	structural reaction injection moulding
SUVs	sport utility vehicles
TMS	The Mineral, Metals and Material Society
USA	United States of America

List of Symbols

Latin variables

a	half length of a crack
d	vector defined by nodes n_i and n_d
E	Young's modulus
J	J integral
k	stiffness
m	mass
n_d	dependent node
n_i	independent node
NU	PAM-CRASH Poisson coefficient parameter
RHO	PAM-CRASH density parameter
U	displacement
W	plate width

Greek variables

ε	strain
θ	rotation
ν	Poisson coefficent
ξ	damping ratio
ρ	density
σ	stress
ω_i	i th natural frequence

Acknowledgements

The author wishes to thank several people. I would like to thank all my room colleagues, specially Daniel Braga, Daniel Peixoto, João Dias and Jaime Rodrigues that gave me a great help during this thesis period. Furthermore I would also like to thank my parents for their support and love. I would like to thank my supervisors (Professors José César de Sá, Paulo Tavares de Castro and Sérgio M. O. Tavares) for their assistance and guidance with this work. Last but not least, I would like to thank SODECIA and the SODECIA - Centro Tecnológico team, specially Eng. Eduardo Santos and my supervisor at SODECIA during my stays there, Eng. Paulo Gomes, for giving me precious information regarding the cross car beam and their know-how in crash simulation and modal analysis.

This work is part of the QREN project 23032 “CCB360” financed by European Regional Development Fund - ERDF through “COMPETE - Programa Operacional Factores de Competitividade”.

Introduction

Analysis of structural dynamic behaviour with finite element method (FEM) software is the present thesis area of research. These analyses are of extreme importance to automotive manufacturers. Among the many sets of dynamic analyses performed in multiple vehicle components, crash simulation and noise, vibration and harshness (NVH) analysis are, these days, crucial to any new vehicle development program.

Crash simulation is a virtual recreation of the destructive and costly crash tests. Its main objective is to evaluate crashworthiness of car components, primarily in components that play a crucial role in the vehicle's occupants safety. One of these crucial components is the vehicle's cross car beam. This structure is the present thesis object of study.

Automakers use crash simulation during CAE analysis for crashworthiness in the CAD process of modelling new cars. The main benefit of this simulation is that crash tests can be quickly and inexpensively performed by a computer, which allows optimization of the design before a real prototype of the car has been produced. Therefore, project problems can be solved before spending time and money in real crash tests.

NVH analysis is the study and treatment of vehicles noise and vibration characteristics. Cross car beam play also an important role in this area as they support the steering column, cause of unconfortable vibrations transmission to the vehicle driver and its occupants.

The present thesis concerns the use of numerical modeling solutions using PAM-CRASH software to validate the design of a cross car beam made of welded steel for mass production of small vehicles.

The cross car beam used was the model BV226 from Brazilian Ford Fiesta. Its CAD geometry as well as other crucial elements for its modelling like material properties, mass and inertial properties of the linked components, boundary conditions, technical specifications, etc., were provided by Sodecia - Centro Tecnológico SA.

1.1 Product presentation

The cross car beam (CCB), see *e.g.* Figure 1.1 and Figure 1.2, is a vehicle structure that usually supports all instrument panel components and systems including the fusebox, the heaterbox of the HVAC system, steering column, radio, passenger airbag, pedals, electric wiring, navigation system and many other components and systems, [1]. Cross car beams have a very important role in car crash performance by avoiding or minimizing the intrusion of foreign elements in the car cabin, *e.g.*, powertrain, [2]. Last but not least, this struture should also avoid the transmission of unwanted noise and vibration to the vehicle's driver and occupants.

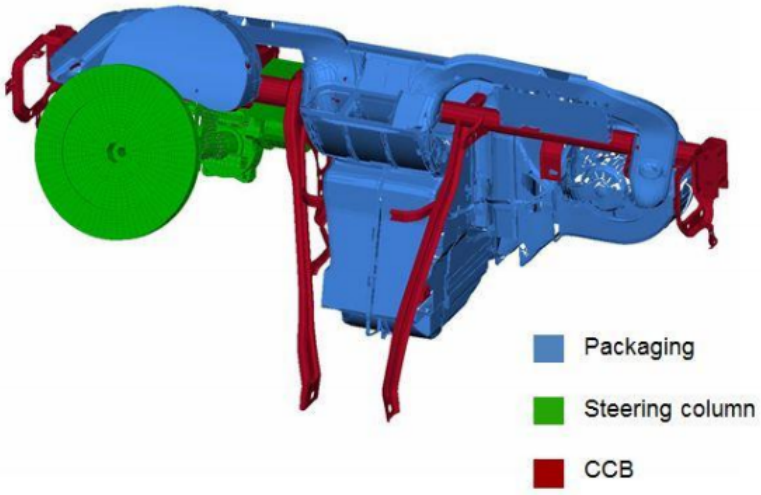

Figure 1.1: Cross car beam assembly, [1].

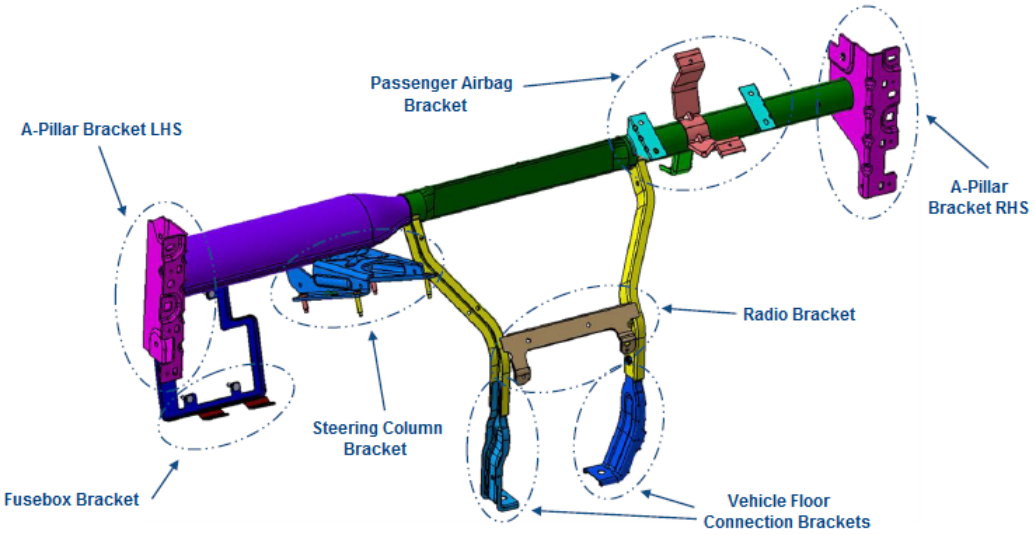

Figure 1.2: Cross car beam from Brazilian Ford Fiesta, [2].

1.2 Background

The use of automobile is by far the most dangerous mode of transportation. In 2008, European roads witnessed 39000 deaths. This number impresses but when compared with 2001 numbers, 54000 deaths, we noticed a downward trend. EU goal is to level the numbers at the 27000 deaths patamar. One of EU priorities in road safety policy is to improve cars safety through technological solutions, [2].

1.2.1 Crashworthiness

One important caracteristic during the design of any automotive structure is its crashworhiness. This attribute defines the ability of a structure to protect its occupants during an impact. This is commonly tested when investigating the safety of aircraft and vehicles, [23].

In a car structure the front, rear and side structures have been developed over the years to provide some impact attenuation and to maintain passenger compartment integrity. Instrument panels are a major source of injury due to lethal projections, sharp corners, and lack of padding, [23].

Depending on the nature of the impact and the vehicle involved, different criteria are used to determine the crashworthiness of the structure. Crashworthiness may be assessed either prospectively, using computer models or experiments, or retrospectively by analyzing crash outcomes. Several criteria are used to assess crashworthiness prospectively, including the deformation patterns of the vehicle structure, the acceleration experienced by the vehicle during an impact, and the probability of injury predicted by human body models.

1.2.2 Crash test

Crash tests are used to find safety issues and test solutions to make cars safer and reduce injuries and deaths from car accidents. This destructive test is usually performed to ensure safe design standards in crashworthiness and crash compatiblility for various modes of transportation or related systems and components.

Types of crash test

- **Frontal-impact tests**: This impact is intended to represent the most frequent type of road crash, resulting in serious or fatal injury. It simulates one car having a frontal impact with another car of similar mass. EuroNCAP performs this tests at 64 km/h with a car striking a deformable barrier, Figure 1.3 and 1.4. The test speed of 64 km/h represents a car to car collision with each car travelling at around 55 km/h. There are usually impacts upon a solid concrete wall at a specified speed, but can also be vehicle-vehicle tests. SUVs have been singled out in these tests for a while, due to high ride-height that they often have, [4, 5].

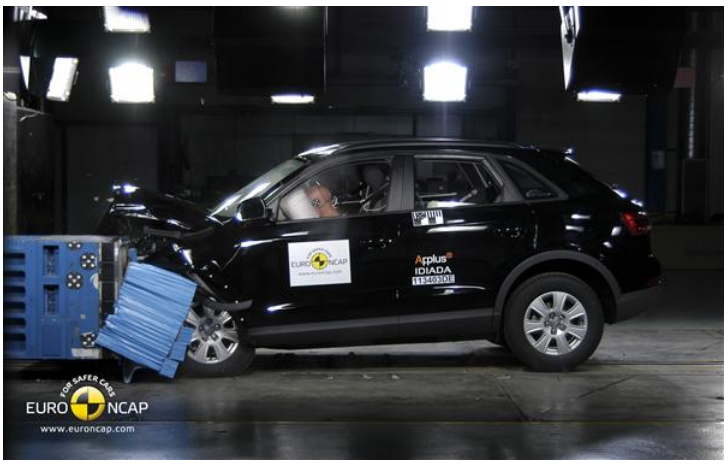

Figure 1.3: Audi Q3, 64 km/h frontal impact with offset deformable barrier, [3].

- **Offset tests**: in which only part of the front of the car impacts with a barrier (vehicle). These are important, as impact forces remain (approximately) the same as with a frontal impact test, but a smaller fraction of the car is required to absorb all of the force. These tests are often realized by cars turning into oncoming traffic. EuroNCAP frontal impact test, Figure 1.4, uses 40% of the width of the widest part of the car, [4, 5].

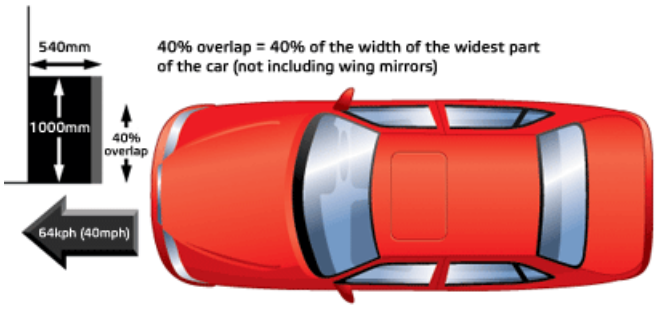

Figure 1.4: EuroNCAP frontal impact test, [4].

- **Small Overlap tests**: In this test only a small portion of the car's structure strikes an object such as a pole or a tree. This is the most demanding test. These are usually conducted with a overlay of 15-20% of the front vehicle structure, Figure 1.5, [5]. Furthermore, EuroNCAP also performs a pole side impact test to encourage manufactureres to fit head protection devices. Side impact head or curtain airbags help to protect the head and upper torso by providding a padding effect and by preventing the head from passing the window opening. To perform this test, the car is propelled sideways at 29km/h into a rigid pole, Figure 1.6 and 1.7, [6].

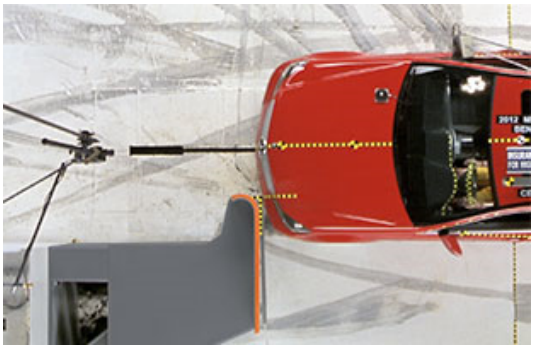

Figure 1.5: Small overlap fronteal test configuration, [5].

- **Side-impact tests**: this type of accidents has a very significant likelihood of fatality, as cars do not have a significant crumple zone to absorb the impact forces before an occupant is injured. Side crashes account for about a quarter of passenger vehicle occupant deaths in the United States, [24]. EuroNCAP performs a car to car side impact test, Figure 1.8 and 1.9, and classifies it as the second most important one. This test

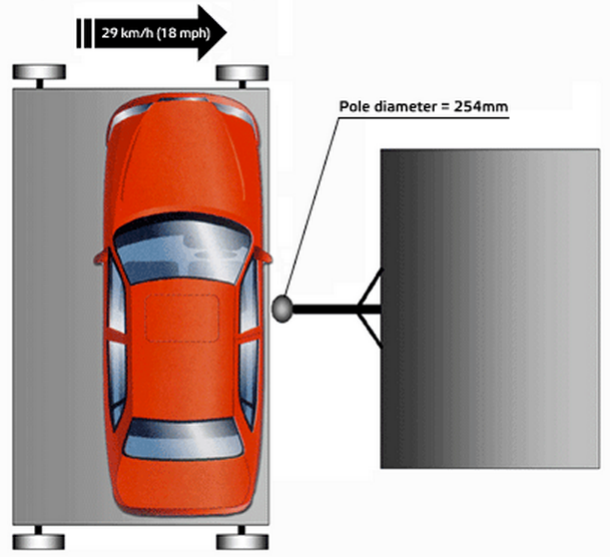

Figure 1.6: EuroNCAP pole side impact test, [6].

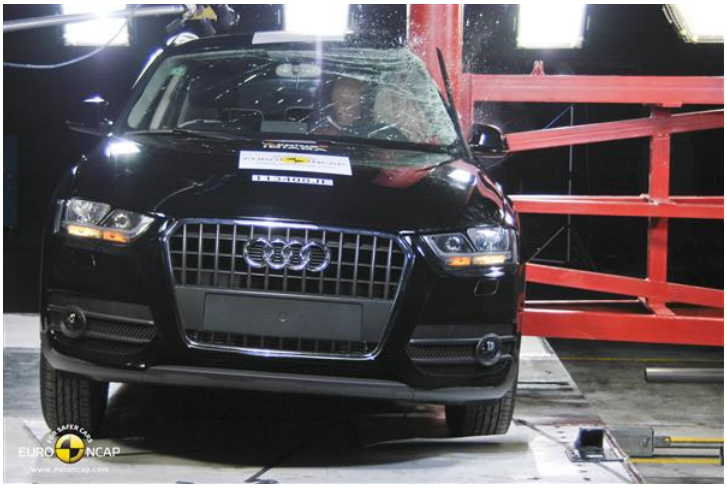

Figure 1.7: Audi Q3 pole side impact at 29 km/h, [3].

is simulated by having a mobile deformable barrier impacting the driver's door at 50 km/h, [7].

- **Roll-over tests**: which tests a car's ability (specifically the pillars holding the roof) to support itself in a dynamic impact. More recently dynamic rollover tests have been proposed as opposed to static crush testing, [25].
- **Roadside hardware crash tests**: are used to ensure that crash barriers and crash cushions will protect vehicle occupants from roadside hazards, and also to ensure that guard rails, sign posts, light poles and similar equipment do not pose an undue hazard to vehicle occupants.
- **Old versus new**: Often an old and big car against a small and new car, or two different generations of the same car model. These tests are performed to show the advancements in crashworthiness.

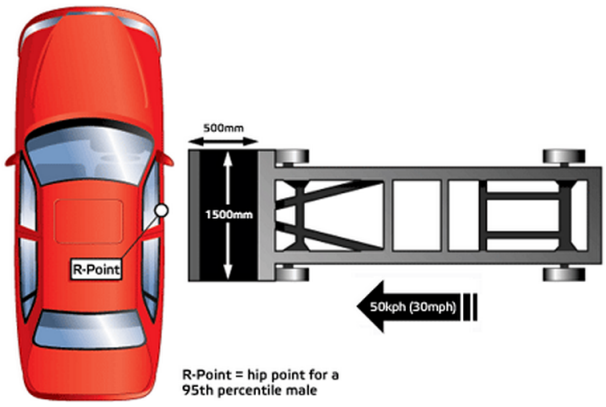

Figure 1.8: EuroNCAP car to car side impact, [7].

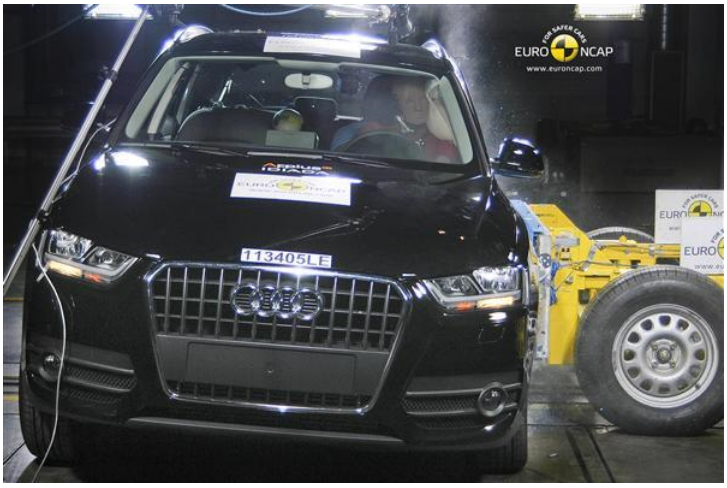

Figure 1.9: Audi Q3 side impact with mobile deformable barrirer at 50 km/h, [3].

- **Computer model**: Because of the cost of full-scale crash tests, engineers often run many simulated crash tests using computer models to refine their vehicle or barrier designs before conducting live tests.

The crash test performed by the computer model of this report trys to replicate the effects of a crash of an offset frontal crash test in the CCB structure.

1.2.3 Chronology of car crash simulation

- 1960 : Lumped mass/ spring models (in-house codes), [8];
- 1984 : Volkswagen Polo ~5.000 elements, Figure 1.10, [8];
- 1987 : First full-scale crash simulation of a car, [26];
- 1990 : ~25.000 elements, Figure 1.11, [8];
- 2001 : ~500.000 elements, Figure 1.12, [8];
- 2010+ : ~1.500.000 elements, [8].

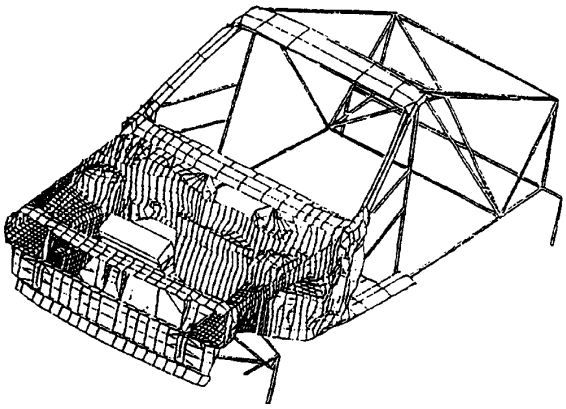

Figure 1.10: 1984 Volkswagen Polo, [8].

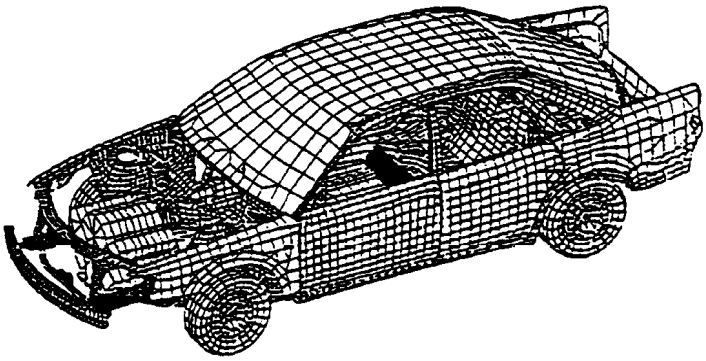

Figure 1.11: 25000 elements model, [8].

1.3 SODECIA company presentation

This work was performed in the context of the project "Car Cross Beam 360º" promoted by Sodecia with the cooperation of Faculty of Engineering of the University of Porto. SODECIA is an industrial corporation operating worldwide as a full service supplier in the chassis, power-

Figure 1.12: 2001 Audi A4 model, [8].

train and body in white commodities. As a partner of the world's major OEM's, SODECIA aims to deliver integrated product solutions to meet the highest demands of our customers, by constantly adding value to their challenges, exceeding their expectations and taking part in their success, [27].

1.4 Development and research of the cross car beam BV226 model behaviour in crash

The main focus of this thesis is the crashworthiness and NVH analyses of an existing CCB - the BV226 model used in Brazilian Ford Fiesta - using state-of-the-art software that was not available at the time of the original design of the mentioned structural component.

The software used is PAM-CRASH. Modeling starting point was the original CAD geometry .igs file. Two models were developed. The first one was developted for crash simulation. The second one derived from the first one completed, adding the necessary changes to performe modal analysis. The model mesh was generated in ANSA software. Definition of constraints, loads, boundary conditions and material behaviour was accomplished in Visual-Crash PAM pre-processor software. The two analysis were performed in different codes, crash simulation was performed in PAM-CRASH explicit solver, whereas modal analysis was performed in its implicit solver.

1.5 Organization and topics addressed in the present report

This thesis is composed of 7 chapters that address multiple topics in order to use numerical tools in a successful way for the design of a component of a vehicle body in white (BIW).

The second chapter describes the state of the art in cross car beam engineering. This is followed by a concise presentation in chapter 3 of fundamental equations of the phenomena studied. Because the finite element method is used, the fourth chapter consists of a discussion of modeling strategies using a few benchmark cases with well known theoretical solution. This chapter ends with some preliminary analyses of conceptual simplified cross car beams using Abaqus. The next chapters 5 and 6 present the main component of this dissertation, where a real Brazilian Ford Fiesta BV226 cross car beam model is studied in detail, as regards crashworthiness and NVH.

Finally, concluding remarks and suggestions for further work are presented.

State of the art: engineering

2.1 General presentation of the CCB, in the context of a vehicle structure

2.1.1 Introduction

The instruments panel (IP) of a car is typically located over a structural element called the cross car beam (CCB), linking the two front pillars of the vehicle, the so called A-pillars. In some cases the cross car beam is not used because the instrument panel itself is structural, *i.e.*, it provides the necessary strength, stiffness and other relevant properties, as discussed, *e.g.,* by Slik, [28]. Although the elimination of the conventionally used cross car beam is an option, most cars do use that component as part of the load carrying structure. The present thesis concerns the use of numerical modeling solutions to validate the design of a cross car beam made of welded steel for mass production small vehicles.

Aims of the analysis are derived from the requirements of the market. These include usability so that the driver is not exposed to inadequate vibration in service, and crash behavior in order to guarantee safety in conditions of accident (passive safety).

In order to limit vibrations, a minimum natural frequency for the instrument panel is aimed at in the design stage, with 30 Hz as a typical lower bound. Higher values, in the range 35-40 Hz, may be desirable as these higher values increase driver comfort. The relevant numerical analyses are implicit approaches to compute natural modes of vibration, and these were carried out in this thesis using the Abaqus and PAM-CRASH software .

On the other end, crash behavior – crashworthiness – is the object of experimental testing, *e.g.,* the European New Car Assessment Program (EuroNCAP), and numerical modeling is of great importance to avoid the huge costs of performing tests on inadequate structural solutions. Numerical modeling is used in the design stage so that the crash behavior is adequately predicted and therefore testing is made to confirm expectations of performance. The software LS DINA is very frequently mentioned in this context, as in Deb, [29], Lam, [30], Tabacu, [31], or Li, [14]; in the present work PAM-CRASH was used instead.

The complexity of automotive systems and subsystems such as the IP is suggested by the list of materials involved. Keoleian, [9], presents the material percent composition of a typical, average instrument panel, Figure 2.1. This indicates that for the CCBs considered, although steel was the preponderant single material, plastic resins comprised 68% of the total mass. The relative amount of plastics in IPs is much higher than in the total automobile.

This literature review will show that although steel is a common material choice for the CCB, as considered in the paragraph above, other materials are possible choices and are indeed currently used.

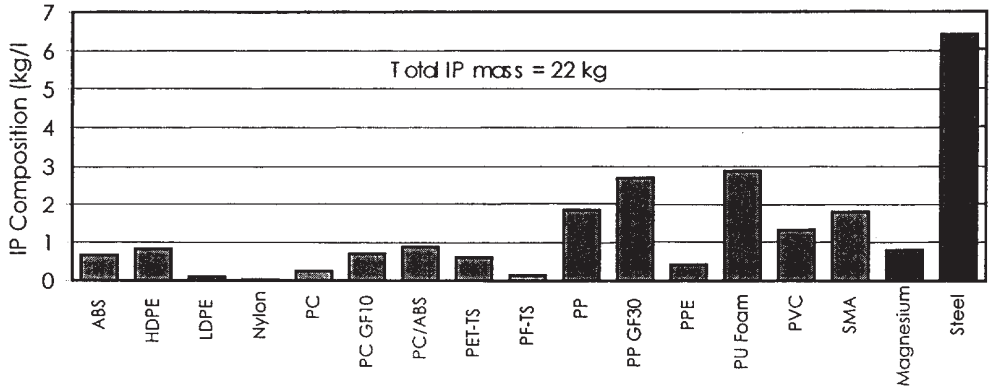

Figure 2.1: Material composition of the average typical instrument panel of a midsized vehicle, [9].

The literature review presented here was based mainly in a search of journal articles, particularly those of Elsevier[1], Springer[2], Wiley[3] and Taylor and Francis[4] . Efforts were made to also include publications of the Society of Automotive Engineers (SAE), obviously a very important source of information for this matter, but these efforts were hampered by the unavailability of free access to that source in FEUP. Nevertheless, some relevant papers from SAE are discussed.

Other documents of this project will include reference to patents search; this type of technical literature will not however be included here, for conciseness.

2.1.2 Load carrying car structure; the BIW (body in white)

Before focusing on the CCB, it is desirable to have a concise picture of the load carrying car structure. Figure 2.2 shows an hugely simplified model of the structure of a standard sedan (saloon), showing the base line load paths.

The baseline model includes floor, roof, side-frames, front and rear bulkheads and windscreen. For simplicity, all of these surfaces are assumed to be plane.

1. Transverse floor beam (front) carrying the front passengers.
2. Transverse floor beam (rear) carrying the rear passengers.
3. Inner wing panels carrying the power-train and supported by the front suspension.
4. *idem*
5. Dash panel–transverse panel between passengers and engine compartment.
6. Front parcel shelf.

[1] http://www.sciencedirect.com/

[2] http://link.springer.com/

[3] http://onlinelibrary.wiley.com/

[4] http://www.tandfonline.com/

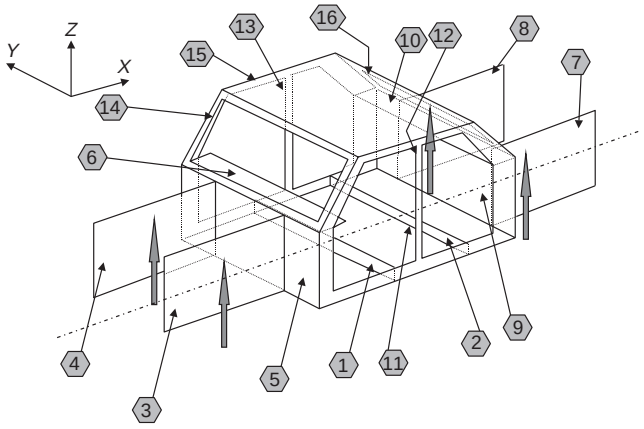

Figure 2.2: Simplified model of the structure of a standard sedan (saloon), [10].

7. Rear quarter panels carrying luggage loads and supported by the rear suspension.
8. *idem*
9. Panel behind the rear seats.
10. Rear parcel shelf.
11. Floor panel.
12. Left-hand and right-hand sideframes.
13. *idem*
14. Windscreen frame.
15. Roof panel.
16. Backlight (rear window) frame.

The cross car beam will be a part of item 6 of the list provided by Brown, [10], and reproduced above.

Load cases for the global structure include the basic ones schematically described in the Figure 2.3 . The analyses of the global structure will not however be the object of further attention in this thesis. The work presented is concerned with the CCB, and the design of this component is constrained by boundary conditions that are specified by the car manufacturer.

The basic architecture of the load carrying structure suffered a great evolution, from the independent chassis supporting an independent bodywork (body on frame construction or BOF), to backbone tube as in the original Lotus Elan, to tubular structures as in the classic Maserati 'Birdcage', up to the integral, new type of body construction, called body frame integral (BFI). This matter is discussed by Deb, [29], making the distinction of the spaceframe architecture and the unibody (*i.e.,* unitized or integral body, or monocoque).

Quoting Deb, [29], *'….. A spaceframe design consists of a three-dimensional grid of components (predominantly extrusions and castings) with welded joints and is an inherently rigid*

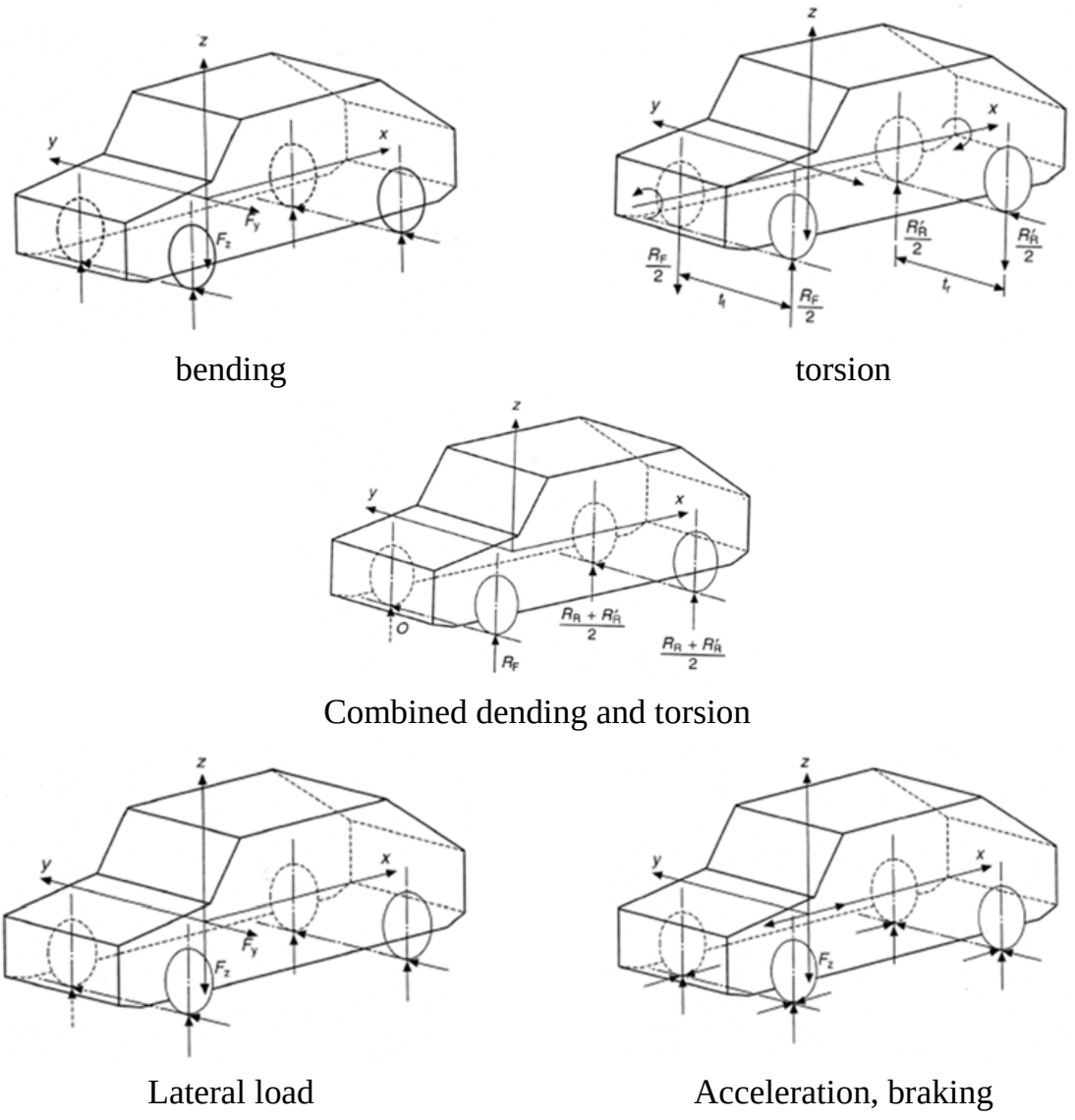

Figure 2.3: Load cases for the global structure, [11].

construction when compared with a unibody design in which thin sheet metal parts formed by stamping are joined along flanges with spot welds located at regular intervals. A spaceframe design does not have discrete spot welds (which are a source of discontinuity between mating parts) and the joints are structurally robust, contributing to the stiffness of the frame. However, the attachment of body panels to the frame requires extra effort and free-form styling can be difficult to achieve. Large volume production tends to be cheaper and efficient for unibody vehicles while spaceframe-based body-in-white (BIW) may be more suitable for low to medium volume production, with less initial investment on tooling as compared to stamping of a large number of body panels…..'. Cars as the Audi A8 or the Lotus Elise have space frames.

This matter of architecture and terminology is further clarified by Mallick, [20], in the following quotation:

'…..The structure of most passenger vehicles has changed from the body-on-frame (BOF) construction to body-in-white (BIW) or unibody construction since the 1970s. The BIW construction

is not only lighter in weight, but also provides higher stiffness per unit weight than the BOF construction. In the BOF construction, two front-to-back longitudinal frame members connected along their lengths by several cross members provide the required stiffness for the vehicle and serve as the principal load carrying members. The body is built separately and then attached to the frame. The BIW construction consists of an integrated box structure, several skin panels (such as roof, quarter panels and floor pan) and bulkheads (such as floor cross members, roof rails, A-pillars and B-pillars), all of which contribute, to a greater or lesser extent, to the stiffness of the vehicle.…..'.

The term monocoque is frequently used to distinguish the early vehicle structures, with separate chassis supporting the bodywork, from the subsequent, and current, unibody constructions - also named unitary construction, unit body, unibody, or Body Frame Integral construction. However, strictly speaking monocoque is a structure that supports loading through its skin, and although this is partially true in unibody construction, this also relies upon structural sections, bulkheads and tubes to provide most of the strength of the vehicle.

2.1.3 The CCB

As mentioned before, *e.g.*, Brown, [10], the CCB is usually supported between the front body hinge pillars – FBHPs in USA terminology, known as 'lower A pillars' in Europe. The CCB supports the steering column, and may support the brake pedal pivots and clutch pedal pivots further to the instrument panel. The primary structural performance criteria for the steering column assembly are usually:

1. Meet a minimum natural frequency target to assure vibration isolation from road and engine idle excitation.

2. Accommodate occupant safety and vehicle crashworthiness objectives.

This thesis is a contribution to a project, QREN 'CCB360', where a company – SODECIA – seeks design innovation for the next generation of cross car beams.

Ardayfio, [32], characterizes innovation in the process of product creation as, (quoting): *'….The critical characteristic of design innovation lies in the features of the new design. A process of design innovation produces characteristics that are novel from several aspects, including component features, functionality and ease of operation, and manufacturing processes associated with the new design.….'.* In the case of the mentioned project, the intention is to improve weight and reduce cost, whithout compromising durability, crashworthiness and satisfying all the relevant requirements. An example of a possible path leading to innovation is found in the recombination of processes and materials, as exemplified by Ardayfio, [32], who mentions the possibility of combining injection molded plastics with a steel structure, leading to an hybrid construction with improved performance in buckling, as found in cross car beams, front ends, etc.. The same reference also argues that hybrid steel/polyamide structures should not pose recycling problems, since they can be shredded using conventional means, separated into steel and polymer using magnetic means, and recycled.

Manufacturing considerations should be made concurrently with the design of the product. Design for manufacturing – but also design for recycling, dismantling etc. – must be performed in an integrated way such that costs and product development time are both reduced. Frise, [33], discusses the problem of the product realization process, namely as concerns the integration of the design and manufacturing processes. At the OEM level, the design decisions must be communicated through the supply chain and production system quickly while still maintaining strict confidentiality of the new vehicle's design features. This implies that companies - such as SODECIA - must be agile and use foresight in planning their design and manufacturing processes. The car industry uses most of the industrial technological materials, as steel, Aluminum alloys, Magnesium alloys, plastics (thermoplastic and thermoset), composites, and processes – machining, casting, injection, moulding, stamping, welding further to a variety of other structural connection processes as riveting, clinching, bonding, etc..

Technologies are constantly evolving, and novel technologies emerge every once in a while. Among these, hydroforming may be of special interest for cross car beams, [33]. Known materials, but in unusual form – *e.g.*, aluminum foams – may be of interest in some applications, where energy absorption may be of interest, [34], combined with a great notch insensivity, [35].

Structural optimization is discussed by Lorenzo, [36], who notes that (quoting verbatim): *'….The drive for lower weight instrument panels (IP) can be addressed with different design approaches. The first and more traditional approach is to substitute existing substrate materials with materials having a higher stiffness-to-density ratio. The second approach looks at the subsystem level where weight reduction is achieved through part integration. The third and most radical approach is weight reduction at the system level. Alternatives to instrument panels that use traditional cross car beam structures will be presented. With these alternatives, hybrid and structural instrument panels can be developed in which weight reduction is achieved by part integration and by allowing plastic materials to fulfill a more significant structural role than in traditional IPs….'.* As an example, this may lead to the consideration of structural IPs, as mentioned in the first lines of this chapter.

Furthermore, Lorenzo, [36], summarizes the challenge posed to CCB and IP suppliers as follows *'…..The instrument panel of the twenty-first century is characterized by functionality, and cost and weight effectiveness. The efficiency and effectiveness required by the market will require the integration of design, materials and processes where:*

- *novel designs drive materials and processing developments;*
- *new material developments drive new designs and processing techniques; and*
- *new processing techniques drive new design, flexibility and materials.*

The integration of design, engineering, materials science, and processing technology is paramount in order to develop a fully optimized IP system that results in a cost and weight effective solution to any given set of engineering requirements…..'.

The desired outcome of the design efforts should be, as concluded by Lorenzo, [36], a balanced structure where no redundant components or materials are used, providing the most

weight and cost effective option to meet the requirements.

2.1.4 Crashworthiness and NVH

The passive safety of vehicles is evaluated through expensive tests described in rules, standards and other guidelines as FMVSS (Federal Motor Vehicle Safety Standards) or NCAP (New Car Assessment Program) in the USA and EuroNCAP in Europe. Literature on crashworthiness includes journals such as the *International Journal for Crashworthiness*, published by Taylor and Francis. Deb, [29], points out that components of vehicle BIWs relevant for crash energy absorption can become either too stiff or exhibit undesirable collapse modes. The deliberate introduction of weaknesses - 'triggers' - in a component at desirable locations may maximize impact energy absorption and lead to improved collapse modes. Crashworthiness is further discussed by Hu, [37], who relates the CCB behavior and leg injuries.

An associated issue, object of numerical modeling, is the vibration behavior, relevant for NVH (Noise, Vibration and Harshness) analyses. The work already performed by a Portuguese company – GESTAMP – is publicly described by Volart, [1] . This work used LS-DYNA software, like the work of Tabacu on crashworthiness, [31], and also Lam, [30], who discuss the consequences of gauge thickness choice.

2.1.5 Recycling

The innovation process in this field is further constrained by compliance with the targets for recycling. 'Design-for-dismantling' is now a relevant issue – together with all the design-for-X already well established, such as design-for-manufacturing, design-for-assembly, design-for-quality, design for maintainability, etc.. The issue of recycling was already mentioned above. As pointed out by Slik, [28], *'….. The European End-of-Life Vehicle (ELV) directive will demand from the automotive industry a quota of 85% reuse and recycling to be met by 2015. This very high reuse and recycling quota for the complete vehicle forces OEMs and the supplier industry to reach a target level for recycling of plastics which is higher than legislation targets set in other sectors….'*.

In the following paragraphs a concise presentation of some aspects of materials relevant for the CCB is presented.

2.2 Concise reference to materials of interest for CCB's

2.2.1 Materials

Weight reduction, and consequent energy economy, lower environmental pollution and sustainability are powerful drivers for innovation in the automobile and all other transportation sectors. In car engineering the traditional material – low carbon steel – has given place to a situation where a variety of metals and non-metals are used. Steel is still the major choice, but the variety of steels now used is huge, as shown by an example of a mass production low cost vehicle in Figure 2.4, [12], where applications for mild steel, bake hardenable steel,

HSLA (high-strength low-alloy steel), dual-phase and multi-phase, and press hardened steel are highlighted.

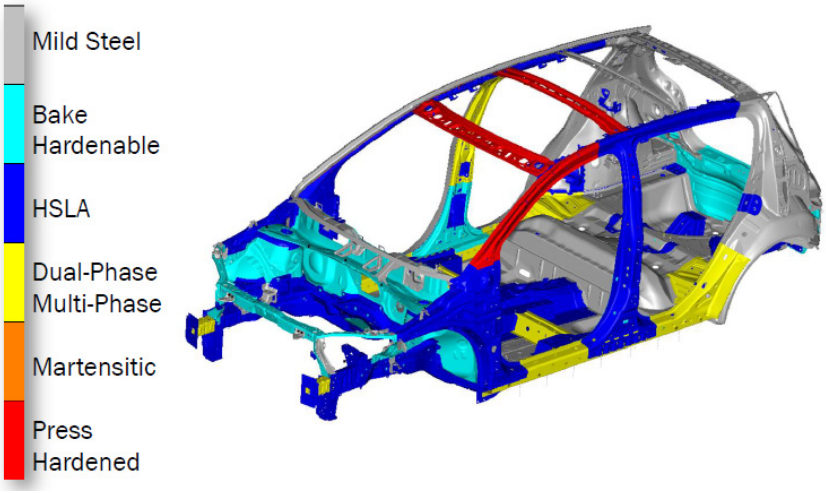

Figure 2.4: Body steel selection for GM Chevrolet Sonic, [12].

Being light materials, Aluminum and Magnesium have always been of interest in automobile engineering, and this trend is reinforced now.

Another focus of interest is the use of a variety of polymer matrix composites. A 1997 reference in *Reinforced Plastics,* [38], stated that high-speed manufacturing techniques for structural composites were not fast enough for large volume production. This drawback may have improved with increasing automation and enhanced production technologies, but certainly still is a problem. Frequently the widespread use of such materials is hindered by the material cost, or by the increased costs of production of parts, and that is the reason why it is usually in the high end of exclusive cars that the use of these non-traditional choices and solutions is first found. The Audi A8 has an all Aluminum bodywork, whereas the Lotus Elise has a fibreglass body shell supported by a chassis composed of Aluminum extrusions; carbon fibre structures are found in the McLaren MP4-12C and other exotic very high speed and very high cost niche vehicles. Reductions in materials costs and easier, faster and less costly processing technologies will certainly lead to the more widespread use of these light alloys and composites in more common vehicles.

The following Table 2.1, [20], highlights a few relevant properties of selected materials.

The use of Al extrusions has an economical aspect that is worth mentioning: extrusion dies are far less expensive than stamping dies or casting moulds, [20]. Table 2.1 who also points out that properties as well as costs of chopped fiber FRPs vary significantly depending on volume percentage and distribution of the glass fibers and the FRP manufacturing process, with flat sheet molding compound (SMC) sheet competing directly with Al alloy sheet, pultruded FRPs with Al alloy extrusions, and shapes produced from bulk molding compound (BMC) competing with aluminum alloy castings.

A comparison can be made between Al Alloys and chopped fiber FRPs, (SMC), in a matrix – Table 2.2 - where the performance of each type of material in several important criteria is

Table 2.1: Material property comparisons, [20].

material	density ρ (g/cm^3)	tensile modulus E (GPa)	yield strength (MPa)	tensile strength (MPa)
DQ low carbon steel	7.87	207	186	317
TRIP 450/800 steel	7.87	207	400	700
5182 H24 Al alloy	2.7	70	235	310
6111-T62 Al alloy	2.7	70	320	360
AZ91 Magnesium	1.8	45	160	240
High strength CFRE unidirectional	1.55	138	-	1550
GFRE unidirectional	1.85	39	-	965
SMC R50	1.87	16	-	164

ranked poorer, indifferent, better or not applicable (-, ~ ,+,×).

Table 2.2: Comparative properties of Al alloys and SMC composites, [20].

	Al	FRP
density	-/~	+/~
strength	-/~	+/~
strength / weight ratio	~	~
E	+	-
ductility	+	-
formability	+	×
machinability	+	-
weldability	+	×
joining	+	-
combustible	+	-
recyclablility	+	-

A critical aspect of engineering with multimaterial solutions is the design of structural connections. A major source of information about adhesive bonding is given in the 'Handbook of Adhesion Technology' by Silva, [39], whereas structural connections among metallic parts are dealt with for example in Moreira, [40].

Using composites connected with metallic parts in hybrid structural systems is currently being developed in aeronautics, automotive, railway, and civil engineering applications. A hybrid structure has potential advantages over a single material product when cost, maintenance, weight and structural performance are considered simultaneously. The connection

metal composite is a source of difficulties; some of these are discussed in an extensive review provided in 'Composite joints and connections: principles, modelling and testing' , [41].

2.2.2 Steels

Figure 2.4, above, already suggested the diversity of options for steel open to present day automobile designers. It is interesting to record some comparisons of basic data for different steels, as in Table 2.3.

Table 2.3: Comparison of basic data for several steels (DP – dual phase; HSLA - precipitation hardened HSLA high-strength low-alloy steels), [21].

grade	yield strength (MPa)	tensile strength (MPa)	total elongation %	yield/tensile strength ratio
DP600	340	590	21	0.58
DP1000	550	980	8	0.56
340 HSLA	340	410	22	0.83
550 HSLA	550	610	18	0.9

This table suggests the advantage of dual phase steels in crashworthiness considerations, given the high energy absorption capability of structural components manufactured with this material. Other type of steel of interest is the martensitic steel, with a matrix rich in martensite, and usually displaying high tensile strength of the order of 900 MPa or even up to 1400 MPa. According to Horvath, [21], (quoting) *'... martensitic steels are very useful in automotive applications for door beams, bumpers, very lightweight and high strength lower side members (rocker panels), and cross car bars and beams that are designed to prevent intrusion into the passenger compartment....'*.

2.2.3 Aluminium

From Sauer, [42], *'.....Aluminum extruded profiles are particularly suited in special cases for the manufacture of safety components for the automobile because the cross-sectional shape can be exactly matched to the loading. They also offer favorable mechanical properties and density and the low E modulus as well. A typical example is the side door beam that can fulfill its role in a very functional way. ....'*.

In Ford's Partnership for a New Generation of Vehicles (PNGV) programme – P2000 car - it was found that Ford achieved substantial weight savings by making most of the P2000's body from aluminium which is less costly than using carbon fibre composites.

A major driver in favor of Aluminum usage is however found in the increasing attention to recyclability, given its excellent performance in that respect.

2.2.4 Magnesium

Magnesium is the lightest structural metal (see Table 2.1 above), with a density of the order of a fourth of the density of steel, and presents tensile strength of the order found in Al alloys. The literature on Magnesium usage in automotive engineering is huge. Luo, [43], for example, remarks that while magnesium components may be heavier than those made with polymer composites, they are stiffer due to their higher elastic modulus.

According to Beals, [44], automotive applications for magnesium include cross car beams, seat frames, steering column brackets, vehicle front end structures, door closures, engine cradles, and power train components, in the form of die castings providing lower weight at costs that are competitive. China is the production leader for magnesium and fabricates more than fifty types of magnesium alloy components including transmission cases, cylinder heads and steering wheel armatures, [44].

A drawback of magnesium alloys is their problematic corrosion behavior. Corrosion behaviour of magnesium may be a problem; however this is less important in interior applications such as IP and CCB. Luo, [43], discusses material choices for the IP as follows (quoting): '*. . . . . The first magnesium IP beam was die cast by GM in 1961 with a mass saving of 4 kg over the same part cast in zinc. The design and die casting of magnesium IP beams have advanced dramatically in the last decade. For example, current IPs normally have a thickness of 2–2.5 mm (compared with 4–5 mm for the earlier IP beam application) with more part consolidation and mass savings. However, the use of cast magnesium IP beams has recently been facing strong competition. IP beams made of aluminium extrusions are used by Mercedes in Europe. IP designs using bent steel tubes (with or without hydroforming) are slightly heavier than magnesium die casting, but significantly less expensive. To maintain and grow its use in IP production, magnesium design and thin-wall casting technology must continue to improve, further reducing weight and cost. Tubular designs using magnesium extrusions and sheet components should also be explored. . . .*'.

As far as crash behavior is concerned, Luo, [43], mentions that the performance of magnesium may be poorer than steel or aluminum, in that although energy absorption is adequate, failure of magnesium tubes may be by sharding or fracture, whereas in aluminum or steel it is likely to be by progressive folding.

Friedrich, [13], gives an extensive discussion of automotive uses of magnesium, and includes Figure 2.5 showing the CCB of a FIAT Marea, and Figure 2.6 showing the dash board panel carrier of a Mini (a BMW product).

Byrne, [45], mentions the applications of Magnesium in CCBs in the form of die casting and remarks its good machinability.

According to Friedrich, [13], the advantages of the use of magnesium in CCBs include:

- reduction in part count;
- improvement of body stiffness and crash behavior (although this seems to contradict the caution stated by Luo, [43], mentioned above);
- increasing vertical steering column frequency (relevant for NVH considerations);

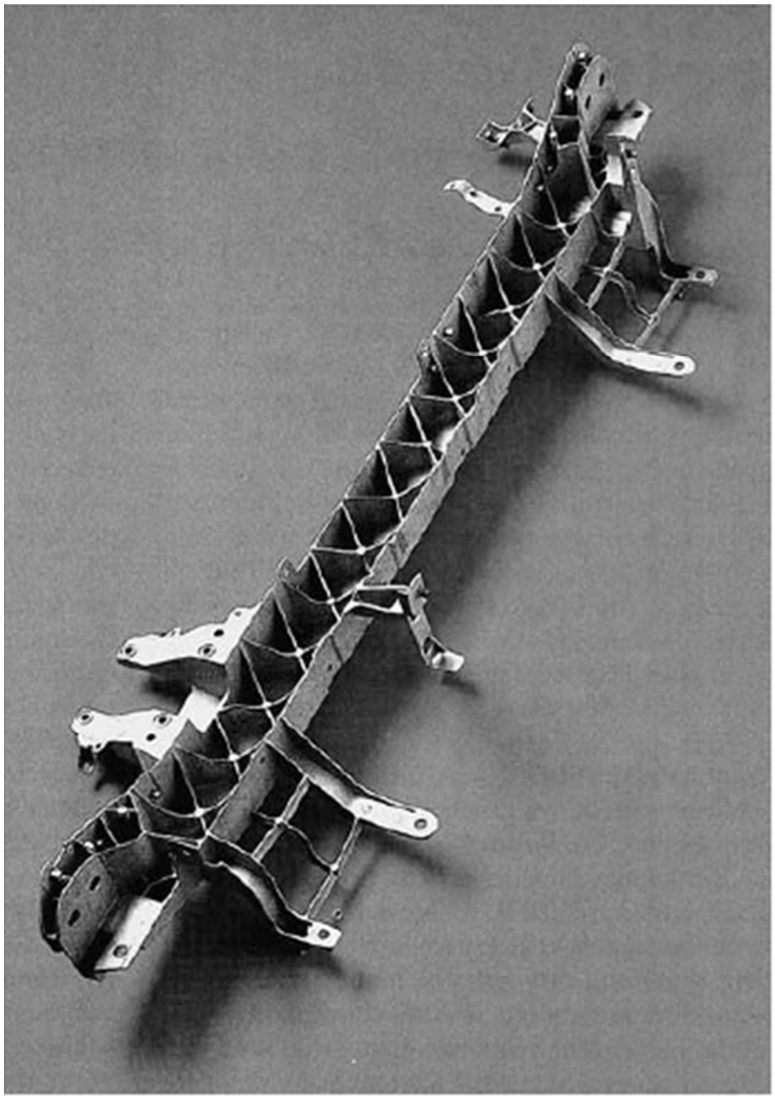

Figure 2.5: Cross car beam of a FIAT Marea, [13].

- a 40% reduction in weight when compared with steel;
- possible cost advantage.

More interesting are the comments made by Friedrich, [13], concerning design/manufacturing issues: the design freeze in a vehicle development phase is not possible until a very advanced stage; and the production of a complex die as requires for such a part is a lengthy process, that must however adapt to the OEM vehicle development timings; this imposes upon a CCB supplier a critical reduction in development and testing time, a key feature in magnesium applications.

Xu, [46], notes that the crashworthiness of magnesium extrusions, taking into account yield strength, ductility, and density, compares favorably to automotive Al alloys and high-strength steels. Applications of magnesium extrusions in cross car beams were however not identified in this literature review.

A SAE paper, [14], discusses the unique design concept for a Ford GT instrument panel

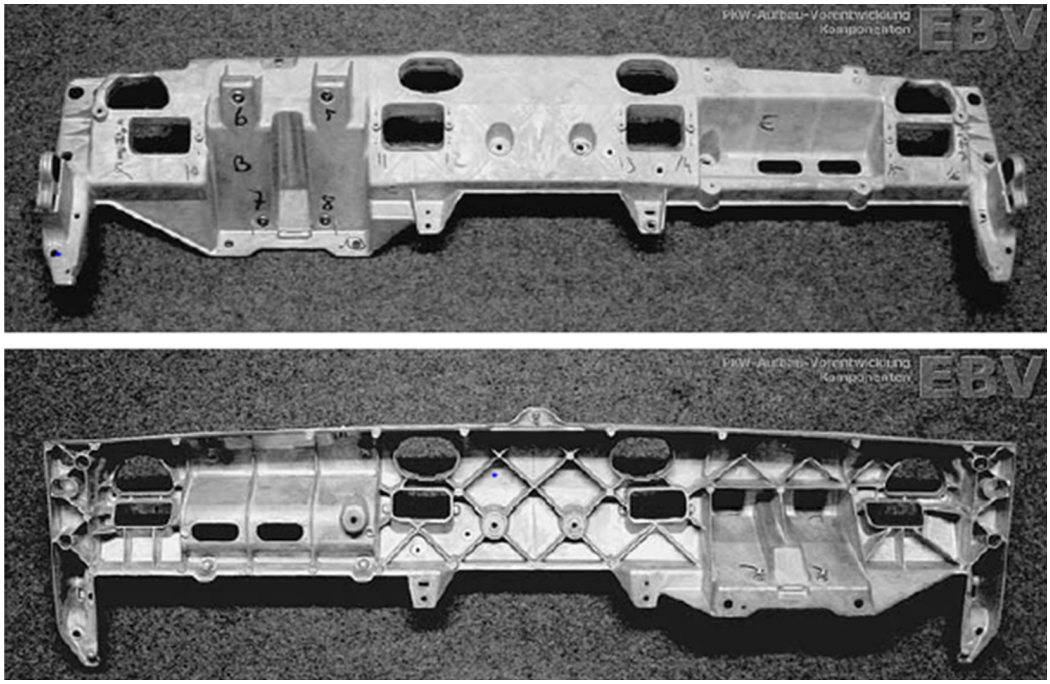

Figure 2.6: Dash board panel carrier of a Mini (a BMW product), [13].

comprised of a structural magnesium cross-car beam and other components, *i.e.*, radio box and console top, which is believed to be the industry's first structural IP from vehicle crash load and path perspectives, Figure 2.7.

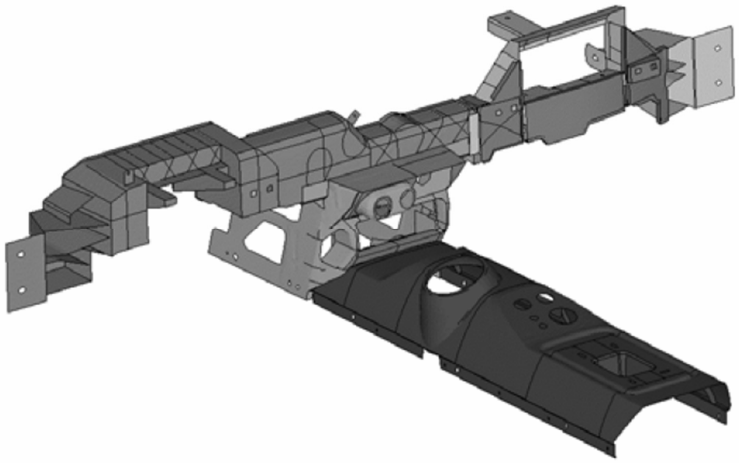

Figure 2.7: Design of the magnesium IP cross car beam and console top, [14].

2.2.5 Metallic Foams

Whereas polymeric foams have been in use for long time, metallic foams are now emerging as possible choices for designers. Baumeister, [34], lists the following properties of metallic foams, interesting for transport applications:

- nearly closed porosity,

- low specific weight,
- high energy absorption capacity during plastic deformation,
- high specific stiffness,
- reduced thermal and electrical conductivity ,
- good mechanical and acoustic damping,
- not inflammable,
- recyclable,
- good machinability.

Energy absorption may be designed by the selection of adequate foam characteristics, namely matrix material, cellular geometry and relative density. Foams are not used on their own, but integrated in the body structure in suitable locations.

Mccullough, [35], presents data on the behavior of Al foams, and one of the conclusions presented concerns the fatigue behavior for a panel with a central hole, where the foam was found to be notch insensitive from the fatigue viewpoint.

2.2.6 Plastics

SMC composites are extensively used in surface critical components like hoods, deck lids and spoilers to semi-structural parts such as cross-car beams and radiator supports, competing with steel. However, Steenkamer, [47], mentions that General Motors decided to replace SMC with steel on their minivans. He further remarks the application of liquid molding processes such as resin transfer molding and structural reaction injection molding (SRIM) in certain niche programs like the Aston Martin DB7, the Chevrolet Corvette, the Dodge Viper, and the Lotus Esprit and Elan S2.

Mann, [48], remarks that legislation and regulations have an impact upon the use of plastics in cars, as related to hydrocarbon evaporation and recyclability for example. Most plastic car parts are produced by injection moulding. Compression moulding is used for SMC (sheet moulding compounds) panels.

The Nov. 2000 issue of *Reinforced Plastics*, [49], gives an interesting comment on choice of material and technology for radiator support assembly and CCB. Both components illustrate SMC's capability for parts consolidation. However, whereas the former leads to a low cost product, the latter remains a premium niche component. Some reasons behind this outcome can be explained from the total system perspective. Quoting this reference, *'...Because of their use on light truck platforms, cross car beams consume significant amounts of SMC. The level of functional integration is as large as in the case of the radiator support but the end result is very different. The added complexity pushes the boundaries of SMC flow and mouldability. To make matters worse, attempts have been made to use very low density SMC, resulting in even*

more moulding difficulties. In the end, low cost has not been achieved, making both OEMs and moulders unhappy.…'.

The subject of CCBs is again taken by the *Reinforced Plastics* journal (Sept.-Oct. 2011), [50], noting that Ashland Performance Materials 'Aropol' PET-based resins are applicable for structural, non Class A SMC components – such as reinforced panels, cross car beams and grille opening retainers – that require high mechanical and impact properties and fast cure.

Stewart, 2003, mentions a Bayer Automotive Plastics hybrid plastic metal technology of interest for instrument panels, CCBs and steering column supports. The *Reinforced Plastics* journal (Jan. 1997), [38], mentions an Alpha/Owens Corning structural SMC resin that can be thickened without sacrificing mechanical strength and heat resistance is suitable for use in applications including radiator supports, fuel tank heat shields, and cross car beams.

2.2.7 Composites

Fiber reinforcements are used to increase the modulus of polymers, as in glass-fiber reinforced polymer (GFRP) and advanced carbon fiber reinforced polymers (CFRP). Polymeric composites are divided in two groups, [43]:

- Structural composites (structural-GFRP and structural-CFRP) in which glass or carbon fibers are uniaxially orientated to provide unidirectional strength/ stiffness for structural applications.
- Exterior composites (exterior-GFRP and exterior-CFRP) in which glass or carbon fibers are appropriately aligned to provide 'quasi-isotropic' strength/ stiffness in planar directions but not in the thickness direction, for exterior panel applications.

Luo, [43], mentions the important problem of creep associated with polymeric materials.

Thermoplastics are discussed in Mallick, [20], remarking firstly their recyclability.

Maruthayppan, [51], studied several structural components, including a CCB, and conclude that *'a thermoplastic composite system can be expected to absorb more energy in critical areas, compared to a conventional steel cross-car beam system. Further study for additional crash information should be performed, as well as comparative analysis with injection- molded structure's'.*

Thermosets are discussed in Mallick, [20], noting their inability for reuse or recycling.

A SRIM (structural reaction injection moulding) composite CCB is discussed by Kendall, [52]. That paper concludes that functional advantages offered by the composite component over the traditional steel component include 50% weight savings, improved NVH performance, part count reduction and ease in vehicle assembly. The major disadvantage of the composite component was increased manufacturing cost, particularly the variable cost, when compared with the steel component.

2.3 Brief reference to some of the relevant technologies

2.3.1 Hydroforming

Hartl, [15], discusses hydroforming in the context of automotive engineering, and remarks that it provides advantages regarding the manufacturing of complex shaped lightweight components. The Figure 2.8 illustrates schematically the process.

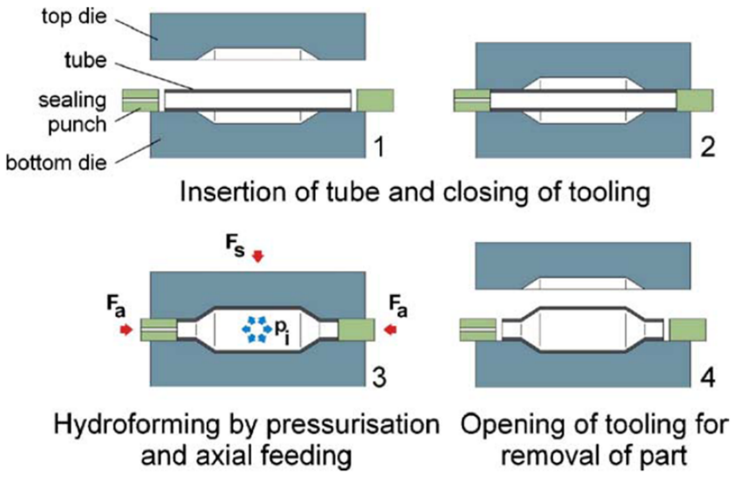

Figure 2.8: The hydroforming principle, [15].

An interesting application for design and for crashworthiness is the easy production of bellows, discussed by Kocanda, [53]. Although most hydroforming applications concern closed sections, sheet hydrofoming processes are available, *e.g.* Parsa, [54].

2.3.2 Welding

A general review of the state of the art for some welding technologies is provided in Moreira 2012, [40]. A presentation by a manufacturer of welding equipment (TRUMPF), by Hravilla, [55], contains reference to the fabrication of CCBs. Figure 2.9 is taken from that source.

Laser welding is an interesting option. According to the *Laser Technik Journal* (LTJ) (January 2013, No.1, p.4), the Dutch company AWL built for Kirchhoff Automotive a production line comprising two laser welding machines that will guarantee a production of 220000 cross car beams per year. According to this source, the use of laser welding for CCBs was for long time common in the USA, but not so in Europe. Process stability is claimed as a plus of this choice of welding technology.

2.4 Industrial engineering aspects and LCA

2.4.1 Inspection

Inspection technologies for the mass fabrication of CCBs are discussed in Killing 2009, [16], and in Sun 2012, [56]. Technologies of AVI (automated visual inspection) were used

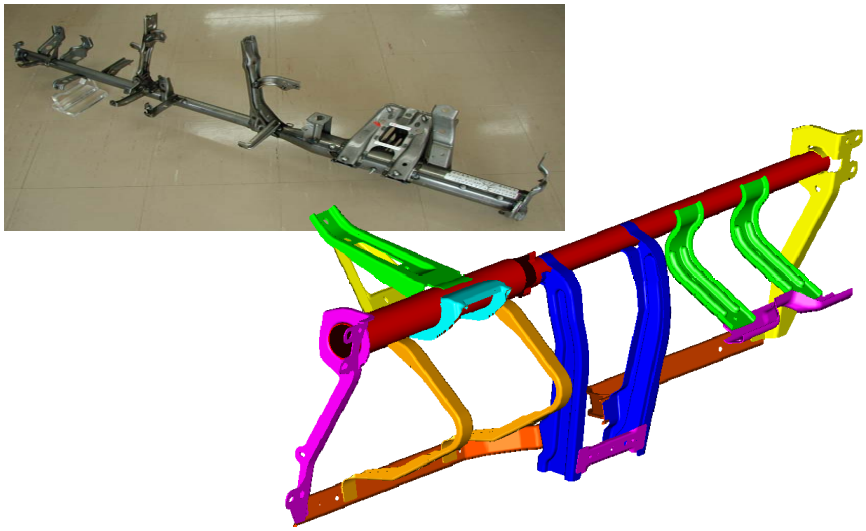

Figure 2.9: Instrument panel carrier for automotive dashboards; source Havrilla, 2010.

successfully.

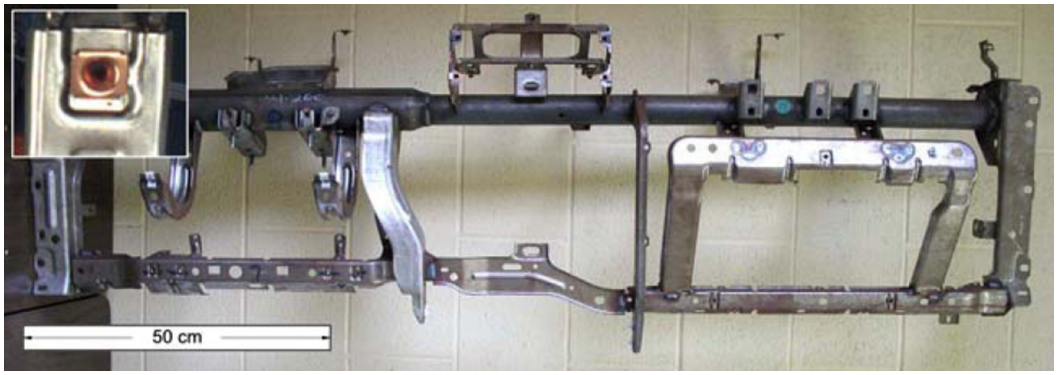

Figure 2.10: Stamped steel CCB; the zoom shows a close up of one of 46 clips, [16].

Killing, [16], discusses inspection of a stamped steel beam that acts as the mounting frame for the dashboard. The system has been tested using images generated by a commercial machine vision system installed on an assembly line for the production of automotive CCBs, Figure 2.10. This particular CCB has a length of 170 cm and 46 metal clips must be inserted to provide threaded fastening points that allow the dashboard to be attached to the beam. At the final inspection station, the beams are checked to ensure that all clips are present and correctly inserted.

2.4.2 LCA – recycling

Life cycle and recycling of lightweight vehicles are discussed by Das, [57]. An interesting analysis of LCA for IPs is presented by Tharumarajah, [58], concluding that the comparison of environmental performance reveals that magnesium IPs performed the worst. Most of its emissions come from magnesium sourced from China and from the use of SF6 cover gas

in melt protection. In the initial paragraphs of the present literature review it was already mentioned that according to Slik, [28], the removal and dismantling of an IP could not be done in a cost efficient way. That was due to the lack of a design for dismantling and recycling strategy, as well as low level of polymer revenue compared with competitive price of virgin polymer.

Keoleian, [9], uses the IP as a case study to investigate the influence of environmental, cost, and performance requirements on the design and management of automotive components, presenting a lifecycle analysis to characterize the major environmental impacts associated with a generic IP. A life-cycle cost analysis is also conducted to understand the market forces.

2.4.3 Supply chain management

Doran, [59], notes that in recent years car manufacturers have been moving from the procurement of discrete parts to the procurement of modular systems. The impact of the use of modular systems in the supply chain management was studied by these authors using as a case study cockpit modules for a French car manufacturer. Modular assembly and development is of interest to complex products under constantly varying consumer demands. Modularity offers increased flexibility, increased speed to market, and reduced cost, through the generation of new products combining and recombining components.

Globalization is driven by the emergence of the BRICs, in particular China, as players in the industrial manufacturing scene. In an article on globalization recently published, the production of cross car beams in China is mentioned in rather interesting terms. Quoting verbatim form Herrigle, [60]:

'……..Rather than designing a wholly new machine or component for the Chinese market, many firms redesign existing offerings to make them more affordable and appropriate for Chinese needs….'. This is the case of a German automobile supplying internal frames (front ends, engine cradles, cross car beams) in China: *'…..Even when the firm wins a bid on a global component that will be built into the same automobile model in Europe, North America, and China, materials, component designs, and manufacturing procedures still differ in each market. In China, the company does not use the same quality steel or the same sophisticated welding processes that it uses to construct the customer's front ends in Europe. The China product is manufactured in a comparatively primitive fashion and is less complex, less durable, and incapable of the same level of performance as its European counterpart…..'*.

It remains to be seen if the quoted remarks will still be true in the future.

Theoretical focus: related literature

During a car crash incident, Figure 3.1, the vehicle body experiences high impact loads which produce localized plastic hinges and buckling which can ultimately lead to large deformations and rotations with contact and stacking among the various components. After stresses exceed the yield strength of the material or its critical buckling load, localized structural deformations occur during a few shockwave transits in the structure followed by inertial effects and a transient response. Car crashes are dynamic events that persist for a short duration of 100 to 200 ms, [61].

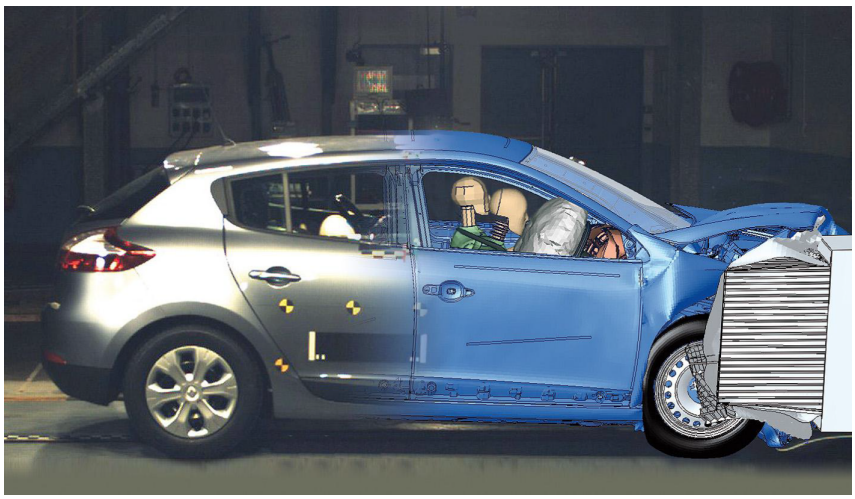

Figure 3.1: Renault Megane crash simulation. [17]

3.1 Crash analysis

Structural response is time-dependent if the loading is time-dependent. However, if the loading is cyclic and frequency is less than 1/4 of the structure first natural frequency, we are facing a quasi-static problem. If loading is of higher frequency or is applied suddenly, dynamic analysis is required, [62].

Dynamic analysis uses the same stiffness matrix as stactic analysis, but also requires mass and damping matrices. For a given magnitude of loading, dynamic response may be greater or less than static response. It will be much greater if loading is cyclic with frequency close to the natural frequency of the structure, [62].

If loading excites only a few of the lowest frequencies and response must be calculated over a time span equal to several multiples of the longest period of vibration, as is the case for earthquake loading, either the mode superposition method or an implicit method of direct integration may be appropriate, [62].

In crash analysis, structures experience extremely high forces in a short period of time: an impact. Here we seek a transient response called response history. Solution requires that differential equations of motion be integrated in time. During the impact, the loading excites many frequencies and response must be calculated for no more than a few multiples of the longest period. In this type of cases explicit direct integration may be appropriate, [62].

3.1.1 Dynamic equations

General Equation

The governing equation for structural dynamics, derived below, provides general expressions for structural mass and damping. Equation of motion is derived by requiring that work done by externally applied loads be equal to the sum of work absorbed by dissipative and inertial forces for any virtual displacement. For a single element of volume V and surface area S, this work balance becomes, [62],

$$\begin{aligned} &\int \{\delta \mathbf{u}\}^T \{\mathbf{F}\}\, dV + \int \{\delta \mathbf{u}\}^T \{\mathbf{\Phi}\}\, dS + \textstyle\sum_{i=1}^{n} \{\delta \mathbf{u}\}_i^T \{\mathbf{p}\}_i = \\ &= \int \left(\{\delta \mathbf{u}\}^T \rho \{\ddot{\mathbf{u}}\} + \{\delta \mathbf{u}\}^T c \{\dot{\mathbf{u}}\} + \{\delta \boldsymbol{\varepsilon}\}^T \{\boldsymbol{\sigma}\} \right) dV \end{aligned} \tag{3.1}$$

where,

- $\{\mathbf{F}\}$- body forces;
- $\{\mathbf{\Phi}\}$- surface tractions;
- $\{\mathbf{p}\}_i$ and $\{\delta \mathbf{u}\}_i$- prescribed concentrated loads at nodes and their corresponding virtual displacements;
- $\{\delta \mathbf{u}\}$and $\{\delta \boldsymbol{\varepsilon}\}$-virtual displacements and their corresponding strains.

FE discretization provides, [62],

$$\{\mathbf{u}\} = [\mathbf{N}]\{\mathbf{d}\}; \qquad \{\dot{\mathbf{u}}\} = [\mathbf{N}]\left\{\dot{\mathbf{d}}\right\}; \qquad \{\ddot{\mathbf{u}}\} = [\mathbf{N}]\left\{\ddot{\mathbf{d}}\right\}; \quad \{\boldsymbol{\varepsilon}\} = [\mathbf{B}]\{\mathbf{d}\}; \tag{3.2}$$

where,

- $[\mathbf{N}]$- shape functions (functions of space);
- $\{\mathbf{d}\}$- nodal degrees of freedom (functions of time).

Thus eqs. 3.2 represent a local separation of variables. Combining eqs. 3.1 and 3.2, [62],

$$\begin{aligned} \{\delta \mathbf{d}\}^T \Big[&\int \rho [\mathbf{N}][\mathbf{N}]\, dV \left\{\ddot{\mathbf{d}}\right\} + \int c [\mathbf{N}]^T [\mathbf{N}]\, dV \left\{\dot{\mathbf{d}}\right\} + \int [\mathbf{B}]^T \{\boldsymbol{\sigma}\}\, dV \\ &- \int [\mathbf{N}]^T \{\mathbf{F}\}\, dV - \int [\mathbf{N}]^T \{\mathbf{\Phi}\}\, dS - \textstyle\sum_{i=1}^{n} \{\mathbf{p}\}_i \Big] = 0 \end{aligned} \tag{3.3}$$

The first two integrals in eq. 3.3 are identified as "consistent" element mass and damping matrices, [62]:

$$[\mathbf{m}] = \int \rho \, [\mathbf{N}]^T \, [\mathbf{N}] \, dV \qquad [\mathbf{c}] = \int c \, [\mathbf{N}]^T \, [\boldsymbol{N}] \, dV \tag{3.4}$$

The word "consistent" emphasizes that these forms follow directly from FE discretization, and use the same shape functions as the element stiffness matrix. We define the element internal force vector $\left\{\mathbf{r}^{int}\right\}$ as forces and moments applied to 6 d.o.f. elements by nodes to resist stresses within the element, [62].

$$\left\{\mathbf{r}^{int}\right\} = \int [\mathbf{B}]^T \, \{\boldsymbol{\sigma}\} \, dV \tag{3.5}$$

Similar notation is used to identify forces and moments applied to nodes as a result of externally applied loads on the element, [62].

$$\left\{\mathbf{r}^{ext}\right\} \int [\mathbf{N}]^T \, \{\mathbf{F}\} \, dV + \int [\mathbf{N}]^T \, \{\boldsymbol{\Phi}\} \, dS + \sum_{i=1}^{n} \{\mathbf{p}\}_i \tag{3.6}$$

The bracketed expression in eq. 3.3 must vanish if the equation is to be true for arbitrary $\{\delta\mathbf{d}\}$. Thus, in the notation of eqs. 3.4 to 3.6, eq. 3.3 yields , [62]

$$[\mathbf{m}] \left\{\ddot{\mathbf{d}}\right\} + [\mathbf{c}] \left\{\dot{\mathbf{d}}\right\} + \left\{\mathbf{r}^{int}\right\} = \left\{\mathbf{r}^{ext}\right\} \tag{3.7}$$

Equations 3.5 and 3.7 are valid for both linear and nonlinear material properties. If the material is linear elastic, then loads associated with the element stresses are $\left\{\mathbf{r}^{int}\right\} = [\mathbf{k}] \, \{\mathbf{d}\}$, where $[\mathbf{k}]$ is the conventional element stiffness matrix. Global forms for a multi-element structure are, [62]

$$[\mathbf{M}] \left\{\ddot{\mathbf{D}}\right\} + [\mathbf{C}] \left\{\dot{\mathbf{D}}\right\} + \left\{\mathbf{R}^{int}\right\} = \left\{\mathbf{R}^{ext}\right\} \tag{3.8}$$

$$[\mathbf{M}] \left\{\ddot{\mathbf{D}}\right\} + [\mathbf{C}] \left\{\dot{\mathbf{D}}\right\} + [\mathbf{K}] \, \{\mathbf{D}\} = \left\{\mathbf{R}^{ext}\right\} \tag{3.9}$$

3.1.2 Response history: direct integration methods

Response history determination using step-by-step time integration of the dynamic equations is called *direct integration.* Response is evaluated at instants separated by time increments Δt, so we compute structure displacements at times Δt, 2 Δt, 3 Δt, ..., $n\Delta t$, and so on. At the *n* th time step, the equation of motion, Eq. 3.7 or Eq. 3.9, is, [62]

$$\begin{aligned} &[\mathbf{M}] \left\{\ddot{\mathbf{D}}\right\}_n + [\mathbf{C}] \left\{\dot{\mathbf{D}}\right\}_n + \left\{\mathbf{R}^{int}\right\}_n = \left\{\mathbf{R}^{ext}\right\}_n \\ \textit{or} \qquad &[\mathbf{M}] \left\{\ddot{\mathbf{D}}\right\}_n + [\mathbf{C}] \left\{\dot{\mathbf{D}}\right\}_n + [\mathbf{K}] \, \{\mathbf{D}\}_n = \left\{\mathbf{R}^{ext}\right\}_n \end{aligned} \tag{3.10}$$

Discretization in time is acomplished by using finite difference approximations of time derivatives, [62].

Methods of direct integration calculate conditions at time step *n+1* from the equation of motion, a difference expression, and known conditions at one or more preceding time steps. Algorithms can be classified as explicit or implicit. An explicit algorithm uses a difference expression of the general form, [62]

$$\{\mathbf{D}\}_{n+1} = f\left(\{\mathbf{D}\}_n, \left\{\dot{\mathbf{D}}\right\}_n, \left\{\ddot{\mathbf{D}}\right\}_n, \{\mathbf{D}\}_{n-1}, ...\right) \tag{3.11}$$

which contains only historical information on its right-hand side. The difference expression is combined with the equation of motion, Eq. 3.10, at time step *n*. An implicit algorithm uses a difference expression of the general form, [62]

$$\{\mathbf{D}\}_{n+1} = f\left(\left\{\dot{\mathbf{D}}\right\}_{n+1}, \left\{\ddot{\mathbf{D}}\right\}_{n+1}, \{\mathbf{D}\}_n, \left\{\dot{\mathbf{D}}\right\}_n, \left\{\ddot{\mathbf{D}}\right\}_n, ...\right) \tag{3.12}$$

which is combined with equation of motion at time step *n+1*.

3.1.3 Explicit analysis *vs* implicit analysis

In practical application, important differences between explicit and implicit methods are related to stability and economy. Explicit methods are conditionally stable, which means there is a critical time step Δt_{cr} that must not be exceeded if numerical process is not to "blow up" by becoming unstable. Because Δt_{cr} is quite small, many time steps are needed, but each one is executed quickly. Implicit methods are unconditionally stable, which means that calculations remain stable regardless of how large Δt becomes (although accuracy will suffer). In explicit methods, the coefficient matrix of $\{\mathbf{D}\}_{n+1}$ can be made diagonal, so that $\{\mathbf{D}\}_{n+1}$ is cheaply calculated in each time step. In implicit methods, the coefficient matrix of $\{\mathbf{D}\}_{n+1}$ cannot be made diagonal, so that cost per time step is greather, increasingly so as the FE mesh increases in dimensionality. Another consequence of the difference in matrix topology is that an implicit method requires much more computer storage space than an explicit method, [62].

For computers, matrix multiplication is not a difficult task. Matrix inversion is a lot more computationally expensive operation. Implicit code finds a solution by computing the element stiffness matrix and then inverting it to solve for the displacements in the element.

Implicit direct time integration is suited to structural dynamics problems where loads vary slowly, such as loads created by an earthquake. Response is dominated by the lower modes. This method competes with the modal method, and may be cheaper where many modes would be needed in the nodal method and when the analysis need not span great a time, [62].

Implicit methods are used because many problems arising in practice are stiff, for which the use of an explicit method requires impractically small time steps to keep the error in the result bounded (see numerical stability). For such problems, to achieve given accuracy, it takes much less computational time to use an implicit method with larger time steps, [62].

Explicit direct integration is suited to wave propagation problems, *e.g.*, effects created by blast or impact loading, as in vehicle crashworthiness analysis. High-frequency modes must

be represented in analysis. Nonlinearity can be accomodated with relative ease, [62].

In conclusion, an implicit analysis is similar to the explicit analysis with the addition that after each increment, implicit does Newton-Raphson iterations to enforce equilibrium of the internal structure forces with the externally applied loads. One drawback is that during the Newton-Raphson iterations one must update and reconstruct the stiffness matrix for each iteration. This can be computationally costly. The equilibirium is usually enforced to some user specified tolerance.

Number of time steps

Although unconditionally stable, implicit methods typically need many time steps in order to trace the physical phenomena studied, [8].

Explicit analysis typically requires a small time step. This leads to a big number of time steps to compute, which is not a problem because CPU cost per timestep is small. Computer storage requirements are low as well, [8].

Equations to be solved

Implicit analysis requires matrix inversion. The solution of the nonlinear equations require iterative solution strategies, [8].

Explicit analysis requires no iteration and no matrix inversion, [8].

Type of problems

Implicit methods are well suited to solve static problems, [8].

Explicit methods are well suited to solve dynamic problems, [8].

3.1.4 Explicit simulation

Explicit analysis treats the structure as a dynamic problem and solves dynamic equations of motion in the time domain. It is especially efficient to solve crash, impact and similar dynamic problems, particularly if material non-linearity (plasticity,...), large deformations or contact occur. For explicity analysis all nodal and element quantities are given with respect to time, [63].

Explicit analysis is applied in broadband excitations, [62].

Crash simulation in PAM-CRASH is performed with explicit time integration using the half-step central difference scheme, [17].

Explicit direct integration

As illustrated in Figure 3.2, the **half-step central differences** method scheme is, [62]:

1. With Δt, the time step, velocity and acceleration at time step n are approximated by

the central difference equations, [62],

$$\left\{\dot{\mathbf{D}}\right\}_{n-1/2} = \frac{1}{\Delta t}\left(\{\mathbf{D}\}_n - \{\mathbf{D}\}_{n-1}\right)$$
$$and \ \left\{\dot{\mathbf{D}}\right\}_{n+1/2} = \frac{1}{\Delta t}\left(\{\mathbf{D}\}_{n+1} - \{\mathbf{D}\}_n\right) \tag{3.13}$$

$$\left\{\ddot{\mathbf{D}}\right\}_n = \frac{1}{\Delta t}\left(\left\{\dot{\mathbf{D}}\right\}_{n+1/2} - \left\{\dot{\mathbf{D}}\right\}_{n-1/2}\right) =$$
$$= \frac{1}{\Delta t^2}\left(\{\mathbf{D}\}_{n+1} - 2\{\mathbf{D}\}_n + \{\mathbf{D}\}_{n-1}\right) \tag{3.14}$$

2. Equation of motion is rewritten, eq. 3.10, with velocity lagging by half a time step. Thus for the half-step method we use the equations, [62],

$$\{\mathbf{D}\}_{n+1} = \{\mathbf{D}\}_n + \Delta t\left\{\dot{\mathbf{D}}\right\}_{n+1/2} \tag{3.15}$$

$$\left\{\dot{\mathbf{D}}\right\}_{n+1/2} = \left\{\dot{\mathbf{D}}\right\}_{n-1/2} + \Delta t\left\{\ddot{\mathbf{D}}\right\}_n \tag{3.16}$$

$$[\mathbf{M}]\left\{\ddot{\mathbf{D}}\right\}_n + [\mathbf{C}]\left\{\dot{\mathbf{D}}\right\}_{n-1/2} + \left\{\mathbf{R}^{int}\right\}_n = \left\{\mathbf{R}^{ext}\right\}_n \tag{3.17}$$

3. Combining these three equations, [62],

$$\frac{1}{\Delta t^2}[\mathbf{M}][\mathbf{D}]_{n+1} = \left\{\mathbf{R}^{ext}\right\}_n - \left\{\mathbf{R}^{int}\right\}_n +$$
$$+\frac{1}{\Delta t^2}[\mathbf{M}]\left(\{\mathbf{D}\}_n + \Delta t\left\{\dot{\mathbf{D}}\right\}_{n-1/2}\right) - [\mathbf{C}]\left\{\dot{\mathbf{D}}\right\}_{n-1/2} \tag{3.18}$$

where, if linear conditions prevail, $\left\{\mathbf{R}^{int}\right\}_n = [\mathbf{K}][\mathbf{D}]_n$

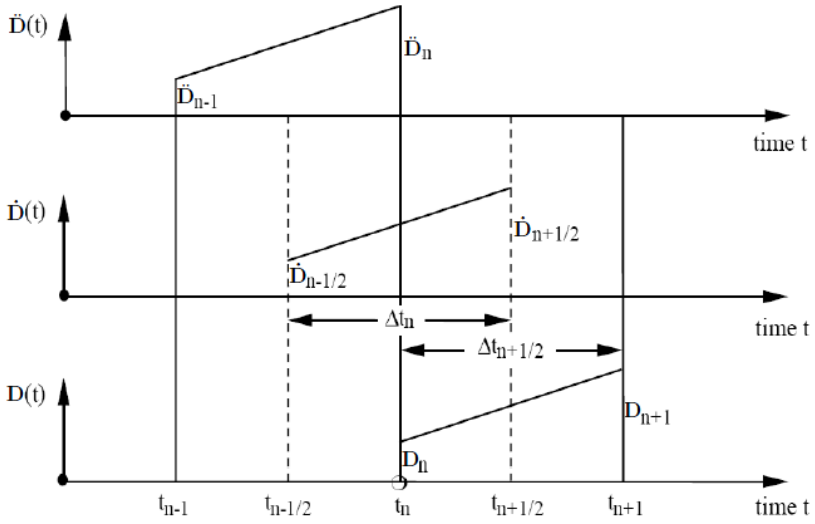

Figure 3.2: Explicit time integration, [8].

Numerical stability

Central difference scheme is conditionally stable so the time step Δt is restricted. The shell time step required for stability is computed by PAM-CRASH as follows, [17]:

- $\Delta t_{shell} = kMIN\left[L/c \min\left(1.0, \frac{L}{\sqrt{3}h}\right)\right]$ for BEND active;
- $\Delta t_{shell} = kMIN\,[L/c]$ for NOBEND active;

where,

- k is the scale factor for the time step;
- MIN is the minimum over all shell elements;
- L is the characteristic length;
- c is the speed of sound,

  $c = \sqrt{E/\rho}$ for NONU active,
  $c = \sqrt{E/\rho(1-\nu^2)}$ for NU active;

- h is the shell thickness;
- ρ is the mass density;
- E is the Youg's modulus.

Remark: If a damping ratio ξ (*KSI*) has been specified in the material properties, Δt_{shell}stable time step is reduced by factor $\left(\sqrt{1+\xi^2} - \xi\right)$, [17].

Time step calculation

Generally the smallest time step of all elements in a model is used for the time-integration. For 2D (shells) and 3D (solids) elements the time step calculation is based on a "characteristic" length. There are two time step criterias available in PAM-CRASH, [17]:

- **Standard time step criteria (*LARGE*)**: the standard time step criteria for quadrilateral, degenerate quadrilateral, triangular and C° triangular shell elements are based on the elastic wave travel time along the characteristic lengths illustrated in Figure 3.3. Use of the standard time step criteria usually results in time steps larger than the ones obtained from the stringent criteria, [17].

- **Stringent time step criteria (*SMALL*)**: the stringent time step criteria for shells are based on the elastic wave travel time along the characteristic lengths illustrated in Figure 3.4, [17].

The stringent time step criteria should assure solution stability in severe cases (very distorted meshes, etc), where the economical standard criteria may become inadequate, [17].

The use of stringent time step criteria may sometimes considerably reduce the solution time step with respect to the solution time step from the standard criteria, [17].

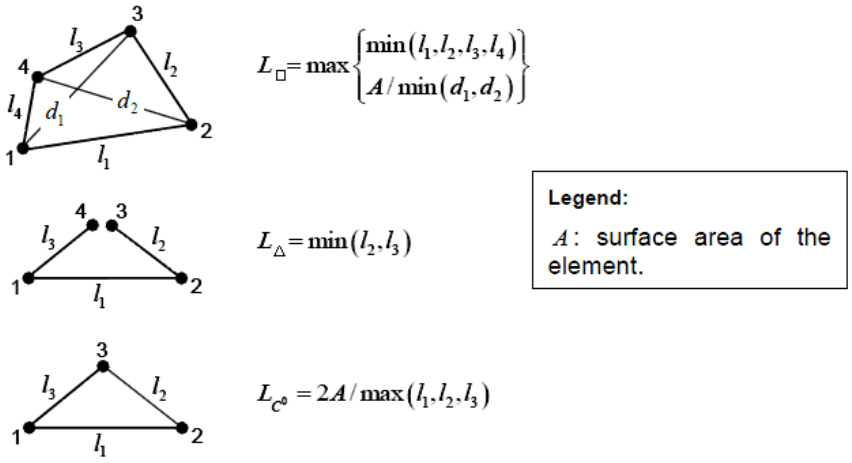

Figure 3.3: Shell element time steps, [17].

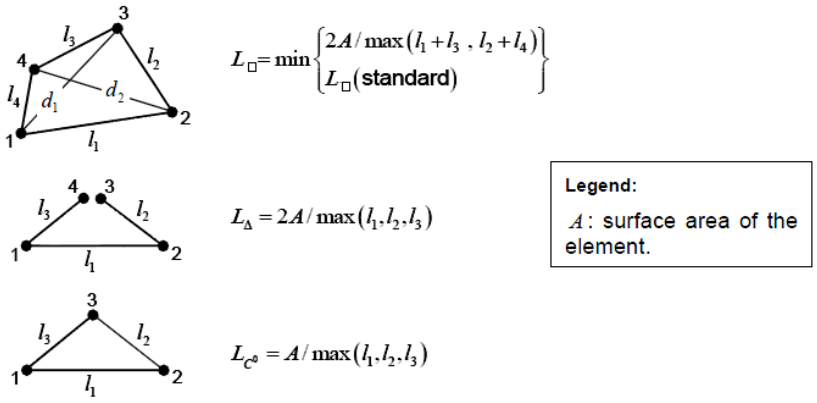

Figure 3.4: Shell element stringent time steps, [17].

3.2 Modal analysis

3.2.1 Implicit simulation

PAM-CRASH modal analysis is performed with the implicit solver because it involves matrix inversion which is available in the implicit code.

3.2.2 Free dynamic vibration - real eigenvalues

Many time-dependent problems can be reduced to a system of ordinary differential equations of the characteristic form given by, [64]

$$\mathbf{M\ddot{u} + C\dot{u} + Ku + f = 0} \tag{3.19}$$

If no damping or forcing terms exist in the dynamic problem of eq. 3.19 it reduces to, [64]

$$\mathbf{M\ddot{u} + Ku = 0} \tag{3.20}$$

A general solution of such an equation may be written as

$$\mathbf{u} = \bar{\mathbf{u}} \exp(i\omega t) \tag{3.21}$$

the real part of which simply represents a harmonic response as $\exp(i\omega t) \equiv \cos\omega t + i \sin\omega t$, [64].

Then on substitution we find that ω can be determined from, [64]

$$\left(-\omega^2 \mathbf{M} + \mathbf{K}\right) \bar{\mathbf{u}} = 0. \tag{3.22}$$

where ω^2 is an eigenvalue and ω is the natural frequency.

This is a general linear eigenvalue problem and for non-zero solutions the determinant of the above coefficient matrix must be zero, [64]:

$$\left|-\omega^2 \mathbf{M} + \mathbf{K}\right| = 0 \tag{3.23}$$

Such determinat will in general give n positive values of ω^2 when the size of the matrices $\mathbf{K}$ and $\mathbf{M}$ is $n \times n$, providing the matrices $\mathbf{K}$ and $\mathbf{M}$ are symmetric positive definite, [64].

While the solution of eq. 3.23 cannot determine the actual values of $\mathbf{u}$ we can find n vectors $\bar{\mathbf{u}}_j$ that can give the proportions for the various terms. Such vectors are known as the eigenvectors and are made unique by normalizing so that, [64]

$$\bar{\mathbf{u}}_j^T \mathbf{M} \bar{\mathbf{u}}_j = 1; \quad j = 1, 2, \ldots, n \tag{3.24}$$

At this stage it is useful to note the property of modal orthogonality, *i.e.*, that, [64]

$$\bar{\mathbf{u}}_i^T \mathbf{M} \bar{\mathbf{u}}_j = 0; \quad (i \neq j) \quad and \quad \bar{\mathbf{u}}_i^T \mathbf{K} \bar{\mathbf{u}}_j = 0; \quad (i \neq j) \tag{3.25}$$

To find the actual eigenvalues it is seldom practical to write the polynomial expanding the determinant given in eq 3.23 and alternative techniques have to be developed, [64].

In some processes the starting point is the standard eigenvalue problem given by

$$\mathbf{H}\mathbf{x} = \lambda \mathbf{x} \tag{3.26}$$

in which H is a symmetric matrix and hence has real eigenvalues. Equation 3.22 can be written as

$$\mathbf{M}^{-1} \mathbf{K} \bar{\mathbf{u}} = \omega^2 \bar{\mathbf{u}} \tag{3.27}$$

on inverting $\mathbf{M}$ with $\lambda = \omega^2$, but symmetry is in general lost, [64].

If, however, we write in triangular form

$$\mathbf{M} = \mathbf{L}\mathbf{L}^T \quad and \quad \mathbf{M}^{-1} = \mathbf{L}^{-T}\mathbf{L}^{-1} \tag{3.28}$$

in which L is a lower triangular matrix (*i.e.*, has all zero coefficients above the diagonal), eq. 3.22 may now be written as, [64].

$$\mathbf{K}\bar{\mathbf{u}} = \omega^2 \mathbf{L}\mathbf{L}^T \bar{\mathbf{u}} \tag{3.29}$$

Calling

$$\mathbf{L}^T \bar{\mathbf{u}} = \mathbf{x} \tag{3.30}$$

and multiplying by $\mathbf{L}^{-1}$ we have finally

$$\mathbf{H}\mathbf{x} = \omega^2 \mathbf{x} \tag{3.31}$$

in which

$$\mathbf{H} = \mathbf{L}^{-1}\mathbf{K}\mathbf{L}^{-T} \tag{3.32}$$

which is of the standard form of eq. 3.26, as $\mathbf{H}$ is now symmetric, [64].

Having determined ω^2 the modes of $\mathbf{x}$ are found, and hence by use of eq. 3.30 the modes of $\bar{\mathbf{u}}$ [64].

3.2.3 Eigen extraction with implicit analysis

A model of *N* degrees of freedom (DOF) has theoretically a maximum of *N* Eigen modes. Due to data management and CPU cost considerations, it is impossible to extract all modes of an industrial model. The extraction has to consist of a limited number of modes, however sufficient to represent faithfully the system response for the user purpose, [17].

PAM-CRASH implicit has two Eigen solvers, [17]:

- Block IRAM: the eigen solver uses the Implicity restarted Arnoldi method, computing eigenvalues by block. Native, direct method, available for DMP and efficient for low-frequency analysis (hundreds of modes) of all model sizes;
- AMLS: the eigen solver uses the automated multilevel substructuring method. Approximate method and efficient for high frequency (thousands of modes) and large size models.

AMLS method is recommended only for mechanical eigen modes extraction, [17].

Block IRAM method is generally used when a small/medium number of eigenvalues is searched. AMLS is generally used when searching numerous eigenvalues. Block IRAM consumes more RAM whereas AMLS consumes more disk space, [17].

Algorithms are available in the following links:

- http://ftp.mcs.anl.gov/pub/tech_reports/reports/P649.pdf
- http://www.cs.sandia.gov/~rblehou/amls-rev.pdf

3.3 Shell elements

3.3.1 Reduced and selective integration

When evaluating the element stiffness matrices a Gaussian quadrature rule is commonly used. Nevertheless, a full quadrature rule may lead to erroneous results in certain constrained problems. This is the case in the presence of thin plate and shell elements where the shear terms may cause an over-stiff solution for bending problems, usually termed as "locking". A common remedy relies in reduced integration techniques, in which a lesser number of Gauss integration points are used to evaluate those terms. Typically, selective reduced integration or reduced integration techniques may be used to avoid shear "locking" in thin plates and shells, [65, 66].

In selective reduced integration, the bending term is integrated with the normal rule, whereas the shear term is integrated with a lower-order rule. In reduced integration, both the bending and shear terms of the element stiffness matrices are integrated with the same reduced rule, [65].

A considerable gain in computing time may also result in large problems, but special stabilization terms must be added in order to avoid spurious deformations patterns, associated to zero energy deformation modes, which may be induced in the solution, [67].

3.3.2 Hourglassing

Quotted from, [68]: *"Hourglass modes are nonphysical, zero-energy modes of deformation that produce zero strain and no stress. Hourglass modes occur only in under-integrated (single integration point) solid, shell, and thick shell elements..."*

Hourglassing is a very common problem of under-integration techniques used in the numerical integration of element stiffness (or other quantities), and is especially common in one point integration elements used in explicit codes, [63].

It is a phenomenon that can be easily excited in regular meshed structures, or poor loading, [63].

Essentially, hourglass modes are certain element deformation modes that erroneously predict zero deformation energy at the element integration points, [63].

Two methods could be used to control or eliminate hourglassing, [63, 68]:

1. Fully constrain all nodes at the boundary (this would be the best modelling approach);
2. Use a different element type that does not have hourglass modes, for example "fully" or "selectively reduced" integrated elements (downsides: more exspensive and more unstable in large deformation applications like crash simulation), or triangular elements (regarding its overly stiff behaviour in some applications);
3. Refine mesh.

3.4 PAM-CRASH constraints

PAM-CRASH constraints used in the dynamic behaviour analyses are defined in the following sections.

3.4.1 Rigid bodys

A rigid body is an element of infinite stiffness defined on a number of nodes. Its most general movement consists of spatial rotations and translations. The links with the rest of the model are fixed, *i.e.* moments and forces are transmitted. The motion of a rigid body is completely defined by the translations and rotations of its center of gravity, [69].

Boundary conditions for the rigid body must be applied to the center of gravity (COG) node only, [69].

In general, no nodes should belong to both rigid body and other nodal constraint, nor should nodes belong to more than one rigid body, [69].

3.4.2 Multiple to one node constraint

A multiple nodes to one node constraint (*MTOCO*) ties one or several translational or rotational degrees of freedom of the dependent nodes to the corresponding degrees of freedom of the independent node, [69].

The constraint equations are, [69]:

$$\begin{cases} \overrightarrow{U}\left(n_d\right) = \vec{U}\left(n_i\right) + \vec{\theta}\left(n_i\right) \wedge \overrightarrow{d} \\ \vec{\theta}\left(n_d\right) = \vec{\theta}\left(n_i\right) \end{cases}$$

where:

- $\overrightarrow{U}\left(n_d\right)$ and $\overrightarrow{U}\left(n_i\right)$ are the displacement vectors of the dependent and independent nodes respectively;
- $\overrightarrow{\theta}\left(n_d\right)$ and $\overrightarrow{\theta}\left(n_i\right)$ are the rotation vectors of the dependent and independent nodes respectively;
- $\overrightarrow{d}$ is the vector defined by nodes n_i and n_d.

No nodes can belong to both a rigid body and a *MTOCO* set, nor can dependent nodes belong to more than one *MTOCO* set for the same constrained degrees of freedom. An independent node can be shared by several *MTOCOs* and can also be a dependent node from another *MTOCO*. Dependent nodes cannot have other imposed kinematic conditions on the constrained DOF, [69].

FEM Software

4.1 Abaqus

Abaqus is a multi-purpose engineering FEA software from Dassault Systémes, very popular with academic and research institutions due to a wide material modeling capability and the program's ability to be customized. Abaqus also provides a good collection of multiphysics capabilities, such as coupled acoustic-structural, piezoelectric, and structural-pore capabilities, making it attractive for production-level simulations where multiple fields need to be coupled.

The Abaqus finite element system includes:

- Abaqus/Standard, a general-purpose finite element program;
- Abaqus/Explicit, an explicit dynamics finite element program;
- Abaqus/CAE, an interactive environment used to create finite element models, submit Abaqus analyses, monitor and diagnose jobs, and evaluate results; and
- Abaqus/Viewer, a subset of Abaqus/CAE that contains only the postprocessing capabilities of the Visualization module.

This software was very useful during the project first stages. The main objectives for use of Abaqus FEA capabilities were:

- Generation of FE parametric meshes;
- Meshing technique validation by studying the mesh configuration influence in results of geometric stress concentration factor for a plate with central hole;
- Study of mesh refinement influence on FEA results;
- Familiarization with the influence of the use of shell elements or solid elements on the FEA results;
- Modal analysis of structures;
- Stress intensity factor determination;
- Aplication of static and dynamic loads on structures;
- Study of the linear elastic behaviour of a conceptual and simplified cross car beam undergoing static loads;
- Modal analysis of a cross car beam.

4.1.1 Benchmark cases

The following benchmark cases are some of the relevant problems analysed in the initial stage of this thesis, in order to understand the use and capabilities of the software.

Modal analysis example

The objective of this benchmark case was to experience the Abaqus potential in modal analysis. The object analyzed was a rectangular plate, whose dimensions in mm are defined in Figure 4.1, with a thickness of 20 mm. The displacements of the plate's 4 edges are constrained but rotations are allowed as depicted in Figure 4.2. The FEA was realized with 4 node quadrilateral shell elements, [70].

The Abaqus designation for the standard linear shell element used is S4R: A 4-node doubly curved thin or thick shell, reduced integration, hourglass control, finite membrane strains, [71].

Plate material is a steel with the following mechanical properties: $\mathrm{E} = 210 \times 10^9 Pa$; $\nu = 0.3$; $\rho = 8700\, kg/m^3$, [70].

A 10 mode truncation modal analysis was carried out with the results being: $\omega_1 = 13.423\ Hz$; $\omega_2 = 30.225\ Hz$; $\omega_3 = 37.882\ Hz$; $\omega_4 = 54.403\ Hz$; $\omega_5 = 59.489\ Hz$; $\omega_6 = 81.097\ Hz$; $\omega_7 = 83.193\ Hz$; $\omega_8 = 97.144\ Hz$; $\omega_9 = 103.26\ Hz$; $\omega_{10} = 125.11\ Hz$.

The modes shapes are illustrated in Figure 4.3.

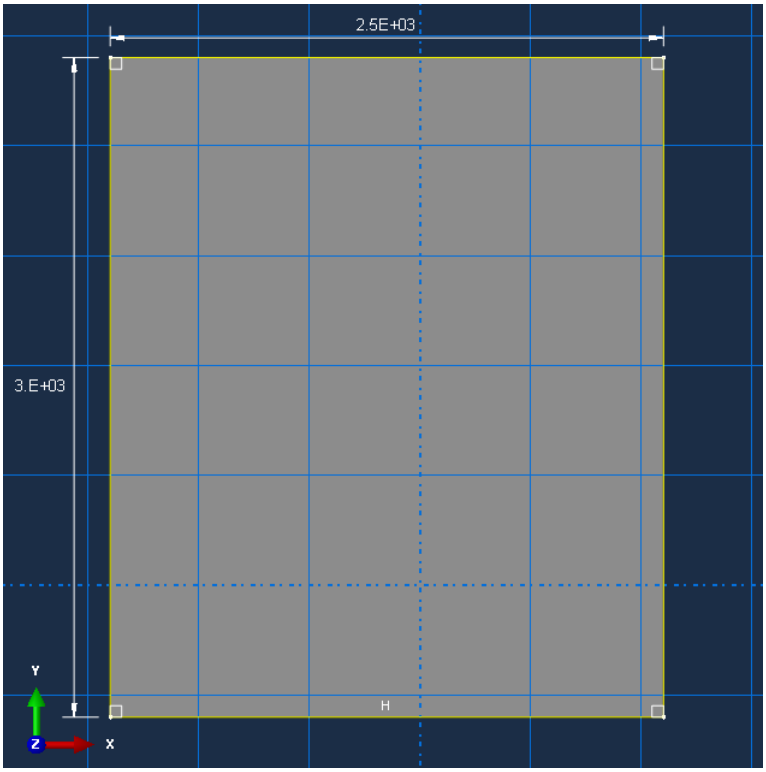

Figure 4.1: Plate dimensions in mm.

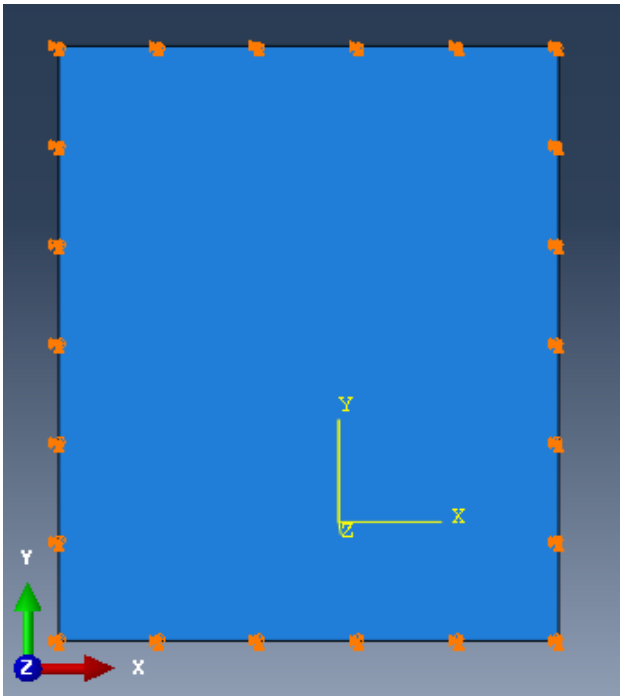

Figure 4.2: Plate boundary conditions.

Dynamic load

This benchmark case is of extreme importance for the topic of impact on structures as it addresses dynamic loading aplication in Abaqus. The problem consists of modelling a masonry wall under a blast explosion. The wall is rectangular with a thickness of 215mm. The remaining dimensions are defined in Figure 4.4. The FEA was undergone in explicit mode with a linear elastic material law. Model discretisation was achieved with 8 node hexaedral solid elements. The wall has its lateral faces constrained in all 6 DOF, Figure 4.5. The blast impact was simulated with a uniform pressure applied in the exposed faced defined in Figure 4.6, [72].

The Abaqus designation for the explicit linear solid element used is C3D8R: An 8-node linear brick, reduced integration, hourglass control, [71]. The analysis is performed with explicit code.

Wall section properties were defined as follows: $\mathrm{E} = 11.8 \times 10^9 Pa$; $\upsilon = 0.15$; $\rho = 2000\, kg/m^3$, [72].

Wall points displacement magnitude during the blast is illustrated in Figure 4.7.

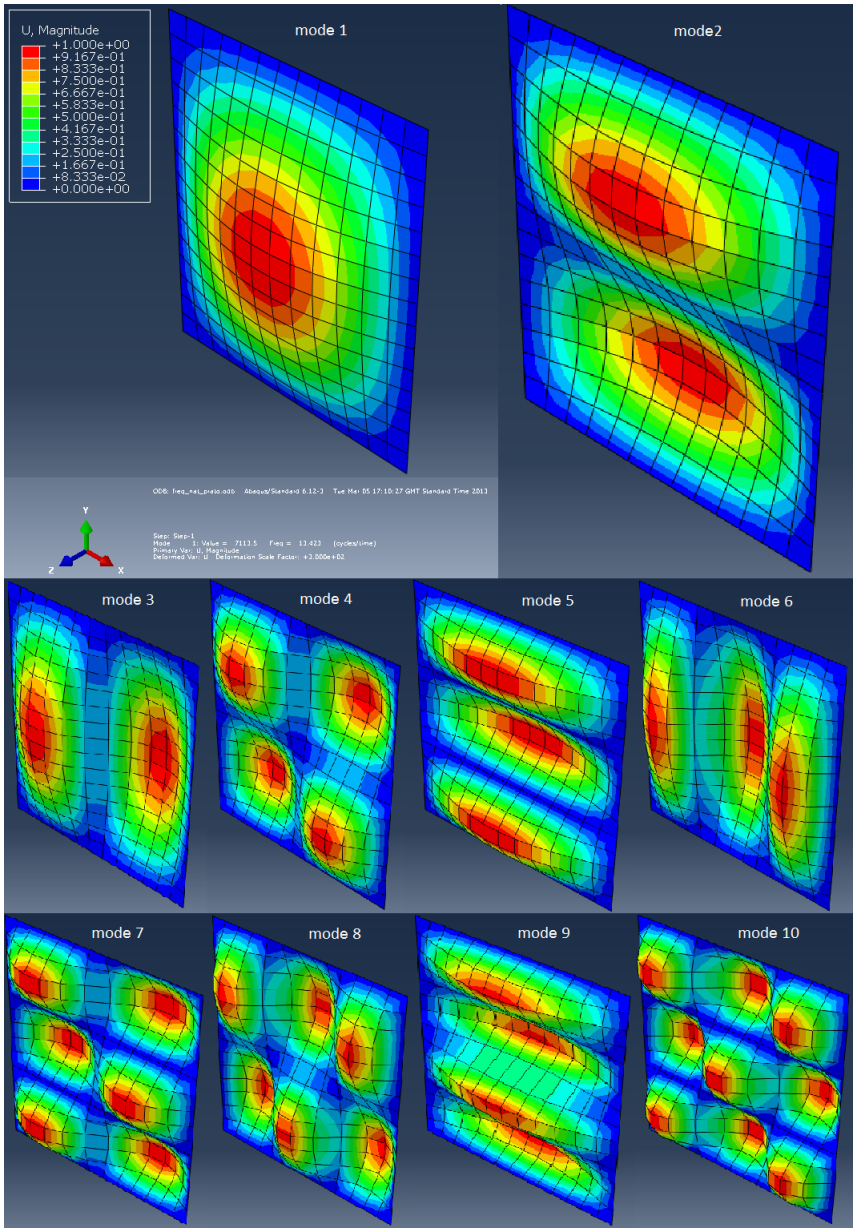

Figure 4.3: Plate first 10 mode shapes.

Stress intensity factor for a center-cracked plate

Stress intensity factor controles the stress state near the tip of a crack caused by a remote load. For a center-cracked plate loaded in mode I, Figure 4.8, the value of the stress intensity factor is dependent from the load applied (σ), the crack length $(2a)$and from plate geometry (Y). This value is obtained by the following expression, [18]:

$$K_I = Y\sigma\sqrt{\pi a} \tag{4.1}$$

When the plate has infinite dimensions, [18] $Y = 1$ and eq. 4.1 becomes

$$K_I = \sigma\sqrt{\pi a} \tag{4.2}$$

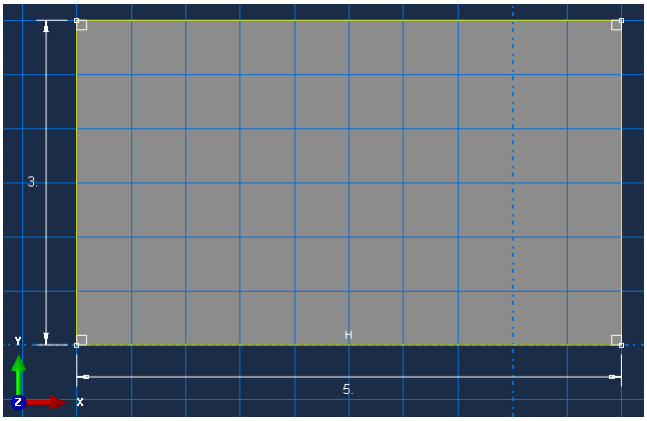

Figure 4.4: Wall dimensions in m.

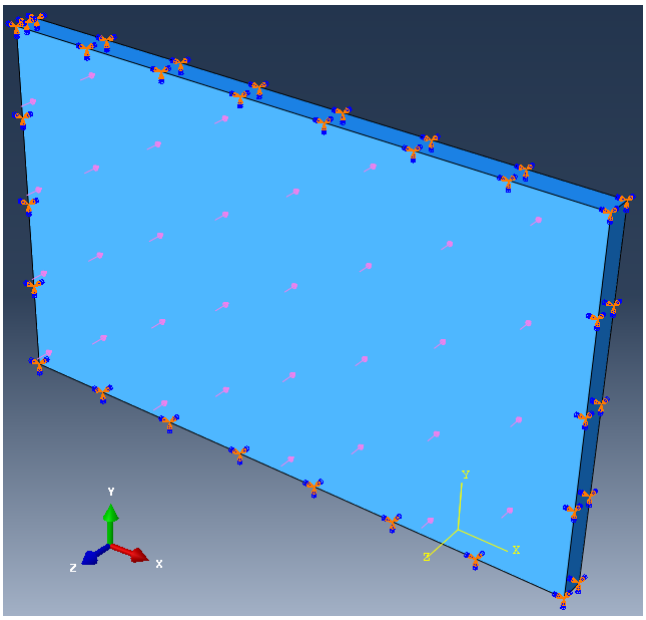

Figure 4.5: Wall boundary conditions and load applied.

For the present analysis, only 1/4 of the plate was modeled due to symmetry, Figure 4.9. The plate is made of steel $\left(E = 210 \times 10^9 Pa;\ \nu = 0.3\right)$with finite width $\mathrm{W} = 1000mm$ and a central crack with a length of $2a = 100mm$. The remote load $(\sigma = 1Pa)$ is in mode I.

In Figure 4.10, the 1/4 of plate crack zone is highlighted in red, with no restrictions for y-direction displacements. Loads and boundary conditions are also illustrated in this figure.

16 FEAs were realized in Abaqus with diferent refinements in the crack zone of the plate's shell mesh, Figure 4.11. Abaqus determines the J-Integral value from which the stress intensity factor is calculated afterwards by the following expression, [18]

$$K_I = \sqrt{EJ} \tag{4.3}$$

The Abaqus designation for the standard linear shell element used is CPS4R: A 4-node bilinear plane stress quadrilateral, reduced integration, hourglass control, [71]. The analysis is implicit.

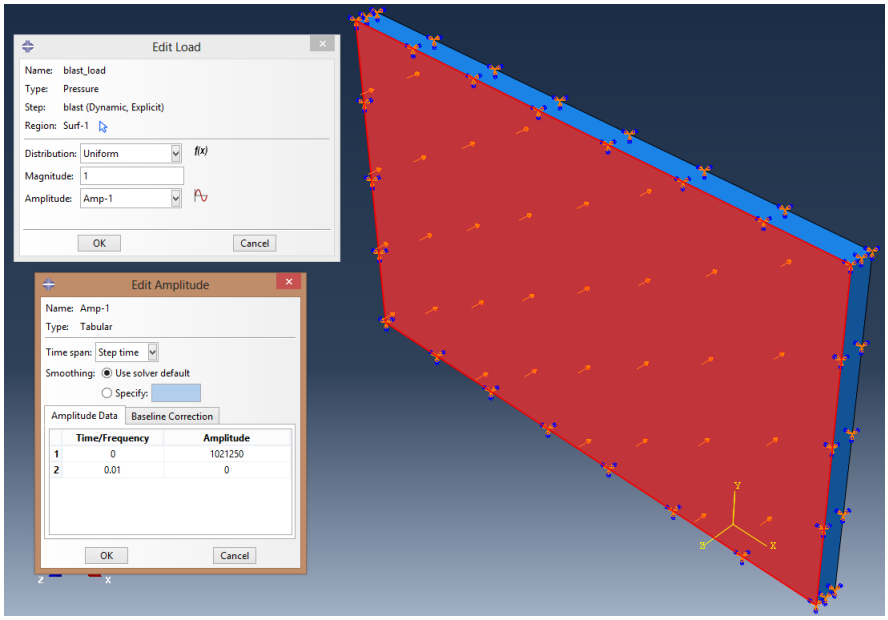

Figure 4.6: Dynamic Load amplitude definition in Abaqus.

In order to evaluate the quality Abaqus FEAs results of stress intensity factor, these values were compared with the value for an infinite plate (*Y=1,* because we are dealing with a low a/W ratio value) and with the values of approximate solutions given by Irwin, [73], $\left(Y = \sqrt{\frac{W}{\pi a}\tan\frac{\pi a}{W}}\right)$ and by Feddersen, [74], $\left(Y = \sqrt{\sec\frac{\pi a}{W}}\right)$.

Cracks in plates of finite size are of great practical interest, but for these cases no closed form solutions are available. These problems are difficult due to boundary conditions. However, approximate solutions can be obtained for a center-cracked finite width plate, [18].

First consider an infinite plate with an infinite row of evenly spaced collinear cracks, Figure 4.12, [18].

Through Westergaard solutions, Irwin, [73], arrived at the following solution for this case,

$$K_I = \sqrt{\frac{W}{\pi a}\tan\frac{\pi a}{W}}\sigma\sqrt{\pi a} \tag{4.4}$$

If the plate is cut along the lines AB and CD one obtains a finite strip of width *W*, containing a central crack of length 2*a.* Therefore, this solution is approximatly valid for a plate of finite width W. Infinite width plate bears stresses along the edges AB and CD , Figure 4.13, whereas in the finte width plate edges are stress free, [18].

Isida developed mapping functions to derive stress concentration factors. These can be used to get the stress intensity factor for finite plate to any degree of accuracy. The result is presented as, [18],

$$K_I = Y\sigma\sqrt{\pi a} \tag{4.5}$$

where Y is a polynomial function in *a/W*. Feddersen, [74], noted that this function is very closely approximated by $\sqrt{\sec\frac{\pi a}{W}}$. Thus, another approximated solution for the stress intens-

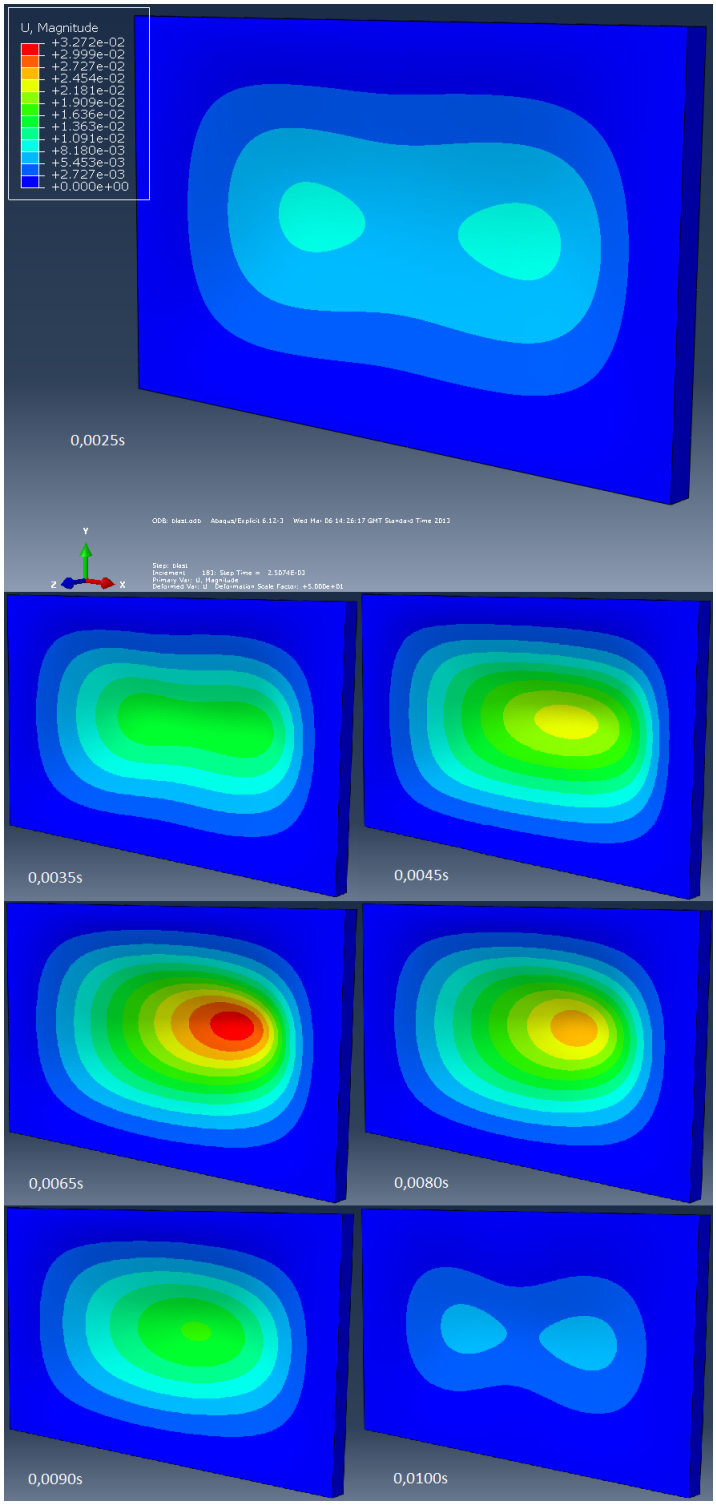

Figure 4.7: Wall points displacement magnitude during the blast.

ity factor is giver by, [18],

$$K_I = \sqrt{\sec \frac{\pi a}{W}} \sigma \sqrt{\pi a} \tag{4.6}$$

A comparisson of finite width correction factors defined by Irwin, Isida and Feddersen is

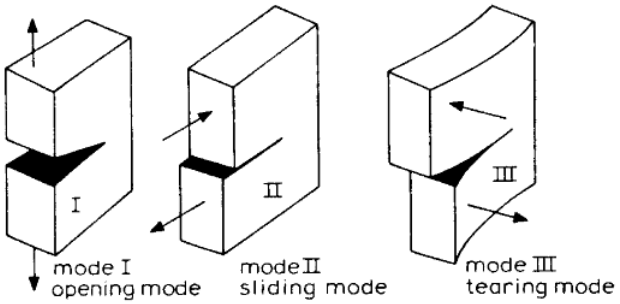

Figure 4.8: The three modes of cracking, [18].

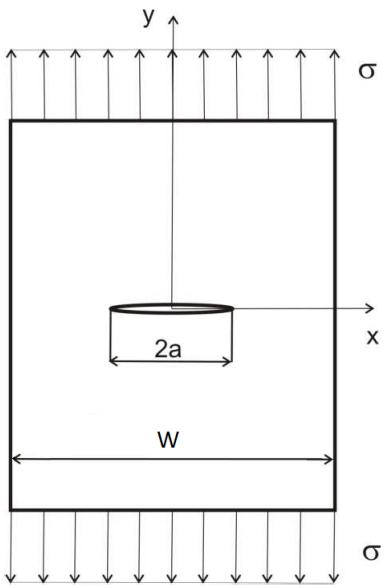

Figure 4.9: Center-cracked plate with finite width W, loaded in mode I.

illustrated in Figure 4.14.

Table 4.1 presents the data and results of the FEA in Abaqus and the percentage difference between the determined values and Irwin, Feddersen and infinite plate solutions.

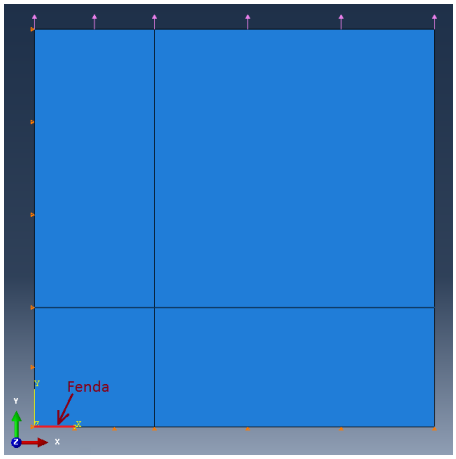

Figure 4.10: Loads and boundary conditions of the 1/4 plate model.

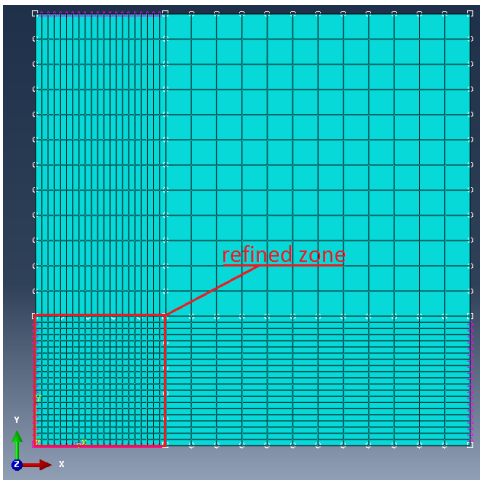

Figure 4.11: Shell mesh used in analysis n°5.

Percentage difference evolution of the stress intensity factor determined by FEA in Abaqus is illustrated in Figure 4.15.

Difference curves behaviour with the mesh configuration are very similar. The FEA results are very close to the analitical approximated solutions evidenced by the low percent error which is almost always bellow 1%, reaching the minimum value of 0.0145% in Irwin's solution reference curve. For rough meshes, FEA results are very close to the infinite plate solution. However, as the mesh was successively refined, FEA results tend to get closer to Irwin and Feddersen solutions. After a certain level of mesh refinement, all errors tend to rapidly increase until it levels out, Figure 4.16. This allows us to conclude that excessive element mesh refinement requires an extra computational time and tends to degrade results.

Meshing technique validation by the analyses of stress concentration factor for square plate with central hole

In this section, the problem of stress concentration in an infinite plate with a central circular hole, Figure 4.17, subjected to an unidirectional traction load (σ_0), is considered.

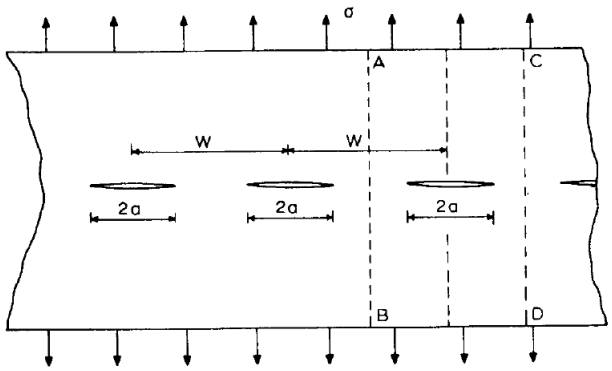

Figure 4.12: Infinite Plate with collinear cracks, [18].

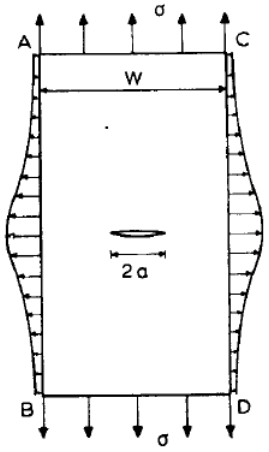

Figure 4.13: Stresses on the edges of strip cut from infinite plate with collinear cracks, [18].

The material of the plate is steel with the following elastic properties: $\mathrm{E} = 200 \times 10^9 Pa$ and $\nu = 0.3$.

For the FEA plate's geometry infinite dimensions were approximated by a square whose edges length were an order of magnitude greater than the diameter of the central hole. Plate's thickness is 5mm.

The theoretical solution for this problem is schematically represented in Figure 4.18. Considering a coordinate system with origin in the hole geometric center, points A and B are localized in the hole perimeter and are the perimeter points that intersect x and y axes, respectively. Y-direction stress value in point A is 3 times the remote load value. As one moves in the x-direction and deviates from th hole, the stress tends towards remote load value, Figure 4.18 a). Point B stress value in x-direction is equal to the remote load one but is a compression stress, Figure 4.18 b), [19].

Abaqus's FEA was computed with shell elements as they enable thin structures modelling with less elements than a solid mesh and without compromising results. Therefore computing time is significantly reduced. The Abaqus designation for the standard linear shell element used is CPS4R: A 4-node bilinear plane stress quadrilateral, reduced integration, hourglass control, [71]. The analysis performed with implicit code.

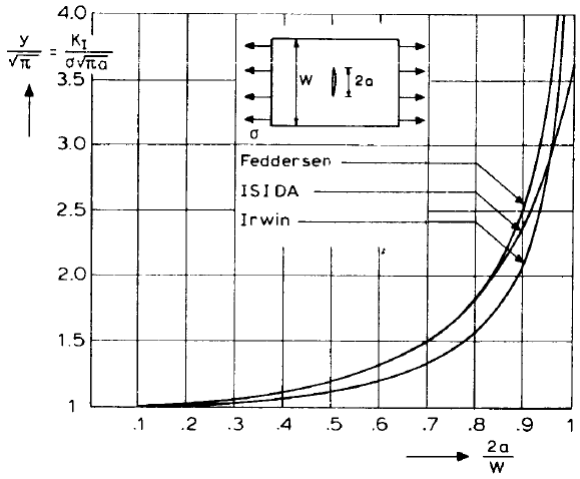

Figure 4.14: Finite width corrections for center cracked plate, [18].

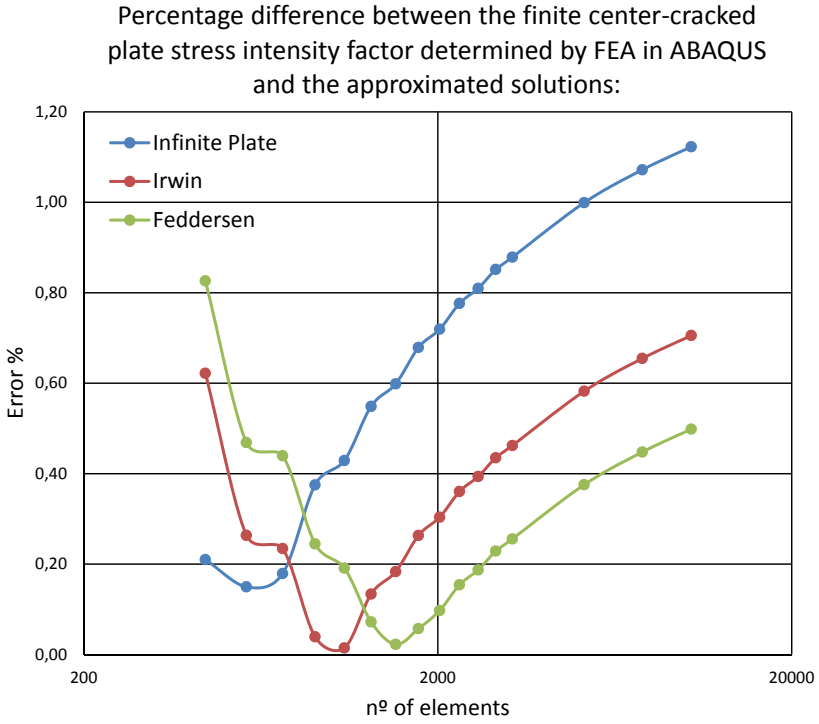

Figure 4.15: Percentage difference evolution with mesh configuration of the finite center-cracked plate stress intensity factor determined by FEA in Abaqus, logaritmic scale.

Taking advantage of the plate symmetry, only 1/4 of the plate needs to be modeled for the plate analysis by adding the necessary boundary conditions, Figure 4.19. Therefore computing is reduced once again.

Mesh configuration is illustrated in Figure 4.20. The 1/4 plate model uses 3176 shell elements.

1/4 plate's stress distributions in y and x directions are illustrated in Figures 4.21 and 4.22, respectively.

The FEA results achieved with this mesh configuration were satisfactory with a percent

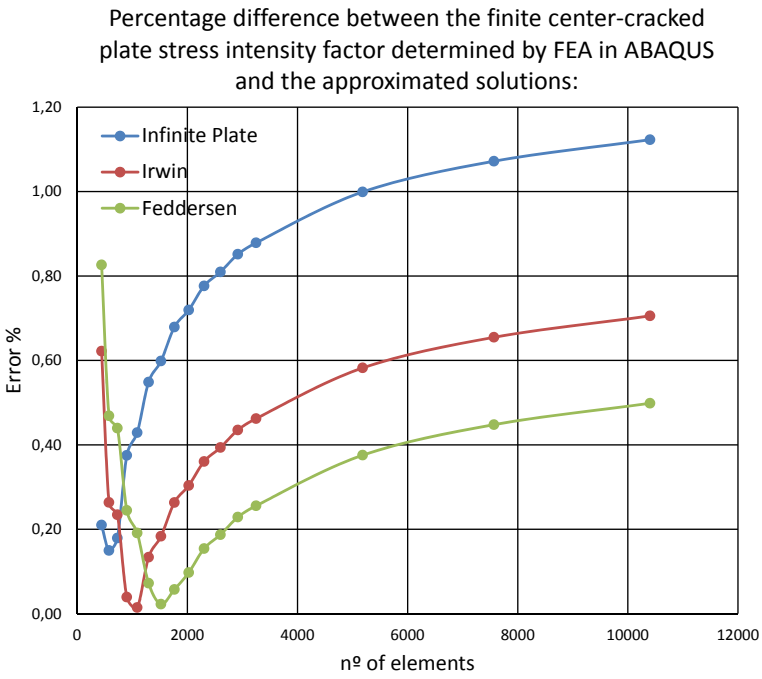

Figure 4.16: Percentage difference evolution with mesh configuration of the finite center-cracked plate stress intensity factor determined by FEA in Abaqus.

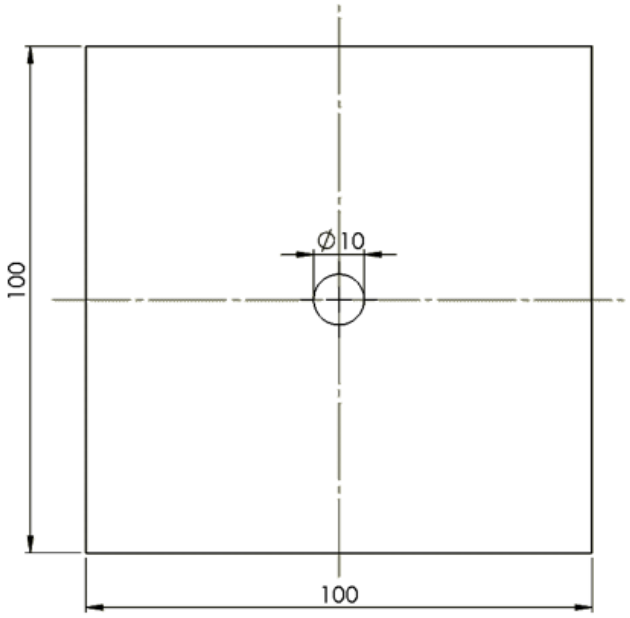

Figure 4.17: Plate dimensions in mm.

error of 2.4% in point A y-direction stress and of 3.27% in point B x-direction stress, comparing with theoretical values.

With the aim of studying Abaqus's FEA results percent error behaviour with mesh configuration, a set of 20 analyses of the 1/4 center hole plate model were computed with the same type of shell elements. The model mesh was being successively refined in hole surroundings,

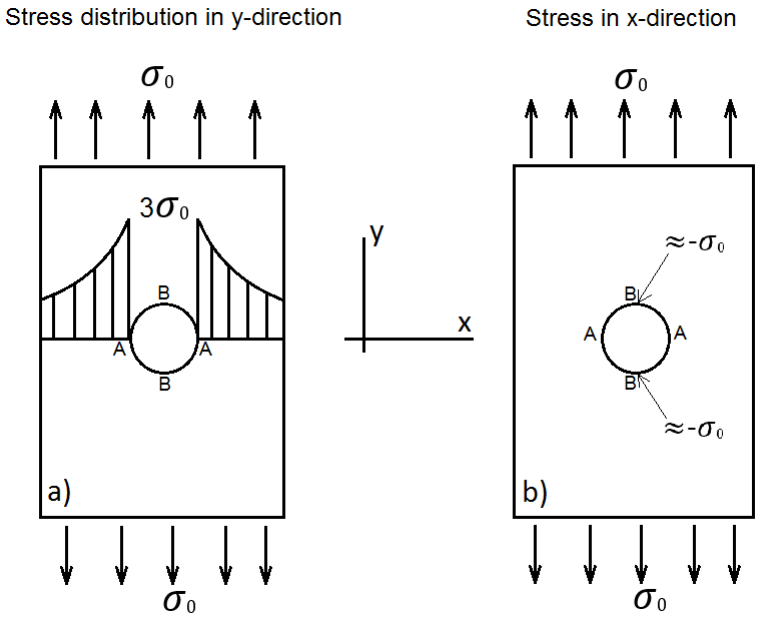

Figure 4.18: Schematic illustration of the stress concentration factor in an infinite plate with a central circular hole, subjected to a traction load in the y-drirection, [19].

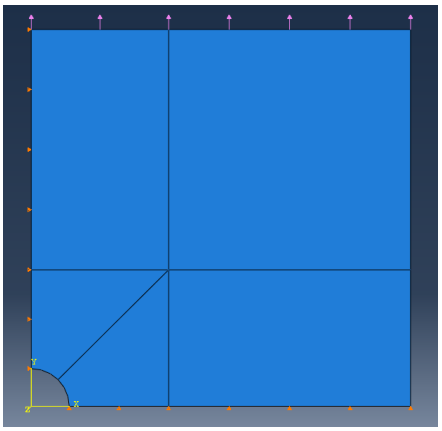

Figure 4.19: Load, boundary conditions and seeds guidelines of the 1/4 plate model.

region visible in Figures 4.23 and 4.24. In order to enable a valid comparison between the results of the 20 analyses, it was defined as a rule of uniformity of the mesh generation that the 2 elements located at the first ring of elements around the hole and that contains nodes belonging to the obliqual seed line segment, should always be defined with equal length between obliqual seeds and perimeter seeds after each successive refinement. These 2 elements boundaries are defined in Figure 4.25.

Mesh configuration parameters as well as results and percent error are found in Table 4.2.

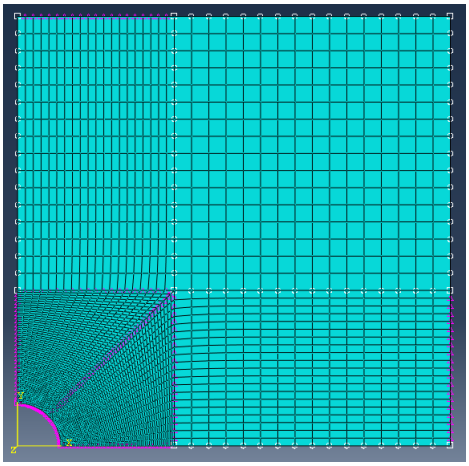

Figure 4.20: 1/4 central hole plate shell mesh.

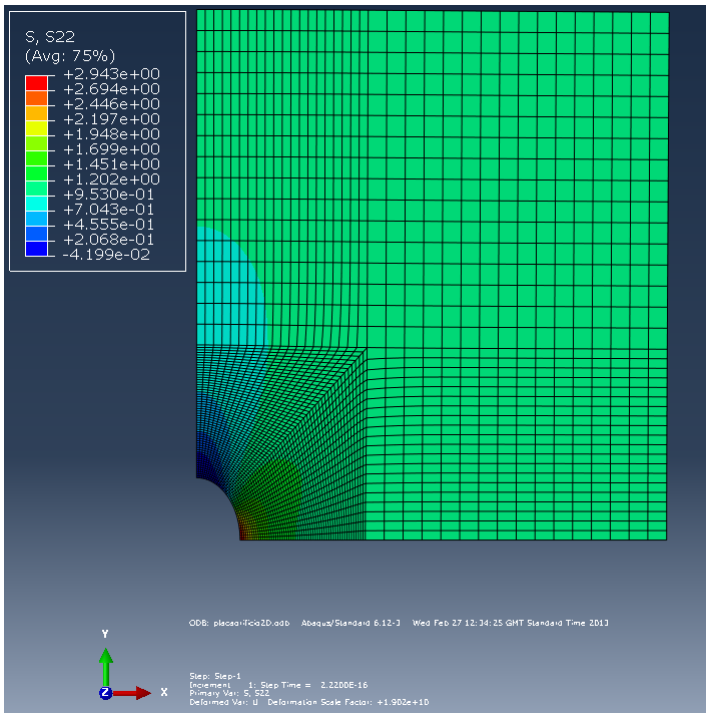

Figure 4.21: 1/4 central hole plate stress distribution in y-direction.

Results percent error behaviour with mesh refinement in the hole surroundings is illustrated in Figure 4.26.

Looking to both curves, it appears that x-direction stress at point B is more sensitive to the mesh refinement than y-direction stress at point A. This phenomenon lies in the fact that the region of maximum stress concentration in y-direction is more extensive than the region of maximum stress concentration in x-direction. Another fact that can explain the difference in sensitivities and also the different number of elements from which results in A and B begin to diverge is the refining zone shape being rectangular and, therefore, in the successive refinements, element size varies differently in the two points. This variation of the element size at point A and point B with progression analysis results error can be seen

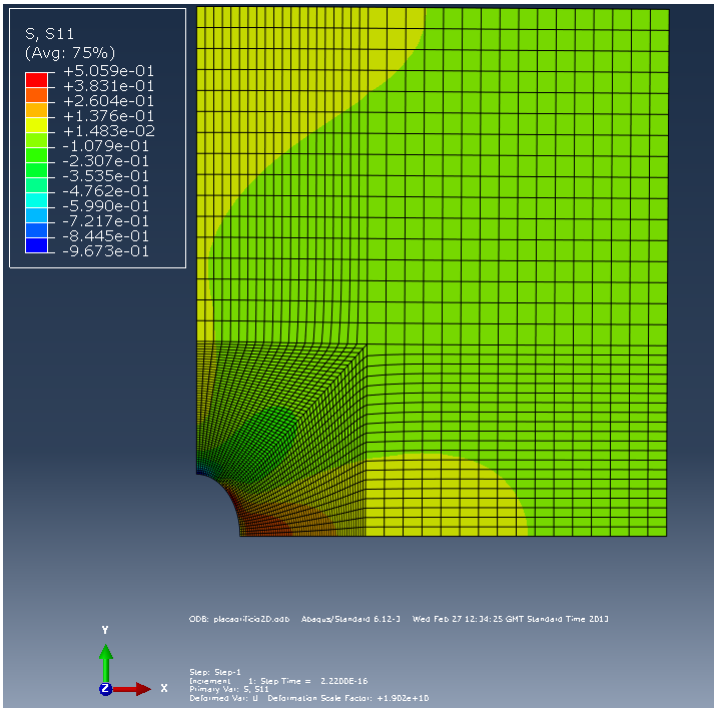

Figure 4.22: 1/4 central hole plate stress distribution in x-direction.

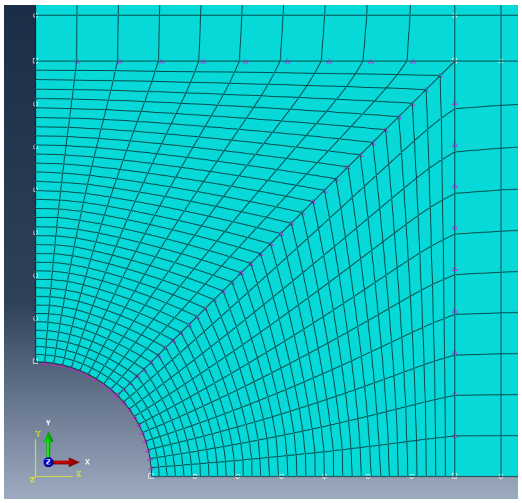

Figure 4.23: Refined zone of the 1256 shell elements mesh.

in Figure 4.27. Another feature visible in Figure 4.27 is the proportional change in the size of two elements with mesh refinement. This confirms the uniformity in meshing after successive refinements.

4.1.2 Cross car beam concepts analysis

This section will present three static analysis in the linear elastic domain of two simplified and strictly conceptual models of a cross car beam structure. Furthermore, the modal analysis of the second one, obtained using the technique of finite element analysis in Abaqus, is also presented.

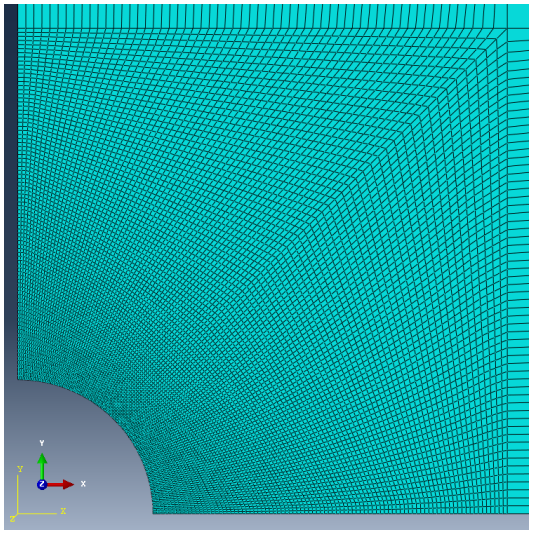

Figure 4.24: Refined zone of the 26506 shell elements mesh.

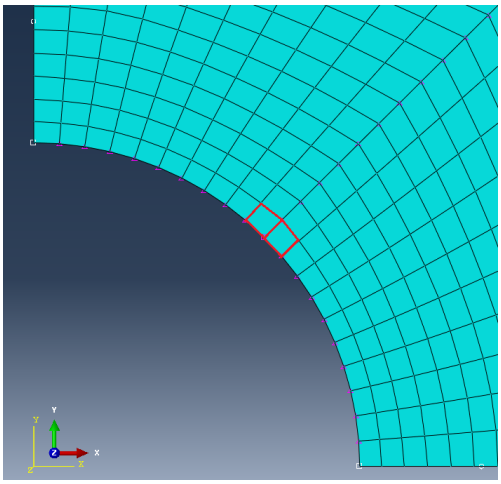

Figure 4.25: Elements defined by 2 pairs of seeds with equal length (highlighted).

The material of the two models is steel with the following mechanical properties:

- $\mathrm{E} = 200 \times 10^9\, Pa$; $\nu = 0.3$; $\rho = 8700\, kg/m^3$.

The Abaqus specification for the standard finite elements used in these concepts analysis is, [71]:

- linear shell element S4R: A 4-node doubly curved thin or thick shell, reduced integration, hourglass control, finite membrane strains;
- linear solid element C3D8R: An 8-node linear brick, reduced integration, hourglass control.

Concerning hourglass effect, common on under-integrated elements, Abaqus element's library provides shell elements with hourglass control as is the case of shell element used in the present example, S4R and C3D8R.

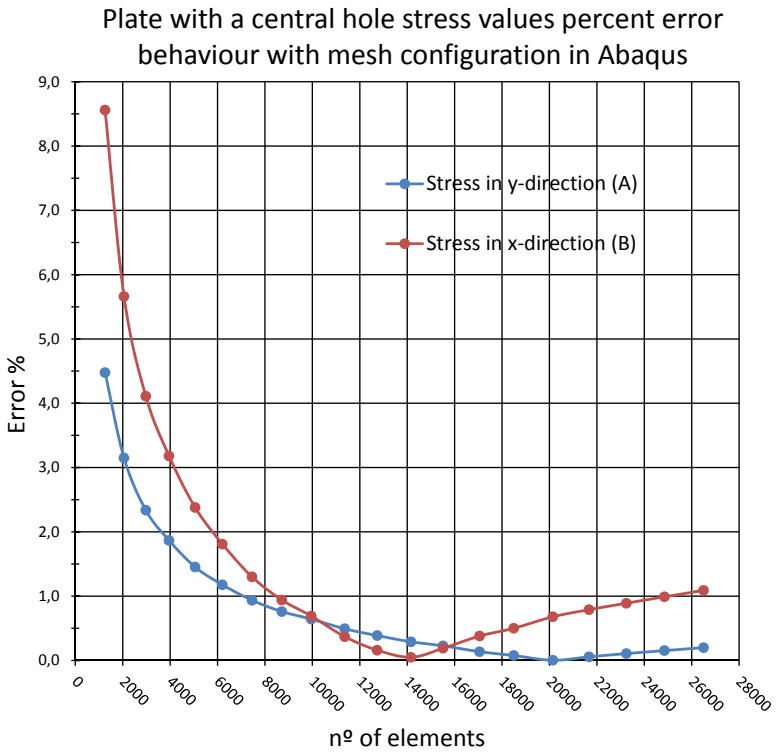

Figure 4.26: Stress values percent error behaviour with mesh configuration for the present plate with a hole example.

First model: simplified tubular concept structure

As an initial approach to the finite element analysis in Abaqus, a very simplified and merely conceptual structure of a cross car beam was modeled. The goal was to perform a linear elastic analysis of a basic model with dimensions identical to those of the actual structure where meshing would not cause a major challenge, applying some illustrative static loads in the same spots where on a car crash event large deformations and rotations occur. The geometry and dimensions of this structure are defined in Figure 4.28.

Two finite element meshes were generated for the first model, one with solid elements, Figure 4.29, and the other one with shell elements, Figure 4.32.

The FEA modeling with a solid elements, Figure 4.29, is more accurate than modeling with shell elements as it prevents problems like hourglass effect and enables the knowledge of structure behaviour along the entire thickness. However, the analysis is heavier to compute requiring a greater effort by the processor and it is, therefore, more time consuming.

Loads and boundary conditions of the solid meshed model are defined in Figure 4.30. The yellow vectors represent *body force* components $\left(strength/length^3\right)$ and violet vectores represent *surface traction* components $\left(strength/length^2\right)$. All load vectors' components have a magnitude of 1 N except the case of the *body force* highlighted in Figure 4.30 as it simulates the load in a critical component wich is the steering column bracket. The structure is constrained on the tops in all 6 DOF as depicted in Figure 4.30.

Figure 4.31 illustrates the von Mises stress distribution of the solid meshed model given

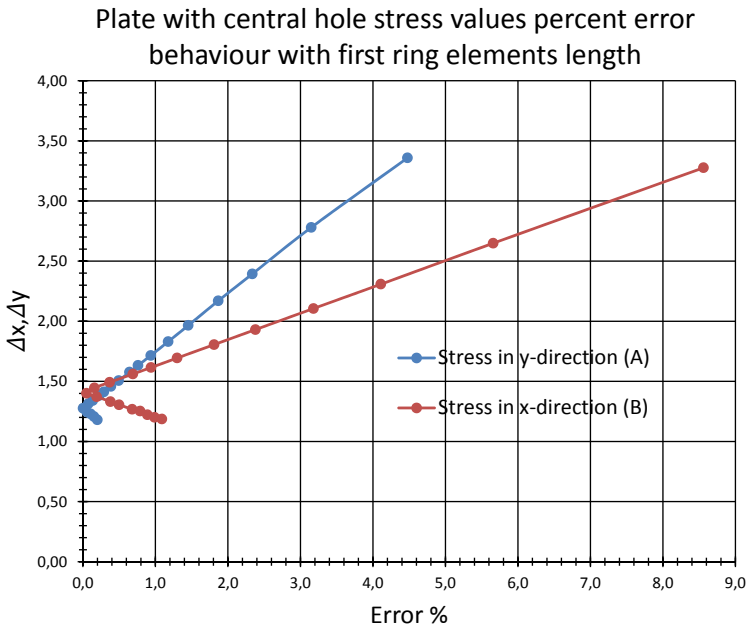

Figure 4.27: Results percent error in function of the greatest length of the elements located in points *A* and *B*.

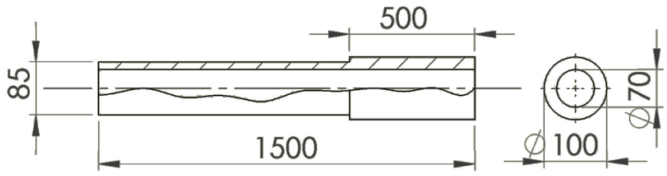

Figure 4.28: Simplified concept geometry and dimensions.

by the FEA in Abaqus. The deformations are with a sacale factor of 10^7.

Shell elements meshes, *e.g.* Figure *4.32,* save a lot of computing time since they allow thin structures modeling, *e.g.* cross car beams, with less elements without sacrificing the results. In addition, shells are a lot easier to mesh and are less prone to Jacobian errors that can occur when analyzing extremely thin structures.

Shell meshed model loads and boundary conditions are visible in Figure 4.33 and were set identically to the solid meshed model.

Figure 4.34 illustrates de von Mises stress distribution of the shell meshed model given by the FEA in Abaqus. The deformations are with a sacale factor of 10^7.

The maximum and minimum values of the von Mises stress computed with the shell meshed model do not match with the ones obtained with the solid meshed model because they only represent mid-surface stress distribution. Nevertheless, values are not very disparate. The computing time for the solid elements model was 78s, whereas the computing time for the shell model was 15s. This represents an improvement of 420% in the computing time, confirming the time economy advantage of using shell elements in finite element analysis.

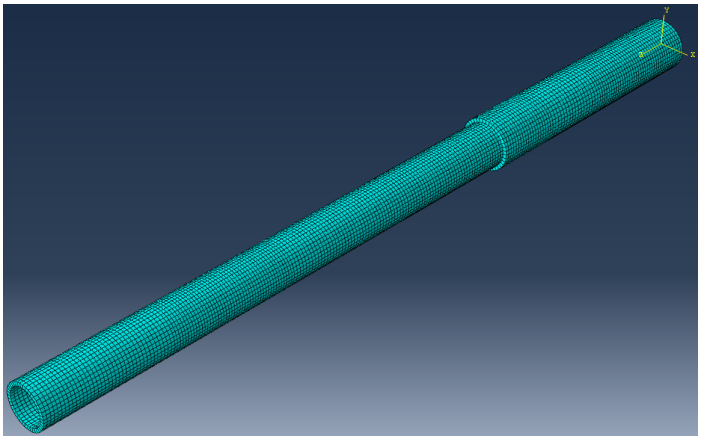

Figure 4.29: First model solid mesh.

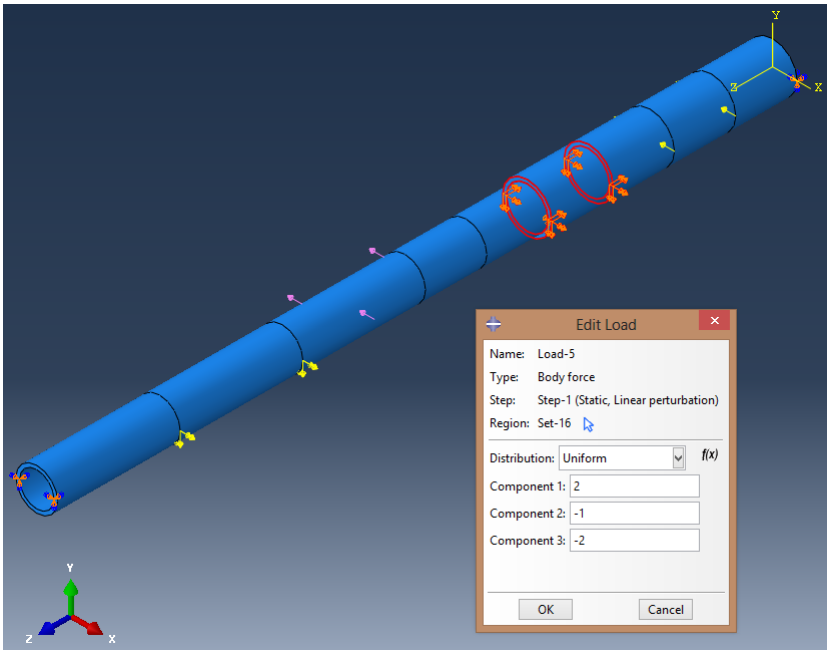

Figure 4.30: Loads and boundary conditions of the solid meshed model.

Second model: simplified tubular structure with three concept components connected

In the second concept model of the cross car beam structure, Figure 4.35, three structural components were added to the first model structure, namely the passanger airbag bracket, the steering column and the center leg bracket that allows the connection to vehicle floor.

Solid elements were used in this model. Mesh was individually generated for each 4 components of the structure. Afterwards, all the components are assembled, Figure 4.36, in order to apply loads and boundary conditions in the global structure.

The loads applied in this second model are exactly the same as those applied in the first, with same direction and the same magnitude. The only difference lies in the point of application since they are two models with different geometries. Concerning the boundary conditions, the central leg base is fixed. The tops of the main beam remain fixed as well .

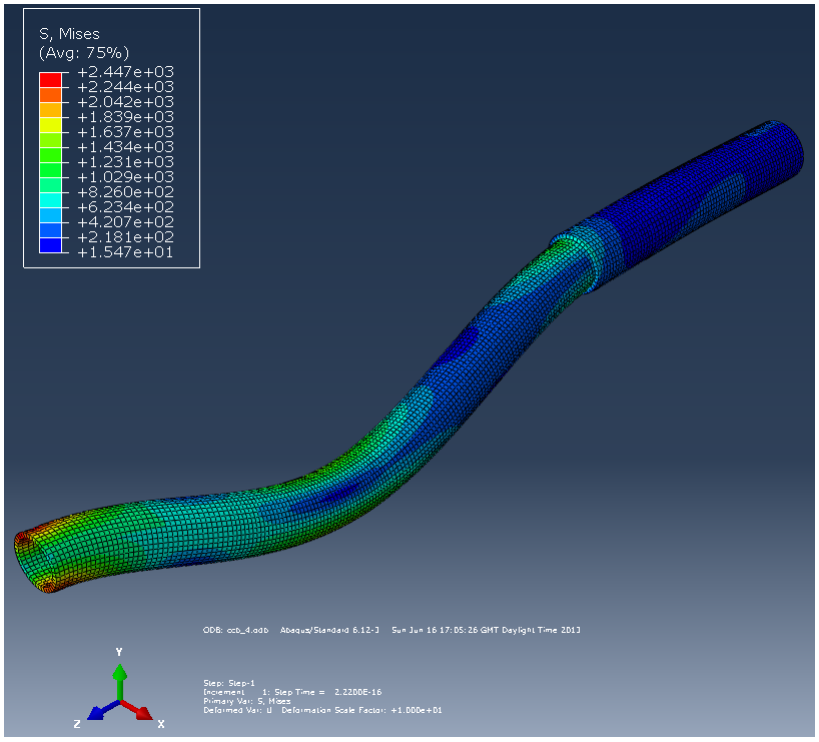

Figure 4.31: von Mises stress distribution (Pa) along the first model solid meshed structure.

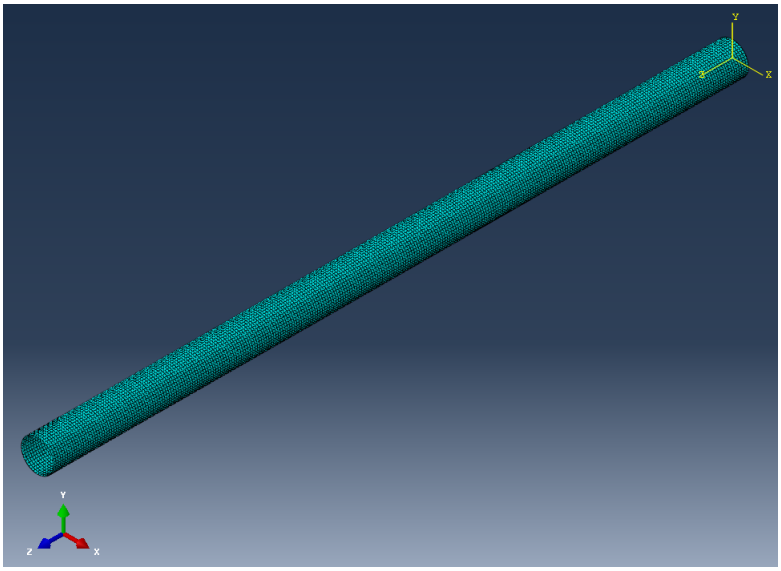

Figure 4.32: First model shell mesh.

Figure 4.37 shows the second model loads and boundary conditions.

von Mises stress distribution results of the second model FEA in Abaqus are illustrated in Figures 4.38, 4.39 and4.40, each one with a different perspective of the structure local deformations. Deformations are depicted with a scale factor of 10^7.

Last but not least, a modal analysis of this second model concept was performed in Abaqus by the finite element method.

One of the cross car beam main attributes is its ability to absorb / reduce the steering

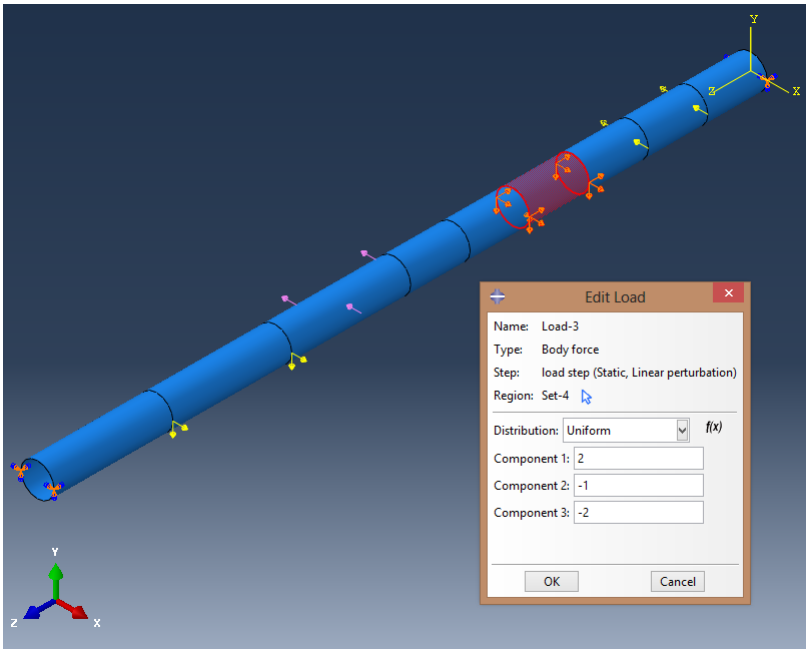

Figure 4.33: Loads and boundary conditions of the shell meshed model.

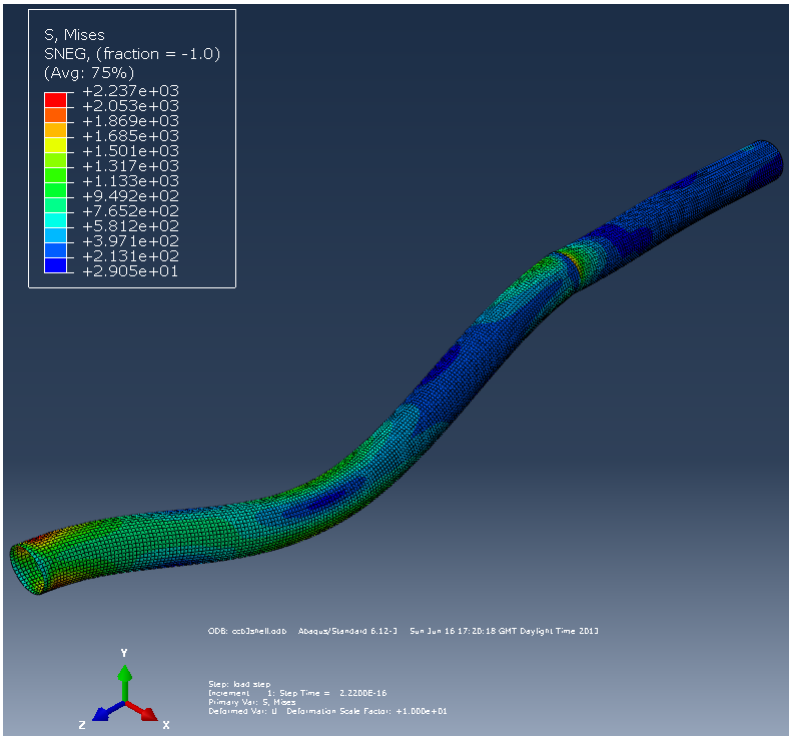

Figure 4.34: von Mises stress distribution (Pa) along the first model shell meshed structure.

column vibration transmission for the driver and passenger. Thus, it is essential to carry out modal analysis during the design / dimensioning of this structure.

The modal analysis was truncated to the first four natural modes of vibration. The natural frequencies computed are as follows: $\omega_1 = 354.32\,Hz$; $\omega_2 = 466.55\,Hz$; $\omega_3 = 472.14\,Hz$; $\omega_4 = 576.32\,Hz$. These values are 10 times higher than the values of real CCB strutures

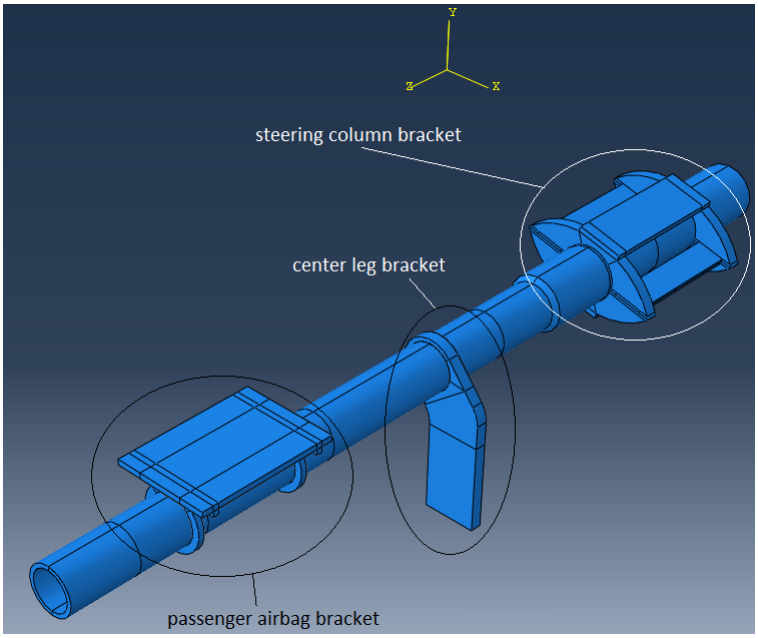

Figure 4.35: Second concept model of the cross car beam.

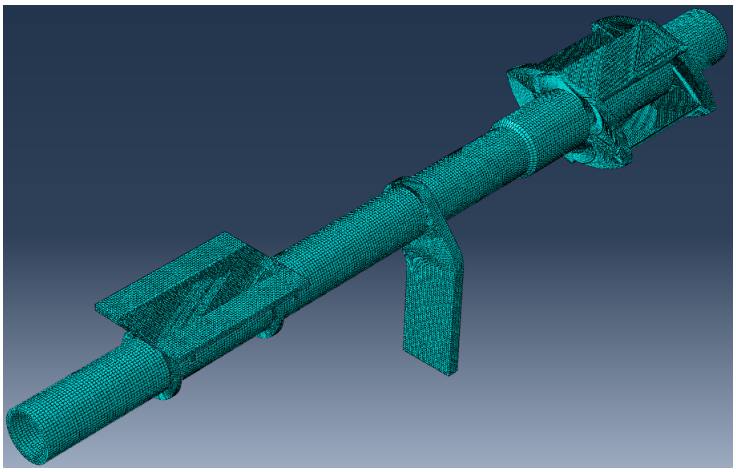

Figure 4.36: Second model solid mesh.

because these models are simply conceptual, very stiff and without realism. The natural shapes are as depicted in Figure 4.41.

4.2 PAM-CRASH

PAM-CRASH is a software package from the ESI Group used for crash simulation and the design of occupant safety systems, primarily in the automotive industry, *e.g.,* Figures 4.42 and 1.12. The software enables automotive engineers to simulate the performance of a proposed vehicle design and evaluate the potential for injury to occupants in multiple crash scenarios.

Based on FEM and specifically designed and validated for crashworthiness analysis in the transportation industry, the software enables the modeling of complex geometry by offering different structural and continuum elements: beams, shells, membranes and solids. In a

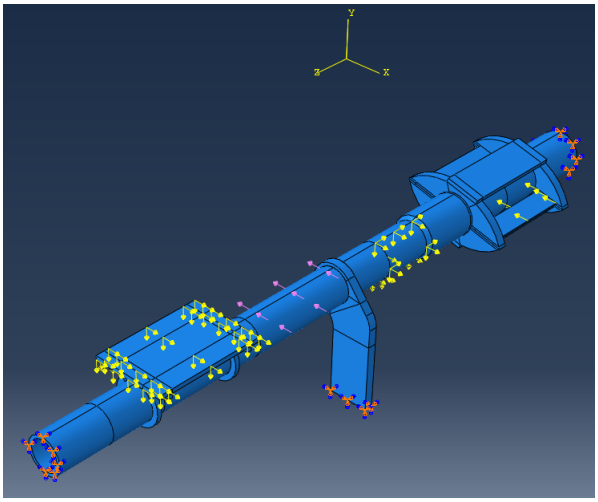

Figure 4.37: Loads and boundary conditions of the second model concept.

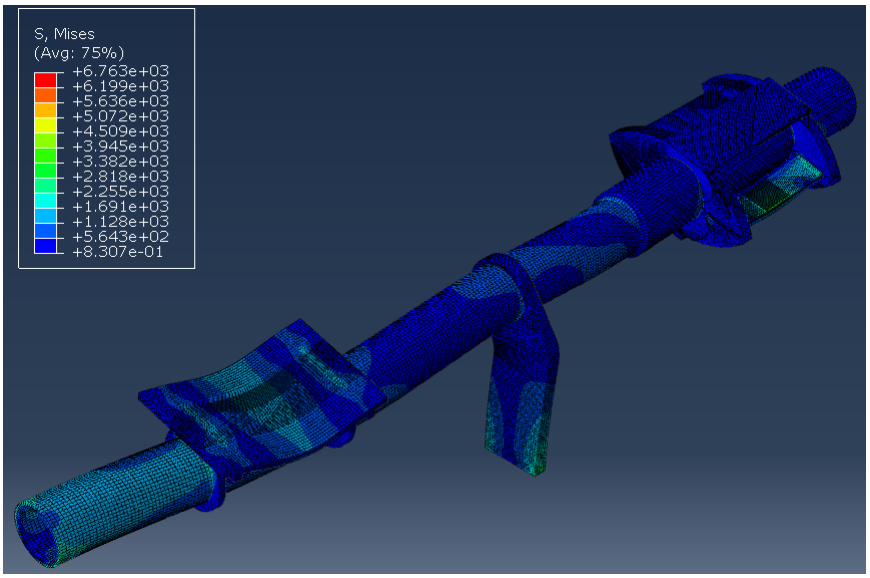

Figure 4.38: von Mises stress distribution (Pa) along the second concept structure - isometric view.

typical crash simulation, shells are used to model thin-walled metal, plastic and composite components. Beams and bars may also be used for stiffening frames, suspensions and special connections. The program offers a large range of linear and nonlinear materials including elastic and visco-elastic and visco-plastic and including foams materials and multi-layers composites up to damage and failure models, [8].

PAM-CRASH code consists of a general purpose explicit and implicit finit element code for impact, crash and static simulation, [75].

4.2.1 Solution phase

The flowchart of the solution phase is shown in Figure 4.43.

Kinematic options are treated after the calculation of accelerations, therefore, [8]:

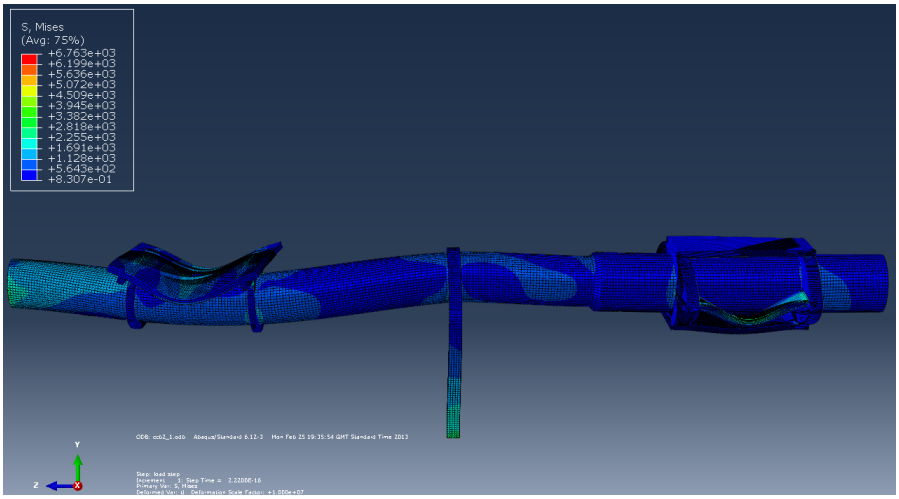

Figure 4.39: von Mises stress distribution (Pa) along the second concept structure - frontal view.

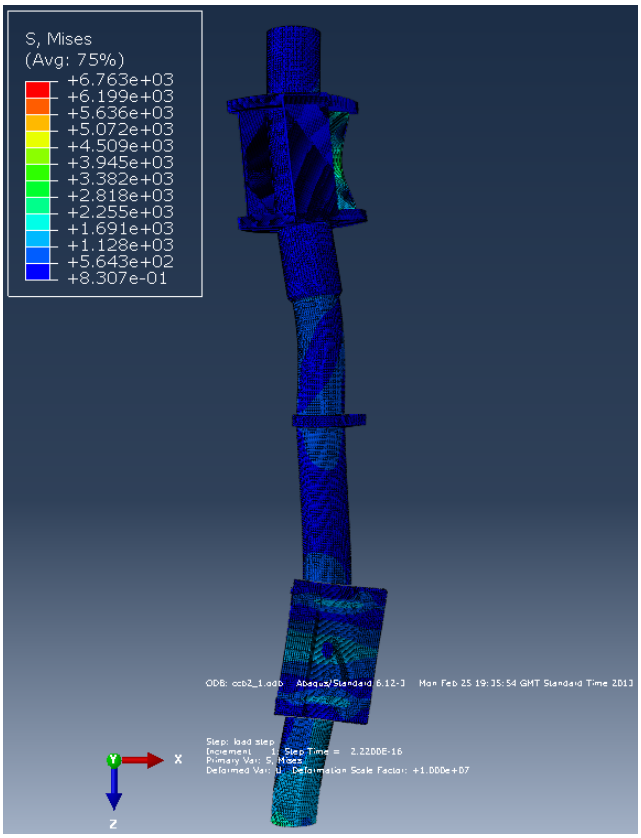

Figure 4.40: von Mises stress distribution (Pa) along the second concept structure -top view.

- For efficiency reasons, accelerations are overwritten for nodes belonging to a kinematic option;
- In general, multiple kinematic options for the same node are not allowed;
- Most interferences (*e.g.*, rigid body node and boundary condition) are automatically

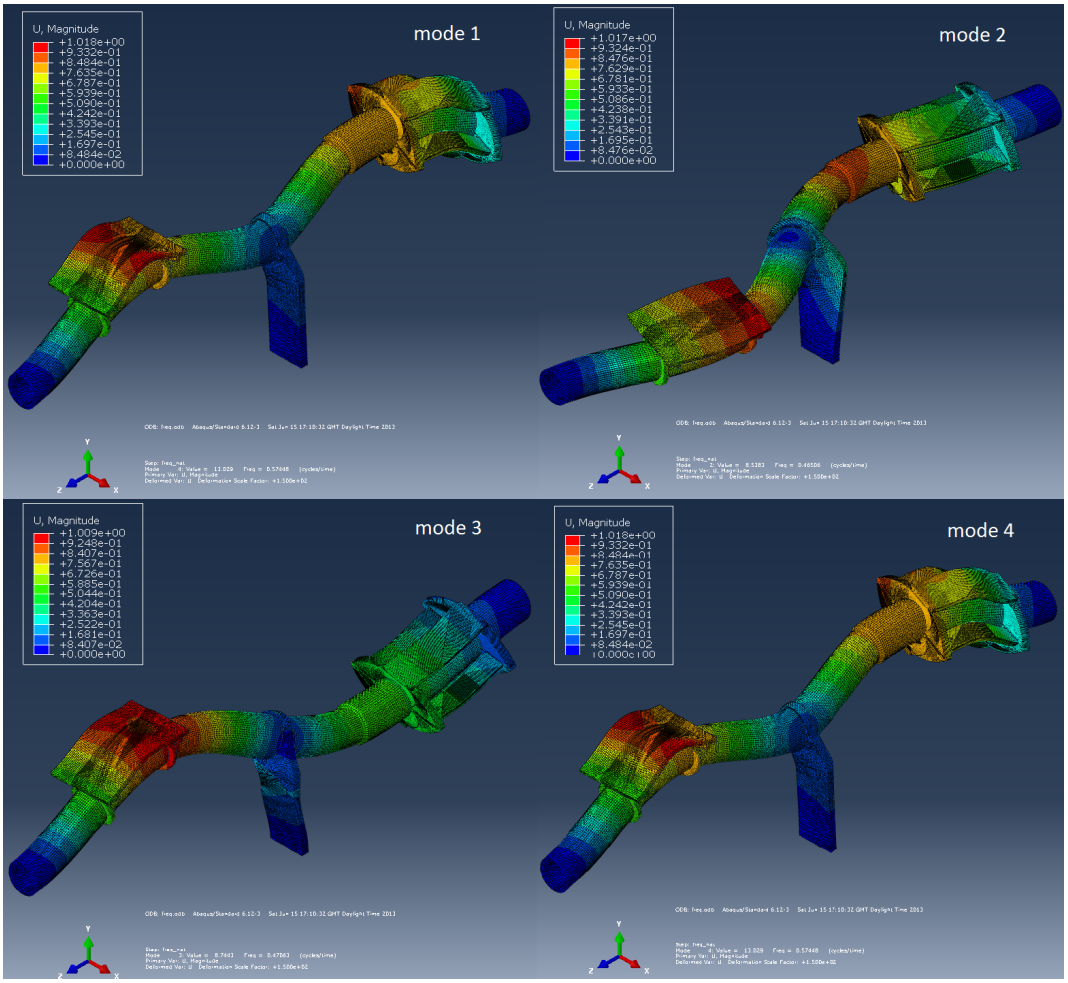

Figure 4.41: Natural shapes of the first four natural modes of the second model concept.

Figure 4.42: PAM-CRASH simulation,[3].

detected during initialization (ERROR message).

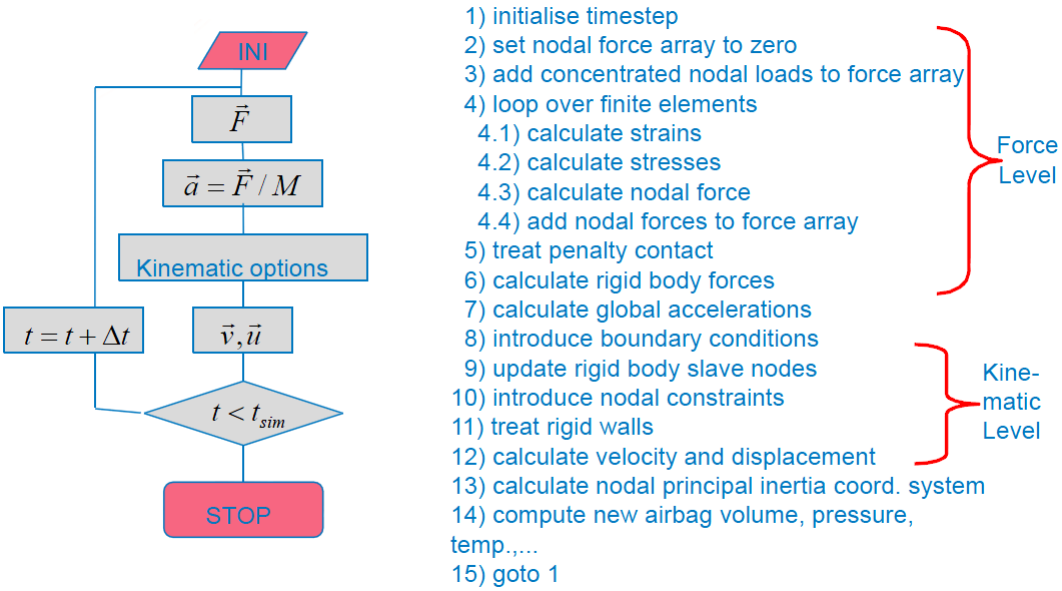

Figure 4.43: PAM-CRASH solution phase, [8].

4.2.2 Crash analysis

PAM-CRASH explicit solver was developed over the years to meet car crash simultion requirements.

Explicit simulations focus on dynamic, non-linear, time- and path-dependent events. Especially at complex contact conditions, it is the recomended solution scheme, [17].

PAM-CRASH explicit solver uses half-step central difference method already discussesed in section 3.1.4.

Analysis Types

Explicit solver performs the following analysis, [17]:

- Transient dynamics;
- Large displacements;
- Non-linear material behavior including damage and failure behavior;
- The equations of motion are integrated explicitly by the method of central differences.

A wide variety of material laws is available to model in elastic, inelastic, damage and failure conditions, [17].

Contact algorithms permit gaps and sliding friction contact along element interfaces, [17].

4.2.3 Modal analysis

PAM-CRASH implicit solver performs modal analysis. However, there are better software packages for this type of analysis as they were specificly developed for NVH problems.

4.2.4 Benchmark cases

As a training exercise and to get deeper understanding of the software tools and functionalities, there are several PAM-CRASH tutorials from Anthony Pickett available online, [75].

4.2.5 PAM-CRASH pre- and post-processing software

Part of the Virtual-Performance software package, PAM-CRASH is a FEM solver code and it only performs the explicit or implicit analysis. Therefore, there are some pre-processing software that allow the user to build a FE model in PAM-CRASH code. Furthermore, a post-processor software capable of reading PAM-CRASH output files to access results from FEA is required. In the following sections the pre- and post-processing software used during the dynamic behaviour analyses performed in this thesis are presented.

ANSA

ANSA was used for handling CAD data and finit element mesh generation.

Visual Crash-PAM

For definition of model entities (loading, boundary conditions, etc.) and material properties, the Visual Crash-PAM software was used.

Visual Viewer

Visual Viewer was used for visualisation of the analyses' results.

Table 4.1: Data and results of the stress intensity factor determination for a finite width center-cracked plate by FEA in Abaqus.

Data:	Remote Stress (Pa):	1	a (mm):	50
	Young's modulus (Pa):	2.10E+11	W (mm):	1000

Analysis nº	nº of elements at the refined zone limit	Total nº of elements	Stress intensity factor (mode I)					Difference % of Abaqus FEA:		
			Infinite plate	Irwin	Feddersen	Abaqus J-Integral	Abaqus KI	Infinite plate	Irwin	Feddersen
1	9	441	12.5331	12.5851	12.6110	7.4486E-10	12.5068	0.2100	0.6219	0.8262
2	12	576	12.5331	12.5851	12.6110	7.5024E-10	12.5519	0.1497	0.2636	0.4687
3	15	729	12.5331	12.5851	12.6110	7.5068E-10	12.5556	0.1791	0.2344	0.4395
4	18	900	12.5331	12.5851	12.6110	7.5362E-10	12.5802	0.3751	0.0392	0.2447
5	21	1089	12.5331	12.5851	12.6110	7.5443E-10	12.5869	0.4290	0.0145	0.1911
6	24	1296	12.5331	12.5851	12.6110	7.5623E-10	12.6019	0.5487	0.1337	0.0721
7	27	1521	12.5331	12.5851	12.6110	7.5698E-10	12.6082	0.5986	0.1834	0.0226
8	30	1764	12.5331	12.5851	12.6110	7.5819E-10	12.6182	0.6790	0.2634	0.0573
9	33	2025	12.5331	12.5851	12.6110	7.5880E-10	12.6233	0.7195	0.3037	0.0975
10	36	2304	12.5331	12.5851	12.6110	7.5966E-10	12.6305	0.7765	0.3605	0.1542
11	39	2601	12.5331	12.5851	12.6110	7.6016E-10	12.6346	0.8097	0.3936	0.1872
12	42	2916	12.5331	12.5851	12.6110	7.6079E-10	12.6399	0.8514	0.4352	0.2287
13	45	3249	12.5331	12.5851	12.6110	7.6120E-10	12.6433	0.8786	0.4622	0.2557
14	60	5184	12.5331	12.5851	12.6110	7.6302E-10	12.6584	0.9991	0.5823	0.3755
15	75	7569	12.5331	12.5851	12.6110	7.6412E-10	12.6675	1.0719	0.6547	0.4478
16	90	10404	12.5331	12.5851	12.6110	7.6489E-10	12.6739	1.1228	0.7054	0.4984

Table 4.2: Study of the plate with hole stress values percent error behaviour with mesh configuration - data and results.

Plate with a central hole stress values percent error behaviour with mesh configuration in Abaqus												
Analysis nº	nº of elements in the 1/8 of the interior hole	Bias	Total nº of elements	Length (mm)		Stress in y-direction (A)			Stress in x-direction (B)			
				ΔX	ΔY	Theoretical solution	Abaqus	Error %	Theoretical solution	Abaqus	Error %
1	10	3.886 to 8.886	1256	3.3584	3.2764	3	2.8657	4.4767	-1	-0.9144	8.5600
2	15	2.61 to 7.61	2056	2.7805	2.6489	3	2.9055	3.1500	-1	-0.9434	5.6600
3	20	1.975 to 6.975	2976	2.3934	2.3081	3	2.9299	2.3367	-1	-0.9589	4.1100
4	25	1.589 to 6.589	3956	2.1699	2.1057	3	2.9440	1.8667	-1	-0.9682	3.1800
5	30	1.3244 to 6.3244	5056	1.9652	1.9305	3	2.9564	1.4533	-1	-0.9762	2.3800
6	35	1.1389 to 6.1389	6206	1.8307	1.8055	3	2.9647	1.1767	-1	-0.9819	1.8100
7	40	0.998 to 5.998	7456	1.7150	1.6942	3	2.9719	0.9367	-1	-0.9870	1.3000
8	45	0.888 to 5.888	8716	1.6329	1.6151	3	2.9772	0.7600	-1	-0.9906	0.9400
9	50	0.800 to 5.800	9956	1.5770	1.5613	3	2.9807	0.6433	-1	-0.9931	0.6900
10	55	0.725 to 5.725	11366	1.5063	1.4926	3	2.9852	0.4933	-1	-0.9963	0.3700
11	60	0.667 to 5.667	12736	1.4578	1.4455	3	2.9884	0.3867	-1	-0.9984	0.1600
12	65	0.615 to 5.615	14166	1.4121	1.4010	3	2.9913	0.2900	-1	-1.0005	0.0500
13	70	0.5725 to 5.5725	15516	1.3828	1.3725	3	2.9932	0.2267	-1	-1.0019	0.1900
14	75	0.535 to 5.535	17056	1.3408	1.3314	3	2.9959	0.1367	-1	-1.0038	0.3800
15	80	0.500 to 5.500	18496	1.3142	1.3053	3	2.9977	0.0767	-1	-1.0050	0.5000
16	85	0.471 to 5.471	20146	1.2763	1.2680	3	3.0001	0.0033	-1	-1.0068	0.6800
17	90	0.445 to 5.445	21676	1.2446	1.2524	3	3.0017	0.0567	-1	-1.0079	0.7900
18	95	0.4217 to 5.4217	23246	1.2296	1.2223	3	3.0032	0.1067	-1	-1.0089	0.8900
19	100	0.4007 to 5.4007	24856	1.2076	1.2008	3	3.0046	0.1533	-1	-1.0099	0.9900
20	105	0.3816 to 5.3816	26506	1.1799	1.1863	3	3.0060	0.2000	-1	-1.0109	1.0900

Case study

The case study consists of the crash simulation and modal analysis of a Ford Fiesta cross car beam BV226, Figure 5.1, by the finite element method using PAM-CRASH as solver, ANSA and Visual-Crash PAM as pre-processor software and Visual-Viewer as post-processor software. This study has a more detailed approach to the dynamic behaviour of the CCB structure when compared to the previous two conceptual simplified design models analyses. Those analyses were far from the automotive industry reality because their main purpose was to develop FEA knowledge. In this chapter, the following example, besides dealing with the CAD geometry of an implemented CCB, the dynamic behaviour analyses, specifically crash simulation and NVH, were carried out with the same CAE techniques and parameters of current automotive industry practice.

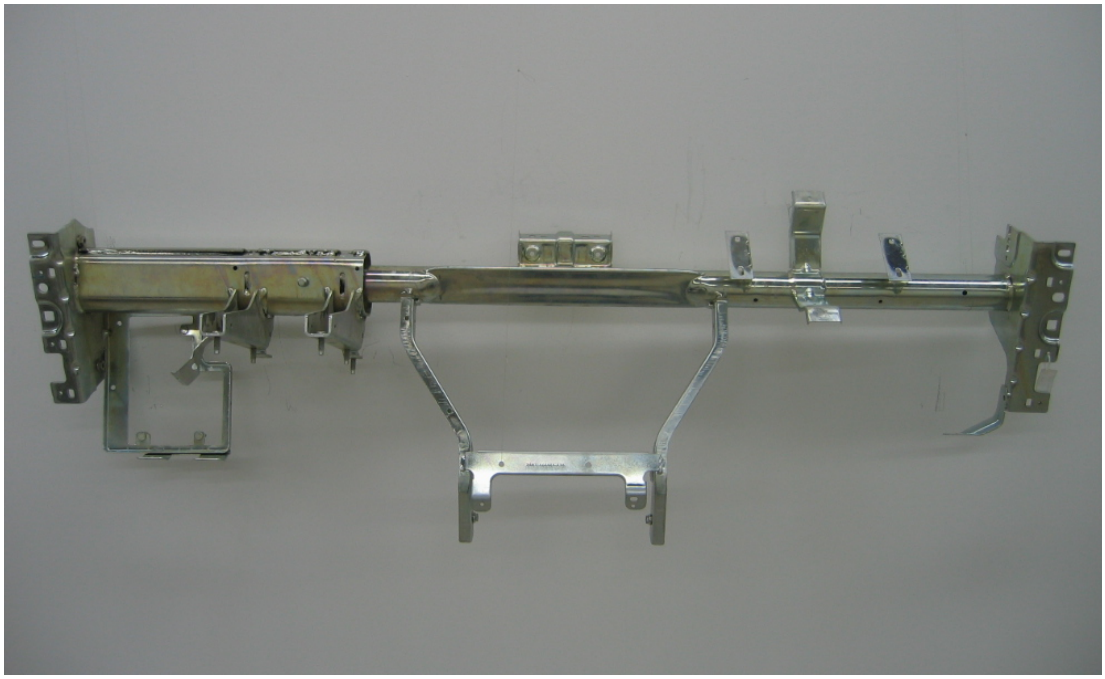

Figure 5.1: BV226 CCB, source: SODECIA.

5.1 Case study description

- Outline: Crash simulation of a cross car beam including mesh definition, model setup and results analysis. Natural frequences and modal shapes location.
- Analysis types: Explicit for crash analysis and implicit for modal analysis.
- Element type: Shell and spring beam elements.

- Material law: Elasto-plastic for crash analysis and elastic for modal analysis.
- Model options: Boundary conditions, rigid bodies, multiple nodes to one node constraint, dynamic loads, g-forces, gravity.
- Key results: Stress distributions, displacements, natural frequencies and modal shapes.

5.2 Background information

Pre-processor, solver and post-processor software used:

- ANSA: For the model mesh generation and other model geometric setups like weld beads, rigid bodys, multiple nodes to one node constraint, springs, etc. .
- Visual-Crash PAM: To set up the finite element model.
- Analysis (PAM-CRASH explicit and implicit): To perform the crash simulation and the modal analysis by the FEM.
- Visual Viewer: Evaluating stress, deformations, natural frequencies and modal shapes results.

5.3 Problem data and description

- Units: kN, mm, kg, ms.
- Description: Steel cross car beam structure with weld connections submitted to dynamic loading that simulate a frontal overlaped crash scenario.
- Loading: Multiple loads on the structure simulating the impact and airbags explosion.
- Material: FEP13 Steel ($E = 205\ kN/mm^2\ (GPa)$; $\nu = 0.3$; and $\rho = 7.8 \times 10^{-6}\ kg/mm^3$), [22]. For plasticity, the stress/plastic strain curve is defined in Table 5.1. The FEP 13 hardening curve is defined in Figure 5.2. The BV226 parts material, available in the technical drawing (appendix 1), is not used in this analysis due to lack of information.

5.3.1 Parts list

The BV226 model structure technical drawing is available in appendix 1. This cross car beam FE model parts list is available in Table 5.2:

Table 5.1: FEP13 steel plastic behaviour, [22].

Stress [GPa]	Plastic Strain [mm/mm]
$161.1932*10^{-3}$ (Yield Stress)	0.0000
$194.3492*10^{-3}$	0.0006
$227.5448*10^{-3}$	0.0010
$255.7650*10^{-3}$	0.0015
$272.9792*10^{-3}$	0.0020
$284.1886*10^{-3}$	0.0025
$326.9750*10^{-3}$	0.0227
$354.9000*10^{-3}$	0.0467
$369.8000*10^{-3}$	0.0701
$383.9000*10^{-3}$	0.0930
$396.0000*10^{-3}$	0.1154
$408.2500*10^{-3}$	0.1373
$408.2500*10^{-3}$	0.3000

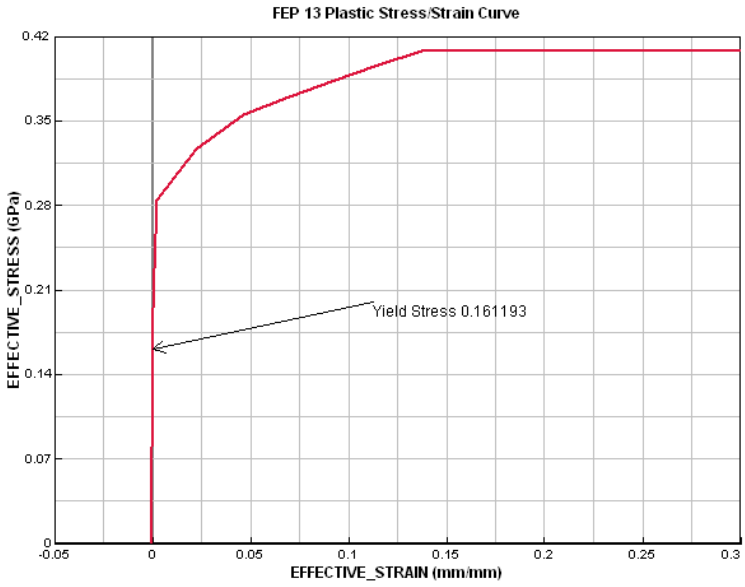

Figure 5.2: FEP 13 hardening curve.

5.4 Model pre-processing

In the following sections, a description of the diferent stages during the development of a crash analysis FE model will be presented. In the last section, the necessary changes needed to convert the PAM-CRASH explicit analysis model into one capable of running in implicit code are described.

Table 5.2: BV226 parts list.

Part name	Part figure	Part name	Part figure
A-PILLAR LHS: A-pillar bracket left hand side (driver's side)	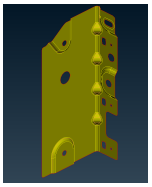	A-PILLAR RHS: A-pillar bracket right hand side (passenger's side)	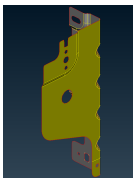
A-PILLAR BRACKET RHS: A-pillar skin bracket right hand side (passenger's side) which connects the CCB to the instrument panel skin	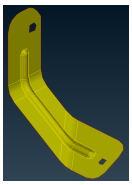	GENERIC BEAM: Main beam with tubular geometry	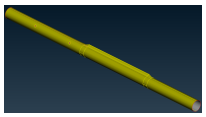
PASSENGER AIRBAG BRACKET ($\times 2$): Bracket connected to the generic beam that supports the passenger airbag box	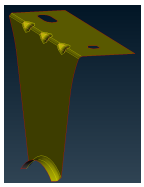	BRACKET INSTRUMENT PANEL: Bracket that connects the generic beam to the instrument panel	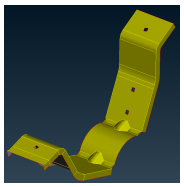
HEATERBOX BRACKET: Bracket that connects the generic beam to the heaterbox of the HVAC system	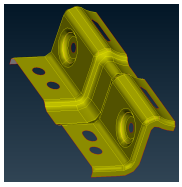	CENTER LEG ($\times 2$): Brackets that support the radio's, have the main role in the connecting the CCB to the vehicle floor and also support the heaterbox	
BRACKET RADIO: Supports the vehicle radio		BRACKET STEERING COLUMN MOUNTING ($\times 2$): Steering column support	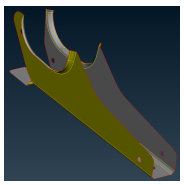
CCB TO IP BRACKET: Bracket that connects the bracket steering column mounting LHS to the instrument panel body		SMBC TUBE: Folded steel sheet welded tube	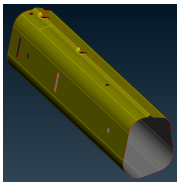
BAFFLE PLATE ($\times 2$): Connects the generic beam to the SMBC tube	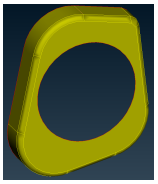	FUSEBOX BRACKET: Supports the fusebox	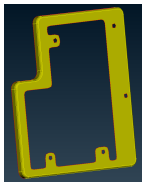
FUSEBOX CONNECTING BRACKET: Connects the fusebox bracket to instrument panel body	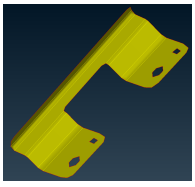	BRACKET FUSEBOX CONNECTING: Connects the fusebox bracket to the SMBC tube	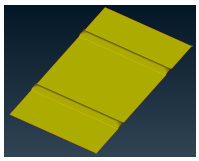

5.4.1 Shell mesh generation in ANSA

First step

After running the software ANSA, the CAD file "2N15_A04545_ AC_A28.igs" which contains the geometry of all components of the cross car beam is loaded. The geometry of the structure will be available on the main screen as it can be seen in Figure 5.3. As a model for the PAM-CRASH solver is being created the default NASTRAN module must change to PAM-CRASH module. To finish this first step, now in the correct module, two mesh files must be loaded, one in the mesh parameters window named 7MM.ansa_mpar and the other in the quality criteria window named fIAT_PARAMETERS.ansa_qual. These files were provided by SODECIA in the framework of the CCB360 QREN resulting project from a partnership between FEUP and SODECIA, as already mentioned in previous chapters.

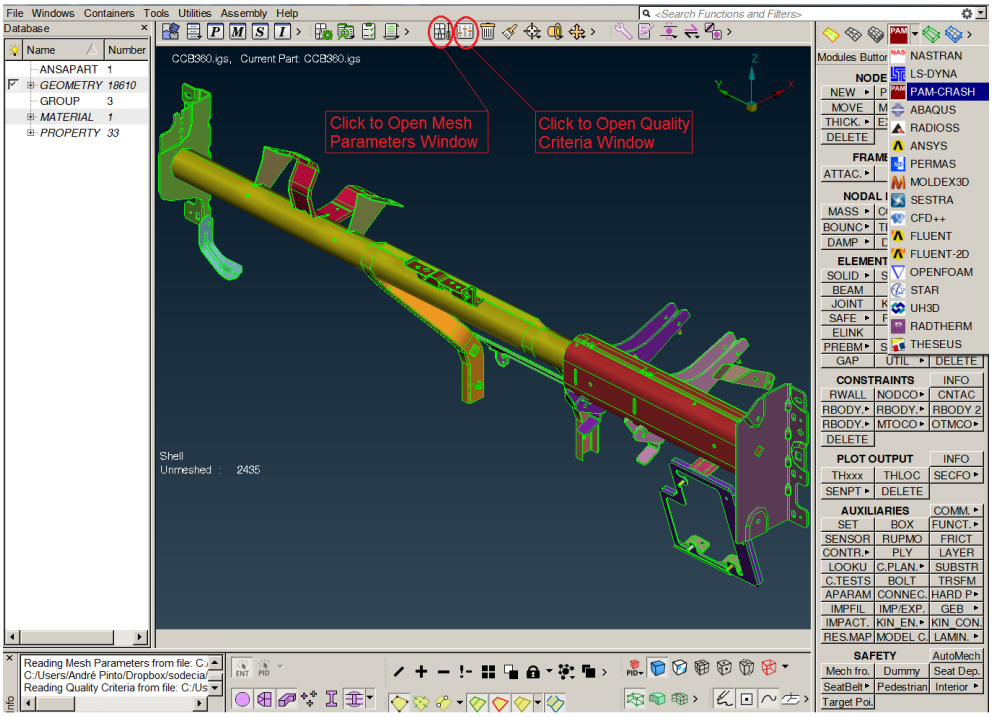

Figure 5.3: First step.

Second step

After loading the mesh parameters file in the mesh parameters window it is convenient to examine the parameters and features defined on the five tabs available. Later, during mesh generation of each component of the structure it may be needed to alter the value of some parameters and enable/disable some features in order to get the best mesh.

The same applies in the quality criteria window where PAM-CRASH calculation should be chosen where available, crash time step should be defined and maximum element length value should be at least two times the minimum length value. Figure 5.4 illustrates all fields of this window as they should be defined.

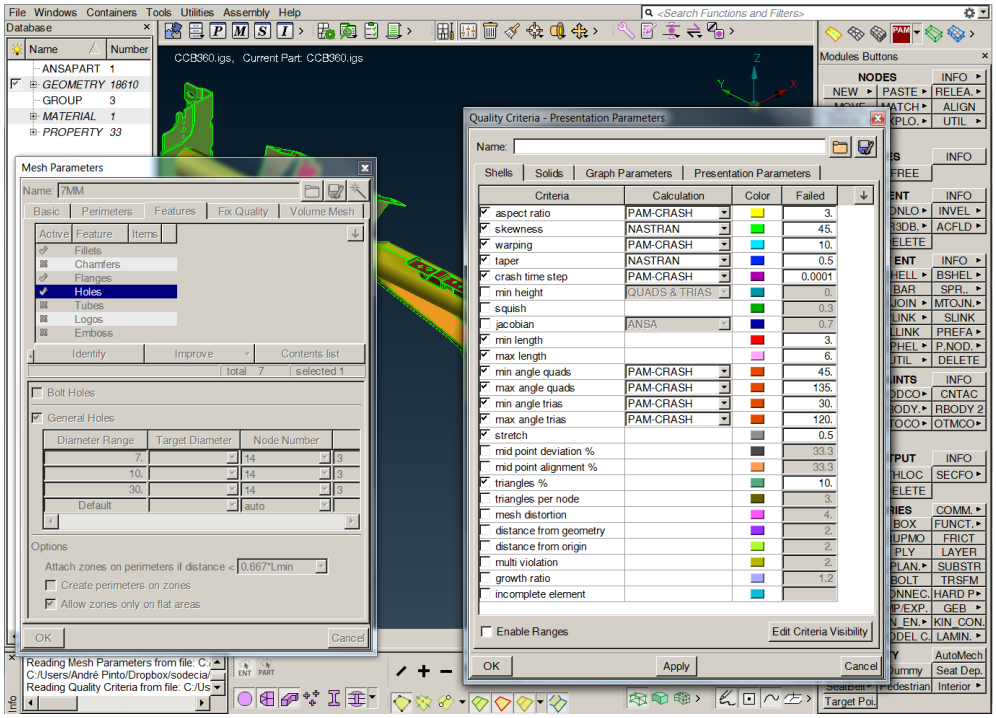

Figure 5.4: Quality criteria window.

Third step

Now that all mesh setup data is loaded and parameters are defined, we must define the material elastic properties so that the time step value can be correctly calculated by ANSA. During the meshing process of each individual part of the CCB structure, time step value will be calculated for each element and if it is below the target value previously defined in the quality window, the element will be highlighted. Thus, it can be identified the zones that need to be re-meshed due to time step problems.

Because we are dealing with crash analysis in PAM-CRASH the properties were defined as shown in Figure 5.5. This is not the final definition of the material properties and behavior. It is there so the user can avoid building a heavy finite element mesh for the CPU.

Fourth Step

In order to achieve a good shell mesh, the best strategy is to generate the mesh independently for each component (part) of the structure and then assemble all parts in one model. Furthermore, there are some non-structural components like nuts and screws that should be deleted. In the Part Manager, Figure 5.6, the model can be devided into several parts, each one related to one component, by clicking *PID-PART* in the Utilities menu and then delete the useless parts.

After deleting the useless parts we can now start working on the shell mesh of each part. The Part Manager is very useful in this stage because it has some important tools like *Identify* which identifies the part number of any component on the global structure or *show only*, on the right clicking menu, so each part can be handle and independently saved by clicking *Save*

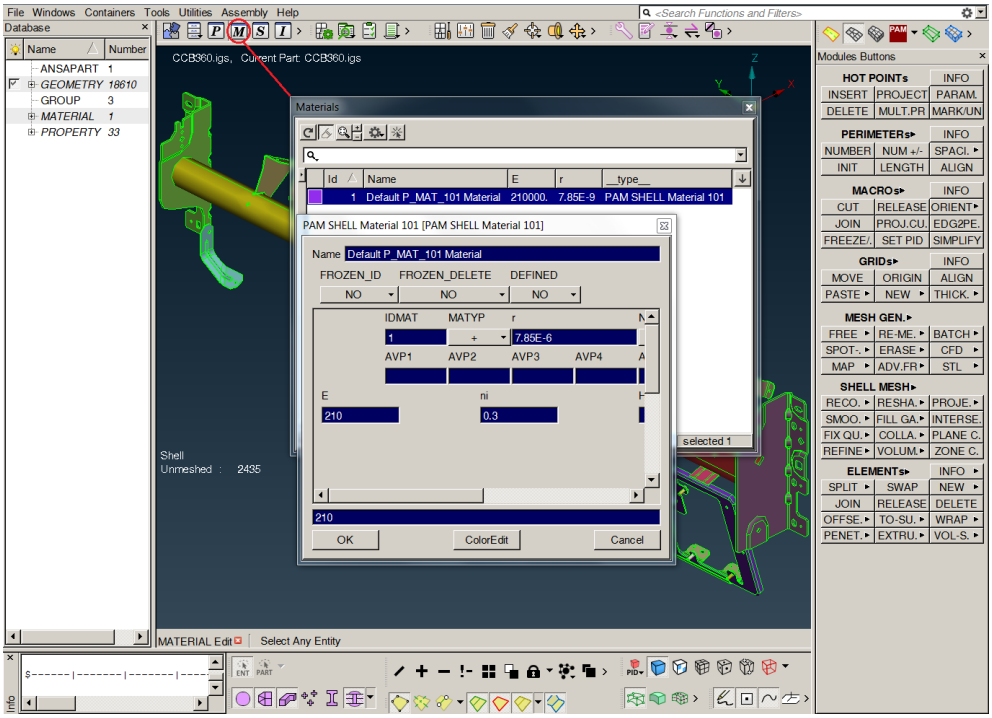

Figure 5.5: Material definition.

visible as on the file menu.

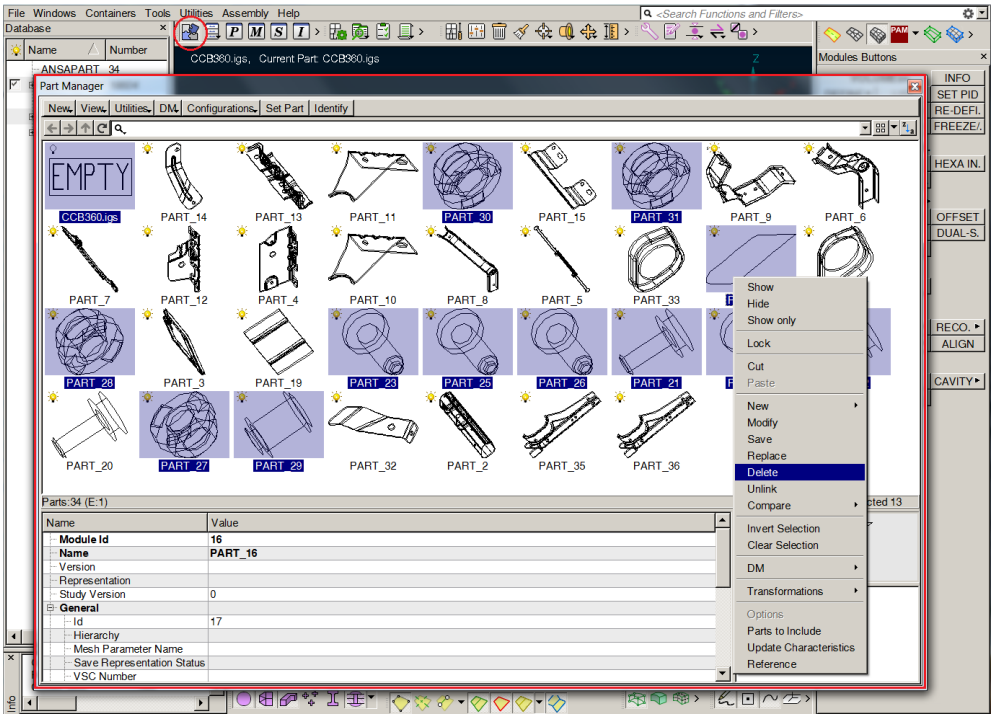

Figure 5.6: Part manager.

Fifth Step

With only one part in the main window, before extracting the middle surface shell from the solid geometry, usually, there are some geometric issues with CAD geometry that need to be solved in the *Topo module*. The first step is to click on ANSA's *Windows* menu and choose the following sequence: S*ettings>Tolerances>Tolerances mode>fine.* Afterwards, in the *TOPO* button, which performs geometry topology, select the all structure and confirm with the scroll button. Then, click ORIENT>Visible to correct the faces normal orientation. After this two steps, a geometry check, Figure 5.7, should be performed to see if there are any remaining problems like cracks, triple Cons (entities curves), needle faces, etc.. In the displayed window it will be visible if there are still geometric problems in red or not. Some errors can be solved automatically by right clicking on them and choose *Fix.* Otherwise, they have to be solved by hand. Geometric errors are identified by red curves in the geometry. Using ANSA Topo module tools, it is possible to correct any type of errors by deleting faces, hotpoints, curves and define new entities. After solving all geometric issues with the geometry check not reporting any errors, we can than proceed to middle surface definition.

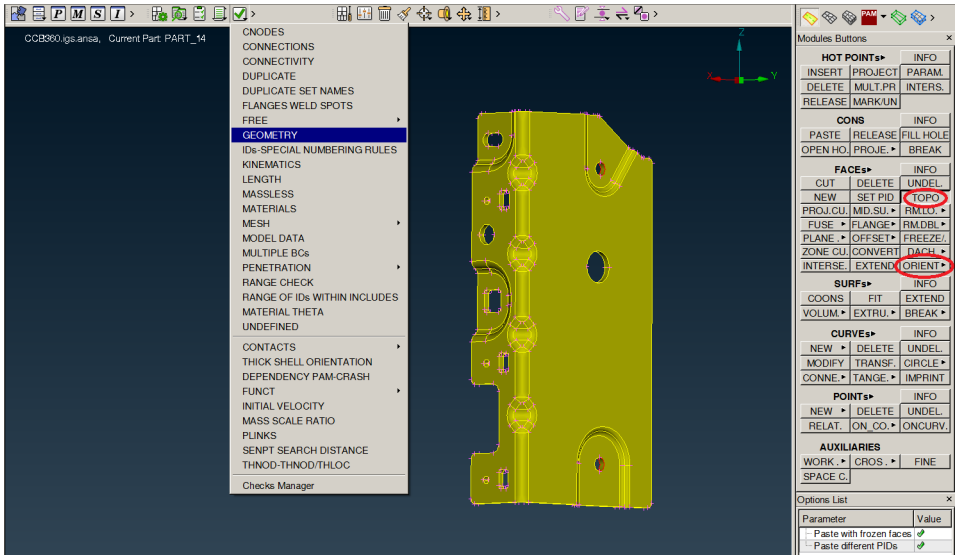

Figure 5.7: Geometry check.

At this point, we have a solid geometry with errors and we must get a shell representative of the solid geometry. To achieve this there are two different approaches. The first one is the quickest and simplest one and consists of using the *MID.SURF* tool which generates automaticly a middle surface of the geometry just by defining de boundaries of the solid geometry and then choosing the external or internal face to be offseted. Normally the best choice is the external surface because it is, usually, the more detailed surface. However, concave geometries, defined with hotpoints, in the surface to be offseted, can generate irregular cross interferences after the offset is done, *e.g.*, Figure 5.8. So awareness of this potential problem must be taken into account when generating mid-surfaces. In these situations, a decision should be made to offset, or not, the internal face. Or, in some rare cases (when the two faces have problematic concave geometries), the geometry should be changed or the offset should

be done by hand shifting from external face to internal face whenever it is more convenient between partitions.

MID.SURF command procedure is as follows: *MID.SURF> Skin> Skin options window where the solid geometry selection is carried out> ok> define the correct boundary lines> ok> surface to be offseted selection> ok> Skin Offset Value window> ok> Middle surface generated.*

One common problem when using the *MID.SURF* command is that sometimes ANSA struggles with the geometry thickness boundaries. So selecting and deselecting some lines (white highlighted ones) during boundaries definition may be needed.

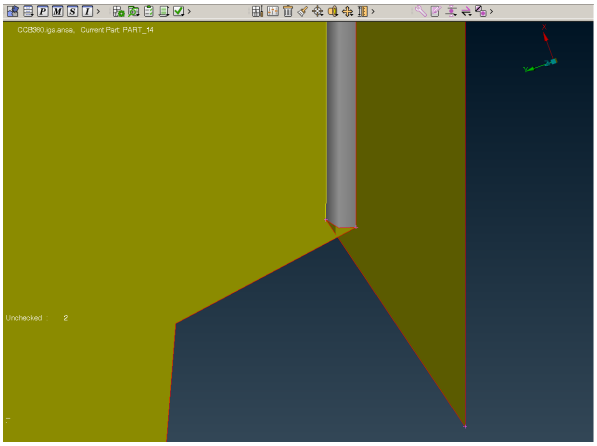

Figure 5.8: Irregular cross interference.

Sixth Step

Now that the middle surface is finished, it is finally possible to start the meshing process after switching to the mesh module. There are some meshing algorithms available in ANSA that give a big help during meshing. Although they produce some quite good meshes, there is always some manual work to do because with this algorithms there is a lot going around during meshing that the user does not control and the final result rarely is very satisfactory for this kind of complex geometries. Therefore, manual meshing is indeed needed, even further with the benefit of the available mesh parameters and mesh quality criteria loaded files. These two mesh settings files give an extra help to the user in order to achieve the best mesh for the purpose of crash simulation in the explicit code of PAM-CRASH.

Concerning manual meshing techniques, every user has its own approach to this iterative process. For the present example, this iterative process is faster and easier because of mesh settings. One important example where the mesh parameter settings are of significant importance is during mesh generation around structural holes, Figure 5.9. These feature allows the user to grow elements around the hole within a diameter range that can simulate the bolted fixed area of the structure. Therefore, the structure's boundary conditions can be precisely defined in the bolted fixed areas. However, if the CAD drawing has not correctly defined the hole, hole feature cannot recognize it and cannot orientate the mesh around it. In this scenarios the best solution is to measure the hole diameter, define the center of the hole, fill the hole and open a new one with the previous center point and diameter mesured. With this

new correctly defined hole, hole feature won't have any problem orientating mesh around the hole during *RECON.* command, as depicted in Figure 5.10.

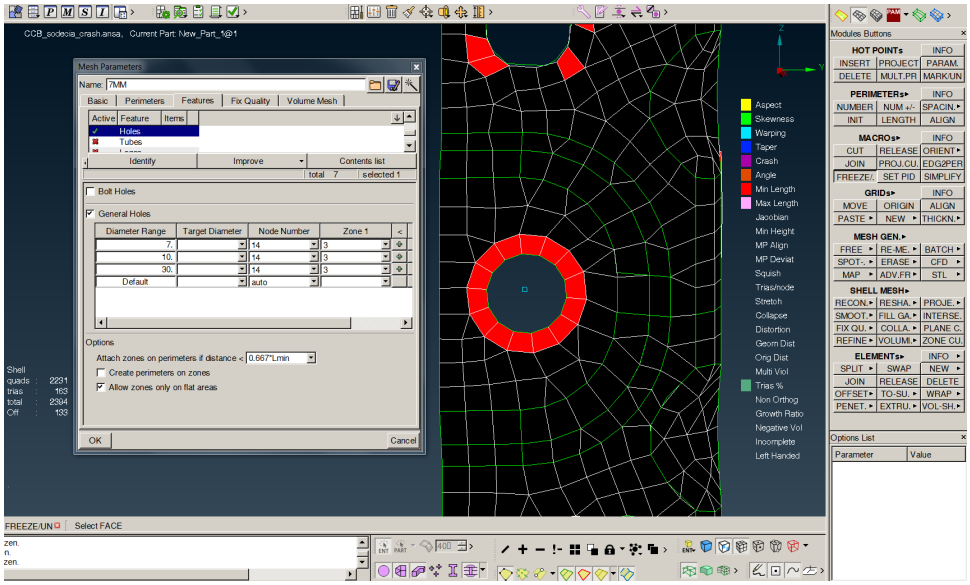

Figure 5.9: Hole feature usefull help in meshing.

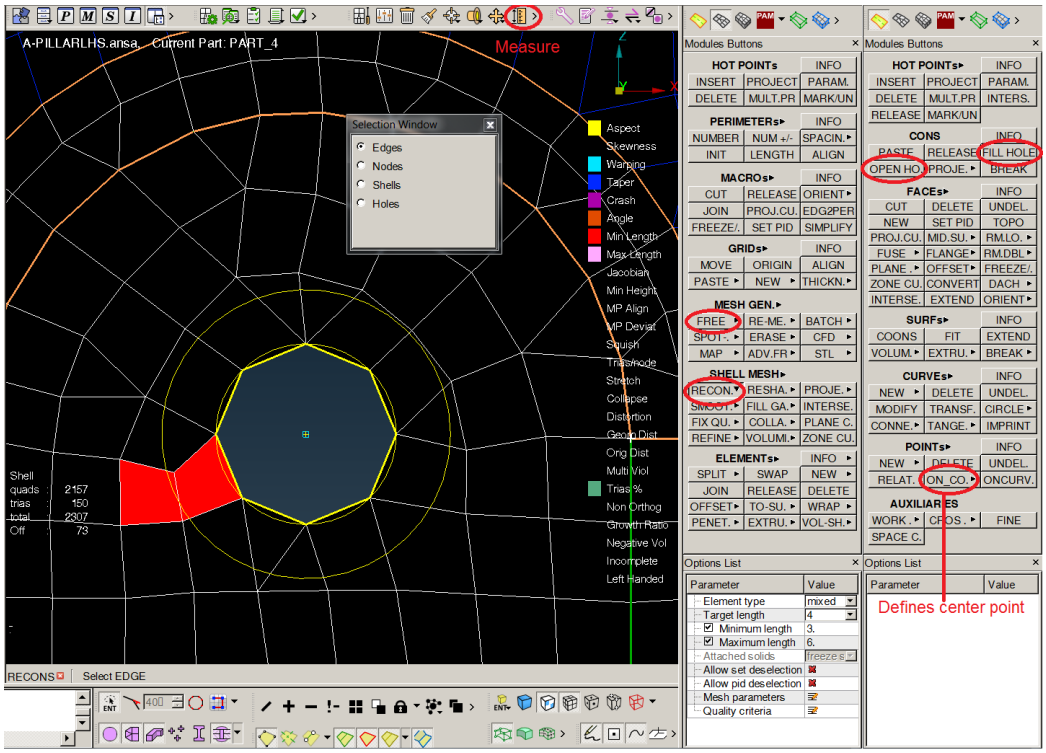

Figure 5.10: Hole correction.

The violet and red highlighted elements, visible in Figures 5.11, 5.10 and 5.9, are elements that have edges with lengthes above the maximum value or below the minimum value, respectively. These elements are very plausible for the FEA if their size do not deviate too much from the neighbor elemements sizes.

Broadly speaking, meshing of the diferent parts of the present cross car beam structure can be achieved by using the following command sequences:

- *MESH GEN.> FREE> SHELL MESH> RECON.> Run Again;*
- *MACROs> JOIN> MESH GEN.> RE-ME.> SHELL MESH> RECON.> Run Again;*
- *MACROs> FREEZE/.> SHELL MESH> RECON.> Run Again;*
- *MACROs> EDG2PER> MESH GEN.> RE-ME.> SHELL MESH> RECON.> Run Again;*
- *SHELL MESH> SMOOT.> Run Again;*
- *ELEMENTS> SPLIT;*
- *ELEMENTS> JOIN;*
- *GRIDS> MOVE;*

where commands,

- *FREE*: Meshing algorithm using the Free meshing method;
- *RE.-ME.*: Re-mesh previously meshed Macro Areas;
- *RECON.*: Reconstruct the mesh on FEM and Macro Areas;
- *FREEZE/.*: Lock (freeze)/unlock (unfreeze) Macro Area's condition;
- *SMOOT.*: Smoothing the mesh on selected Macros's aArea or FEM;
- *EDGE2PER*: Cut macros along along selected element edges or washers.

Figure 5.11 shows three steps of the A-PILLAR LHS cross car beam component meshing process: the initial shell, the first rough mesh obtained with *FREE* meshing algorithm and the final result after manual mesh treatment.

One of the concerns to have in mind during meshing around holes and stress concentration regions is to avoid triangular elements and replace them by quadrilateral elements as they tend to have a lower acccuracy in the results when compared to quadrilateral elements, [76].

Sections (Fith step and Sixth step) should be repeated for each structural part of the cross car beam. After all components are correctly meshed, final assembling can be achieved by creating a new file and in the *File* menu clicking in *Merge*. In the window selection of all parts can be accomplished.

5.4.2 Weld beads generation

Weld beads location and length are defined in the technical drawing, appendix 1. In order to create a weld bead mesh there is a quite stringent procedure to be accomplished. The first step is to extract from the CAD geometry the curves that will guide the bead generation. To extract curves from the CCB geometry, local mesh must be unfrozen. The extraction

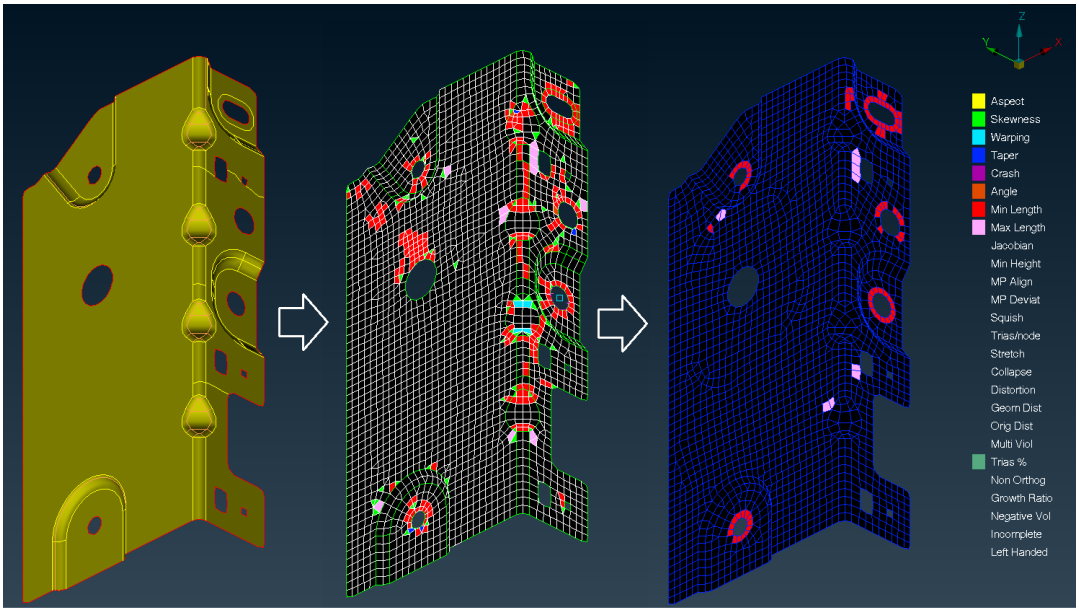

Figure 5.11: A-PILLAR LHS meshing steps.

procedure starts with the insertion of an hotpoint in each tip of the the curve. With measure tool help, it is essential that curves length match the beads length defined in the model technical drawing. To create the new curve, ANSA has a tool called *CONS2C*. (Creates 3-D-curves from *CONS*, element edges and cross sections) in the *CURVESs* menu (Topo module). After all curves are created, they must be converted to *Seam Lines* by clicking in the convert menu of the assembly bar, *Curves* option, select curves, confirm and in the *Connection type* window choose *Seam Line* option. After all *Seam Lines* are finished, the whole group aspect should be like as depicted in Figure 5.12.

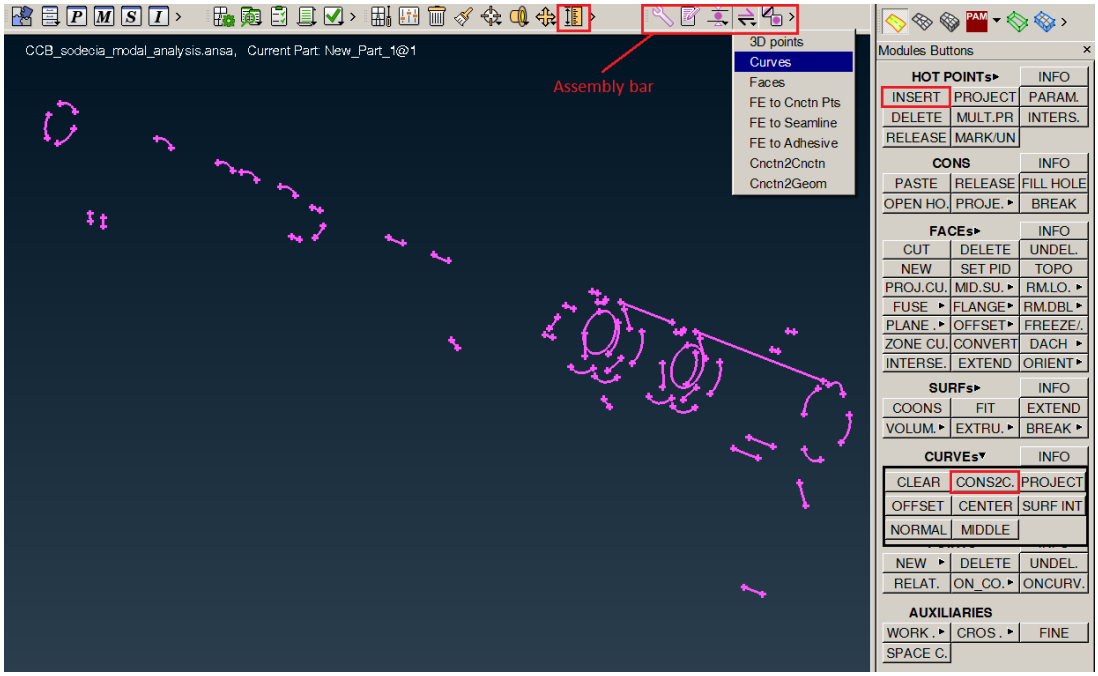

Figure 5.12: Seam Lines of all CCB structure.

With the *Seam Lines* correctly defined, it is finally possible to generate the weld beads mesh in the *Connection Manager* window. All weald beads were created with a with of 3.5 mm. Parts to be welded must be defined in the *Connection Manager*. *OVERLAP-SHELL* is the most suitable FE representation type but in some complex scenarios *LASER-WELD-SHELL* might be suitable as well. Figure 5.13shows the *Connection Manager* weld bead parameters defined for one of the multiple weld beads of the CCB structure.

During this process, it is very likely that, after the weld bead mesh is generated, remeshing of the welded parts is needed. Another subject to be noted is the bead material definition. It is a common pratice to define weaker steel properties for the welded beads mesh, because weld connections always cause regions of weakness in the structure, precisely the heat affected zone around the beads. In the present model, the same material (FEP13) was defined for all components, including weld beads. This step is reapeted for all weld connections of the structure.

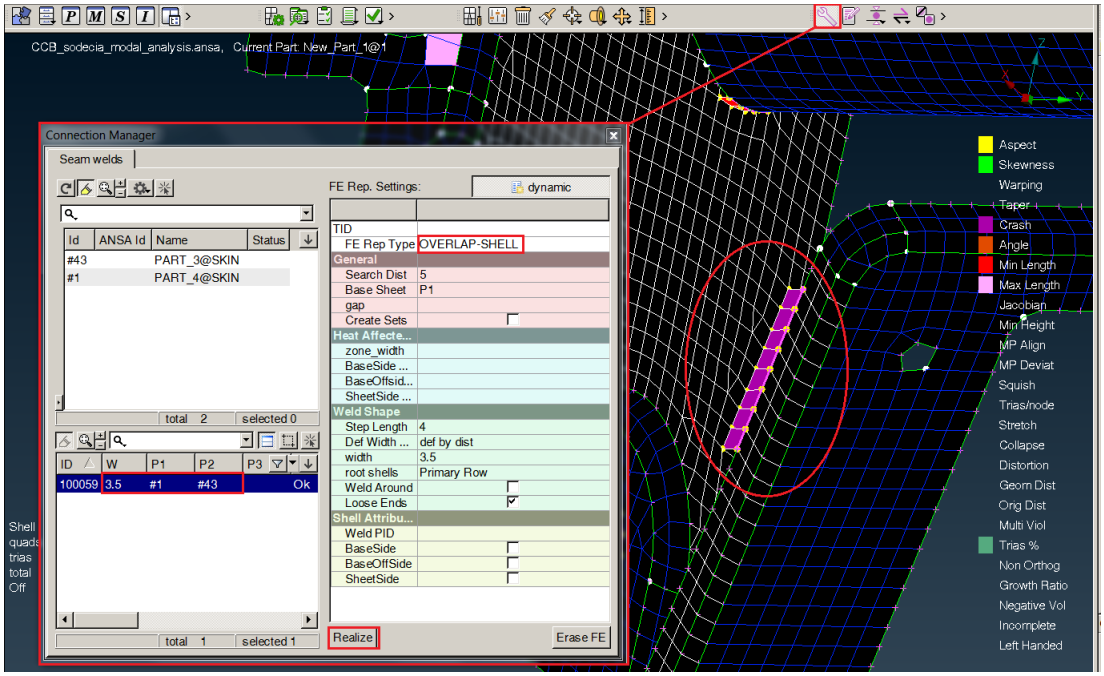

Figure 5.13: Weld bead mesh definition.

After this step, although the model definition could continue in ANSA, the model mesh was ouptutted from ANSA to Visual-Crash PAM.

5.4.3 Constraints definition

In order to study the CCB dynamic behaviour there are some attached components to the CCB that play an important role and must not be ignored. Unfortunetly, they are not part of the CCB model mesh because there was no CAD geometry file with this global assembly available.

These components have a significant mass with their COG offset from the CCB section center line. So, they alter the structure inertia properties by adding to it mass-moments

of inertia. Furthermore, during a crash event, the attached components suffer themselves external dynamic loading. With this two details in mind, there are some constraint to be defined in the CCB structure. These are three rigid bodys and three multiple to one node constraint which refer to:

- Two rigid body with user-defined center of gravity, mass and inertia properties (PAM-CRASH definition: rigid body type 3). These rigid bodys refer to the passenger airbag assembly and to the heaterbox of the car HVAC system;
- One regular rigid body (PAM-CRASH definition: rigid body type 0) to localize the point of apllication of the A-pillar LHS load and moment;
- Two multiple to one node constraint with user-imposed mass and inertia properties (PAM-CRASH definition: *MTOCO* type 1). One refers to the steering wheel - airbag assembly and the other one refers to the steering column.
- One regular multiple to one node constraint (PAM-CRASH definition: *MTOCO* type 0) to localize the first cardan of the steering column where is placed a frontal impact dynamic load.

The reason why *MTOCOs* are used instead of rigid bodies is because they are applied in the steering column assembly where the the dependent nodes of the steering wheel and 1st cardan *MTOCOs* are exactly the same node which is also the independent node of the the steering column *MTOCOs*. This scenario is incompatible with rigid body constraint as mentioned in previous section 3.4.

To build these 6 constraints, coordinates of the COGs and of the loads point of application needed to be defined. Figures 5.14, 5.15 and 5.16 define some of these points coordinates, more precisely the COG of the steering column, steering wheel and heaterbox, respectively. Passenger airbag COG and first cardan coordinates were obtained from a NASTRAN model of this CCB in SODECIA - Centro Tecnológico. These coordinates are visible Table 5.3. Last but not least, the coordinates of the point of application of the A-pillar loading were assumed to be as defined in Table 5.3.

Table 5.3: Passenger's airbag assembly COG, first cardan coordinates and A-pillar LHS loading point of application.

Coordinates(mm)	Passenger's airbag COG	1st cardan	A-pillar LHS loading
X	2344.78	2218.29	2254
Y	343.20	-334.95	-660
Z	1108.79	848.12	979

Figure 5.17 shows the points of the CCB structure where the heaterbox is fixed.

Mass and inertia properties of the heaterbox, passenger airbag assembly, steering column and steering wheel were provided by SODECIA - Centro Tecnológico. These properties are defined in Table 5.4.

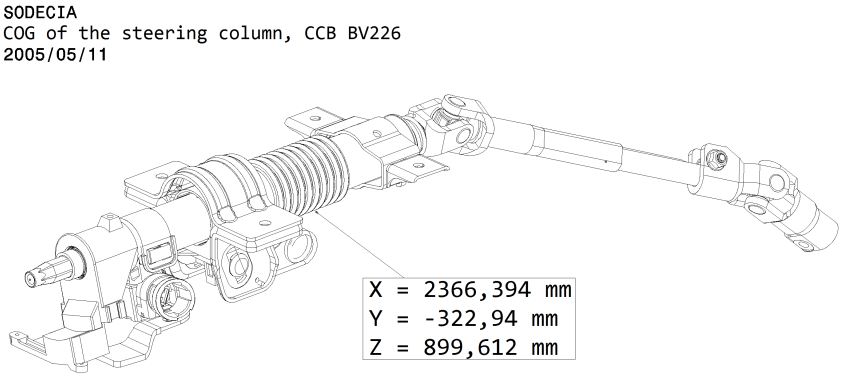

Figure 5.14: Steering column COG.

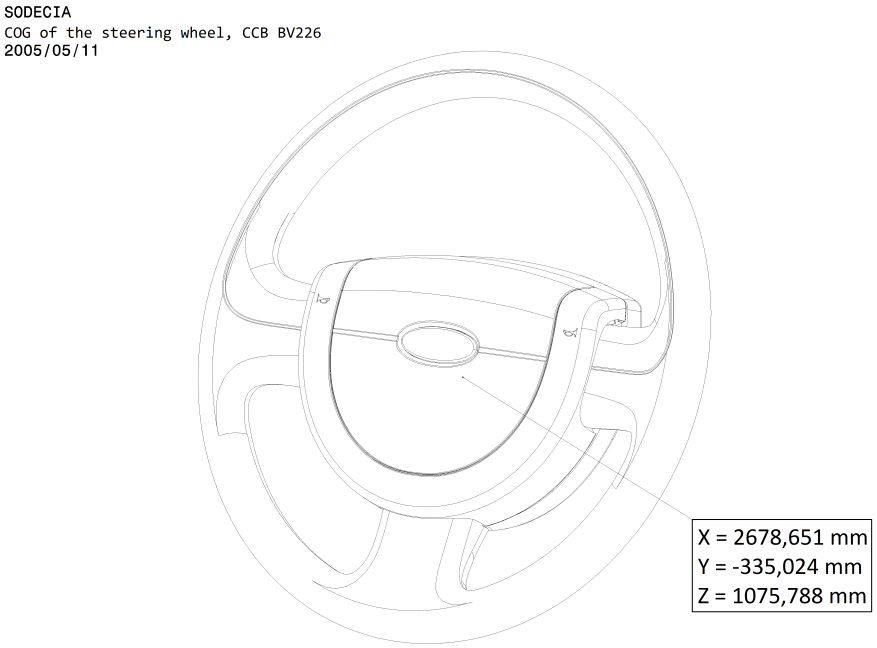

Figure 5.15: Steering wheel-airbag assembly COG.

In Visual-Crash PAM, rigid bodies and multiple to one node constraint options are available in the *Constraints* sub-menu of the *Crash* menu. Their configuration is illustrated in Figures 5.18 and 5.19. In both editing windows, mass, inertia properties, COG node and the dependent nodes (bolted area elements nodes) are defined. For *MTOCOs* the independent node can be different from the COG node. In this constraint, DOF of the dependent nodes constrained to the corresponding DOF of the independent node can be also defined. The final aspect of the model constraints is visible in Figure 5.20.

5.4.4 Loads and boundary conditions definition

Loads were adapted and slightly changed in some vectores magnitude from Renault technical specification, [77].

In Visual-Crash PAM loads and boundary conditions can be created in *Loads* submenu of

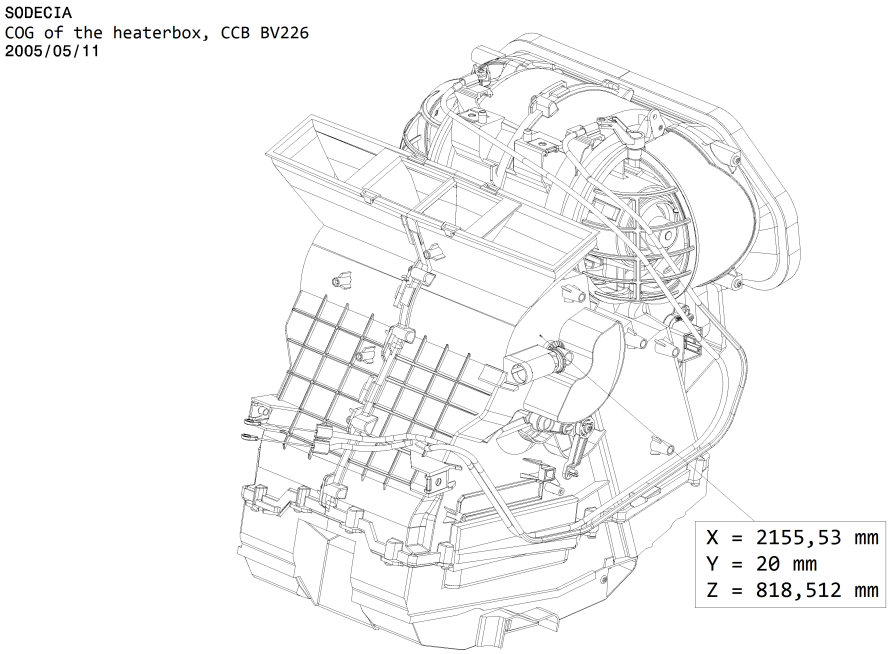

Figure 5.16: Heaterbox COG.

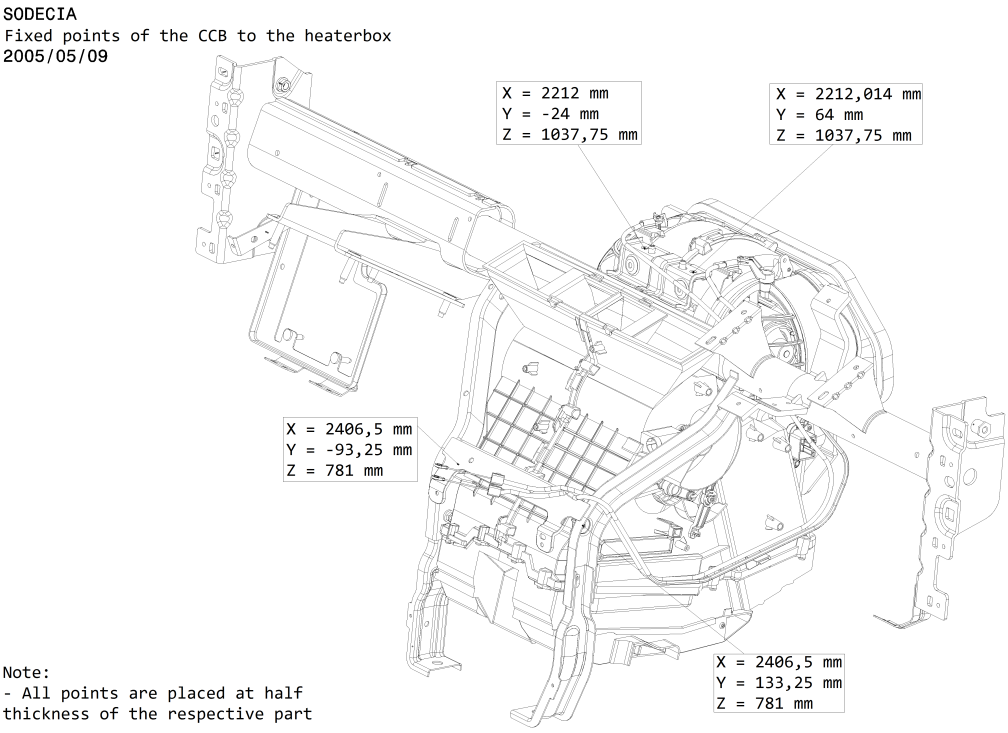

Figure 5.17: Fixing points of the heaterbox to the CCB.

the *Crash* menu.

Boundary conditions location is available in the following Figure 5.21 and were defined as fixed for crash simulation. Fixed elements are the ones that define the bolted area, Figure 5.22.

For the crash simulation, boundary conditions were removed from the A-pillar LHS bracket

Table 5.4: Mass and inertia properties of all the relevant attached components to CCB structure considered in the present analysis.

Full inertia tensor (global frame)				
Component	Mass (kg)	Inertia tensor $\left(kg \cdot mm^2\right)$		
Steering column	3.8	10137	2140.6	-14478.4
		2140.6	34663.2	1358.1
		-14478.4	1358.1	26541.9
Steering wheel	2.45	3042.2	4.75	433.4
		4.75	1993.19	2.04
		433.4	2.04	2298.3
Heaterbox	4.5	128884	-882.9	31894
		-882.9	158880	1722.3
		31894	1722.3	110847
Passenger's airbag assembly	3	40586.6	-109.2	337.7
		-109.2	19439.8	-325.6
		337.7	-325.6	43355.7

due to the loads applied to this component, as this simulation recreates a overlap frontal colision where the A-pillar from the barrier side suffer large deformations and large rotations.

In order to dimension the left hand drive CCB to an overlaped frontal crash, dynamic loads are applied to this structure simulating a colision that occurs is 100 *ms*. These loads were defined as follows:

- A-Pillar loading: moment and a tensile stress applied to the point defined in Table 5.3. This point is connected to the A-pillar bracket by a rigid body. This moment and tensile stress are defined in time dependency in Table 5.5. Figures 5.23 and 5.24 illustrate the load and moment magnitude in time.

- Steering wheel loading: tensile stress applied to the steering wheel COG with two components, one in x-direction and one in z-direction. These components simulate the driver's airbag explosion and are defined in time dependency in Table 5.6 and illustrated in Figure 5.25.

- First cardan loading: tensile stress applied to the first cardan *MTOCO* independent point, Table 5.3, with components in the three directions, x, y and z. These components are defined in time dependancy in Table 5.7.

- HVAC loading: tensile stress applied by the heaterbox into the generic beam during a colision. This stress is distributed on all nodes of the Figure 5.26 highlighted elements.

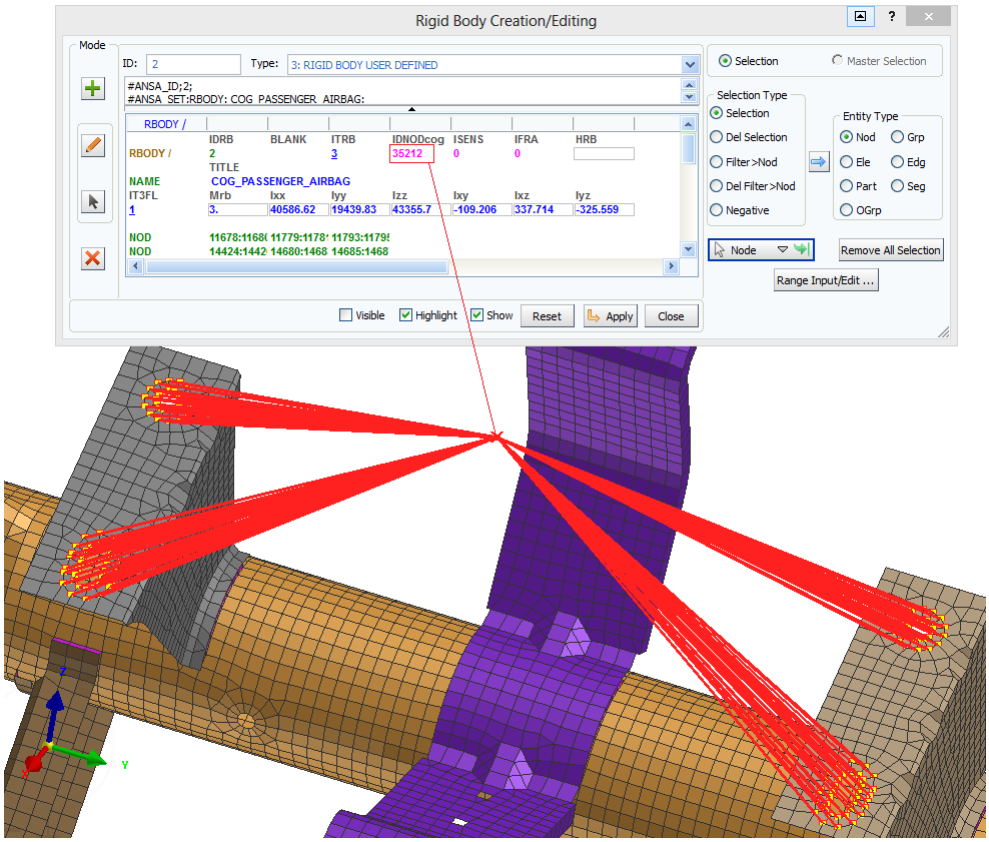

Figure 5.18: Passenger's airbag rigid body.

Table 5.5: A-pillar loading.

A-Pillar LHS loading			
Time (ms)	Moment ($kN.mm$)	Time (ms)	Y-direction stress (kN)
0	0	0	0
25	-250	30	-3
32	-87.5	38	-0.3
60	-750	52	-18
72	-575	68	-18
90	-87.5	100	0
100	0		

Stress magnitude in time dependancy is defined in Table 5.8 and illustrated in Figure 5.27.

- SMBC tube loading: tensile stress applied in x-direction to the SMBC tube during the front colision. This stress is distributed on all nodes of the Figure 5.28 highlighted elements. Stress magnitude in time dependancy is defined in Table 5.9 and illustrated in Figure 5.29.

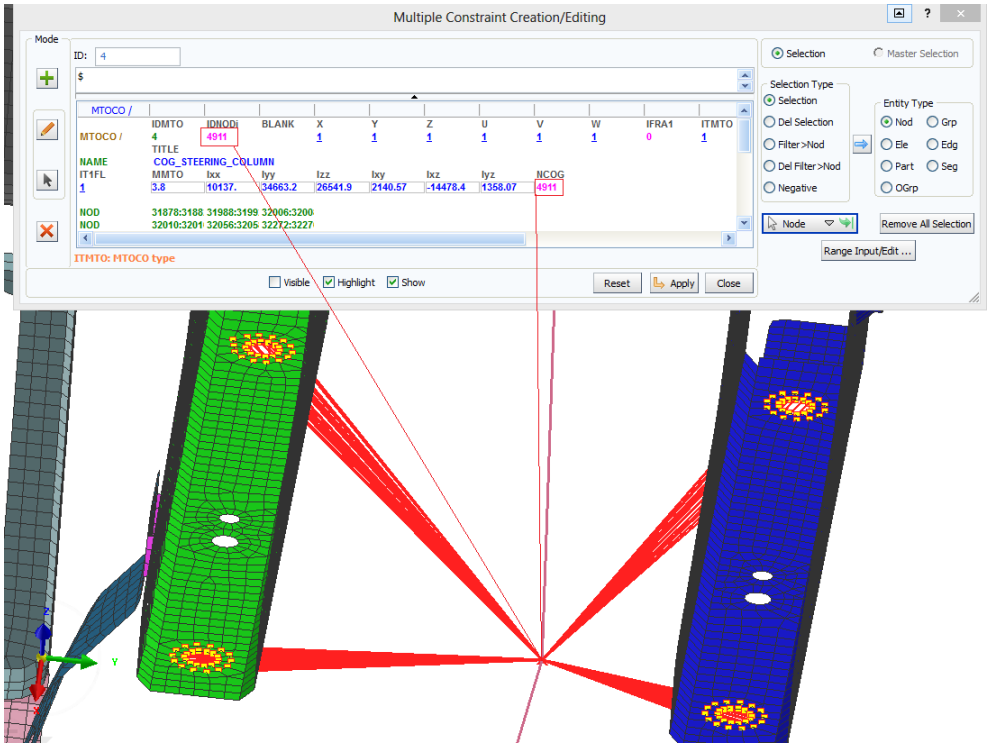

Figure 5.19: Steering column *MTOCO*.

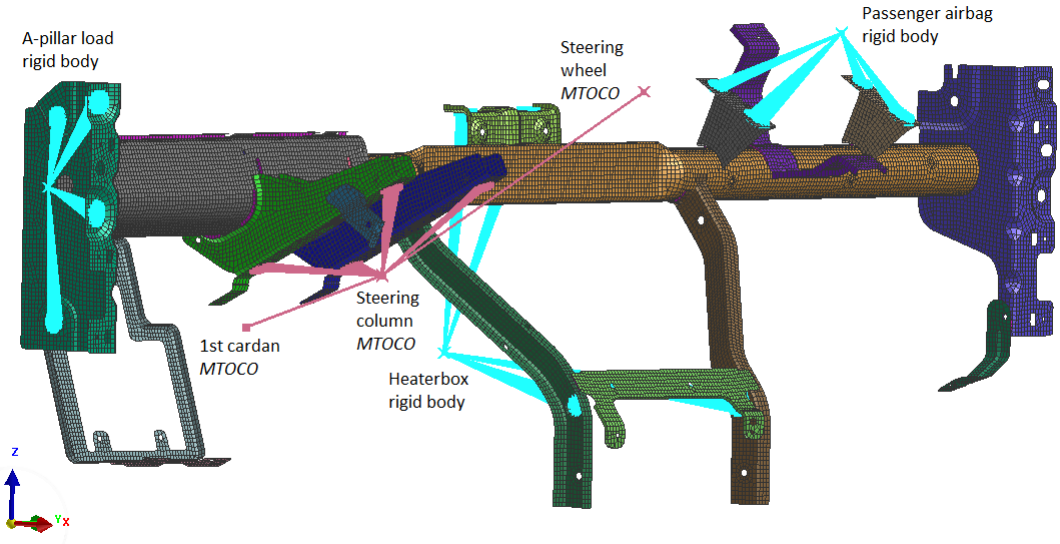

Figure 5.20: CCB constraints.

- Passenger's airbag loading: tensile stress applied to the passenger's airbag assembly COG, Figure 5.3, with two components, one in x-direction and one in z-direction. These components simulate the passenger's airbag explosion and are defined in time dependency in Table 5.10 and illustrated in Figure 5.30.

- CCB acceleration fields: gravity and deceleration g-force apllied in all CCB model nodes and defined in Table 5.11.

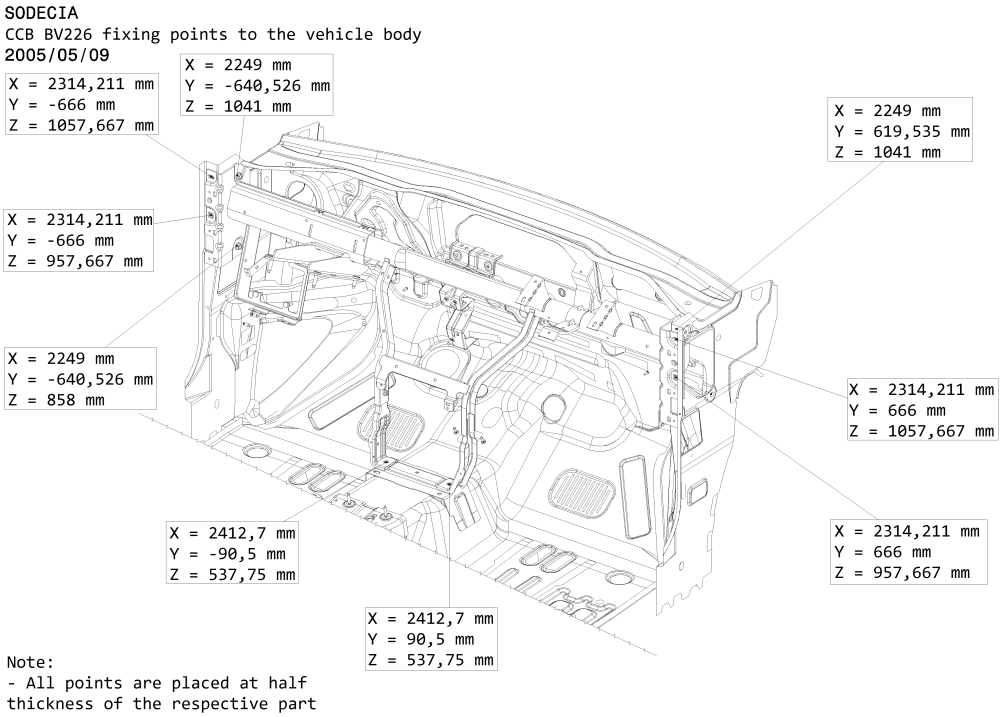

Figure 5.21: CCB boundary conditions location.

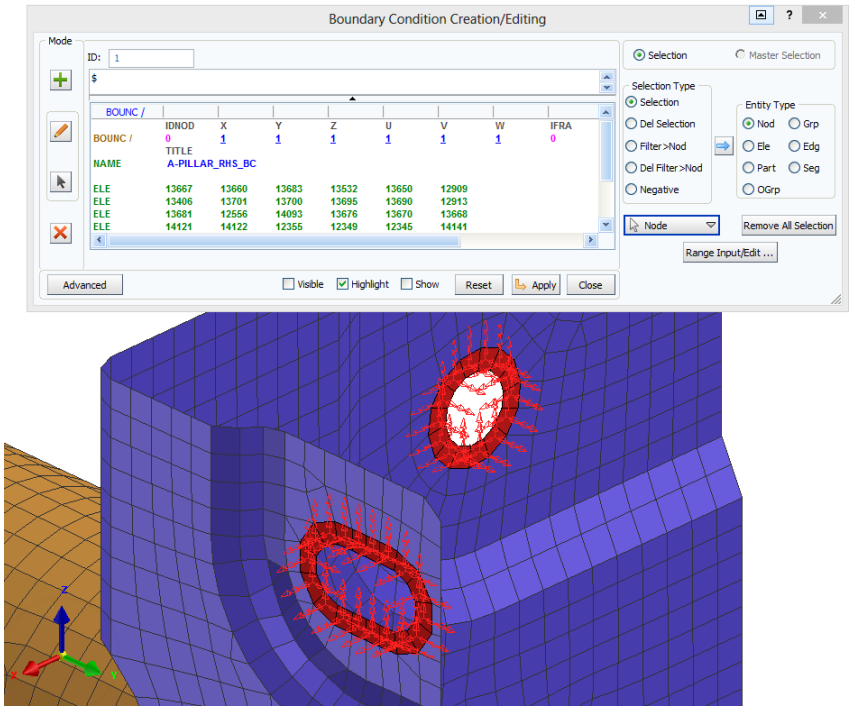

Figure 5.22: Fixed elements of the bolted area.

5.4.5 Material law definition

In PAM-CRASH, for every different element formulation, the material law and properties need to be defined for each and every one. So, as an example, if a FE model has solid and shell elements or has different types of shells, it is not possible to define the material and

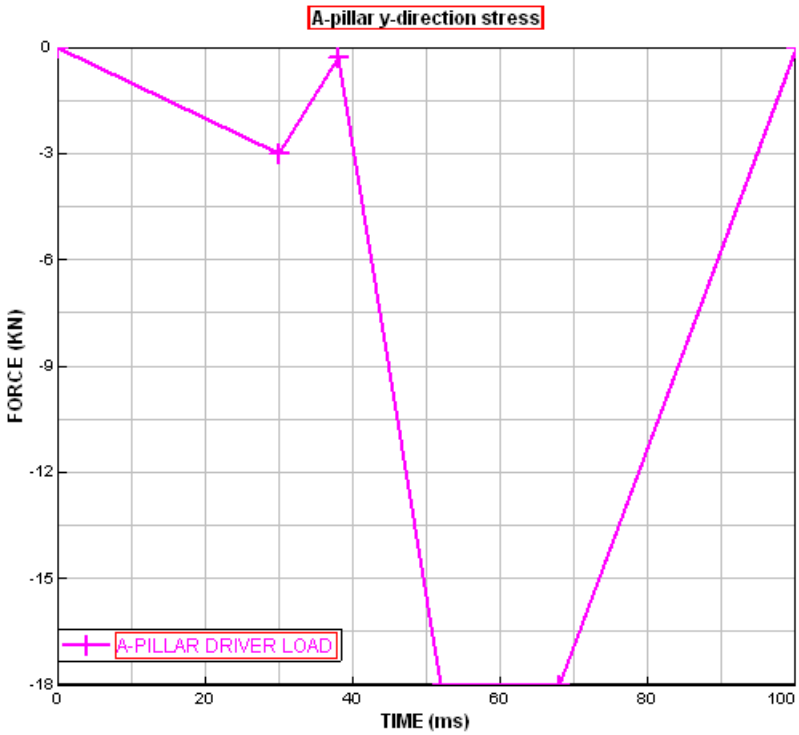

Figure 5.23: A-pillar y-direction load.

Table 5.6: Steering wheel loading.

Steering wheel loading		
Time (*ms*)	X-direction stress (*kN*)	Z-direction stress (*kN*)
0	0	0
16	0	0
18	-7	-2
22	-7	-2
24	0	0
28	0	0
30	-5	-1
80	-5	-1
85	0	0
100	0	0

then associate it to both element formulation. This is the most significative negative point of PAM-CRASH.

For the present model, only one element formulation was used, the structural shell element *103-ELASTIC_PLASTIC_ITERATIVE_HILL*. This element and its linked material properties were defined in the *Material Editor* window, as depicted in Figure 5.31. The default Belytschko-Tsay formulation (one point integrated) is the most economical and should be used

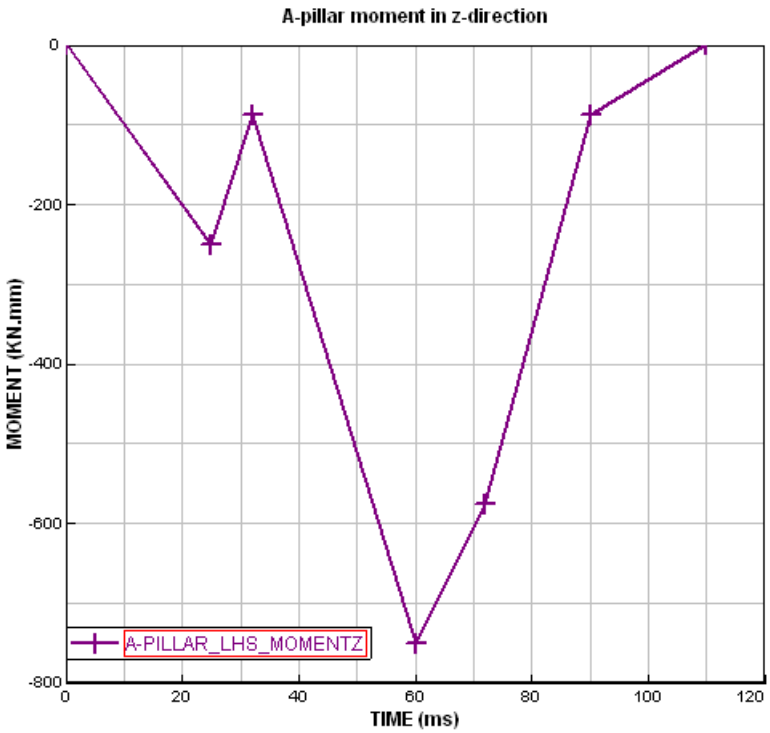

Figure 5.24: A-pillar moment.

unless features particular to other formulations are required. Hourglass control parameters and transverse shear correction factor were set with the default values. If not defined, these settings appear as an error wise in the *Data Check* tool available de *Checks* menu. Also in *Data Check* error wise, for convergence reasons, a stiffness proportional damping ratio value of 0.1 was suggested. Plastic stress/strain curve was defined with the values of Table 5.1. The maximum plastic strain for element elimination was set as 0.3 in accordance to Table 5.1 data. Finally, the shell elements hourglass prevention and parameters and the quadratic viscosity multiplier value were set according to Pickett's crash models tutorials, [75].

5.4.6 Control cards

After finishing the FEA model, there are some control cards in the explorer tree, Figure 5.32, that need to be defined before exporting the model to PAM-CRASH solver job format (.pc). *Inputversion* control card is mandatory and must always be defined for both explicit and implicit analyses. *Analysis* control is also mandatory in order to define the PAM-CRASH solver. Signal enables or disables iteractions with the running job by a signal file wether it exists or not in working directory. There a great number of interactions allowed like ploting results up the instant of processing the signal file, quiting, stoping, etc. *Runend* control card defines the run termination time (150 ms in the present example). *OCTRL* controls the output files formats and their parameters. *TCTRL* cards, Figure 5.33, allows the user to control computing time-step in order to achieve computing stability and convergence in the results. *DTmin* avoids drops of the time step during simulation, *DTSCAL* improves the initial time

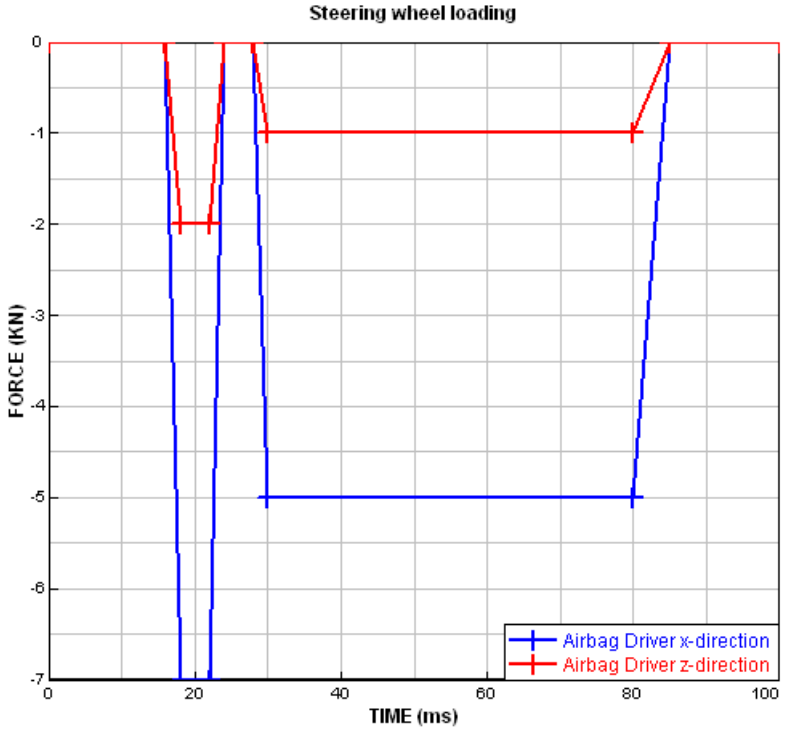

Figure 5.25: Steering wheel loading.

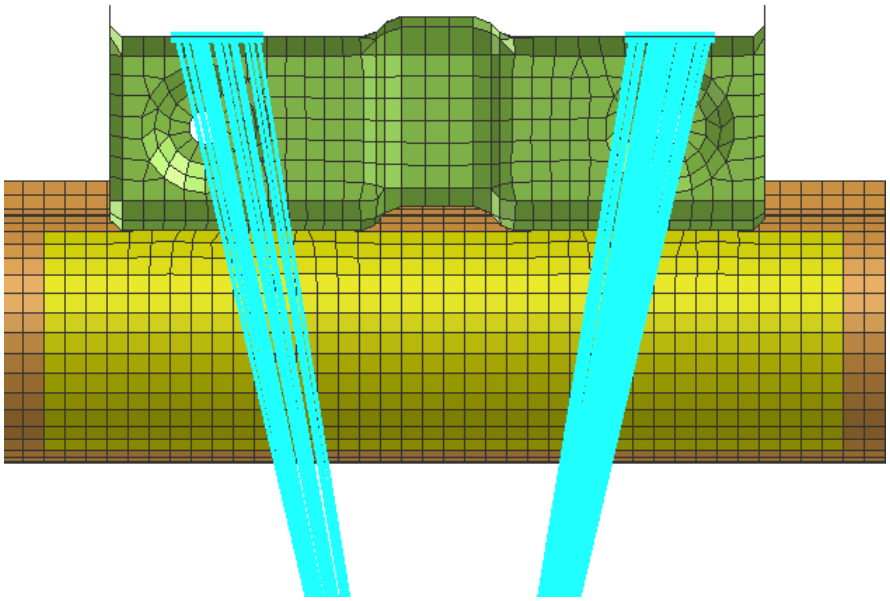

Figure 5.26: HVAC loading point of application.

step of the initial mesh and *ALMASS* defines the maximum allowed mass increase factor per node. The time step calculation was already mentioned in previous section 3.1.4. *ECTRL* was used to define the strain rate filter intervals. Also before exporting it is advisable to perform some checking tools available in the *Checks* menu to avoid errors that enable the simulation, [17].

Figure 5.34 shows the final model aspect with the applied load vectors, constraints and

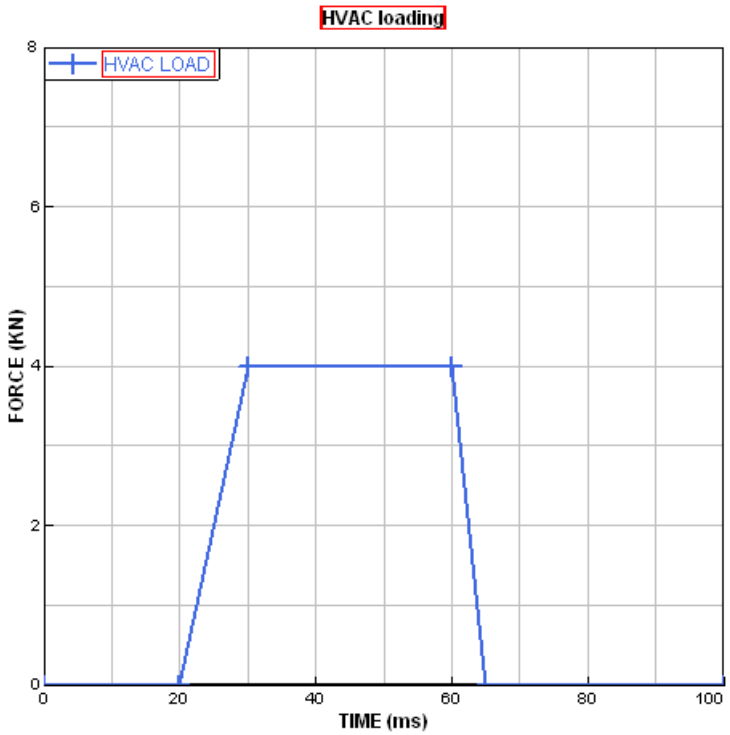

Figure 5.27: HVAC loading.

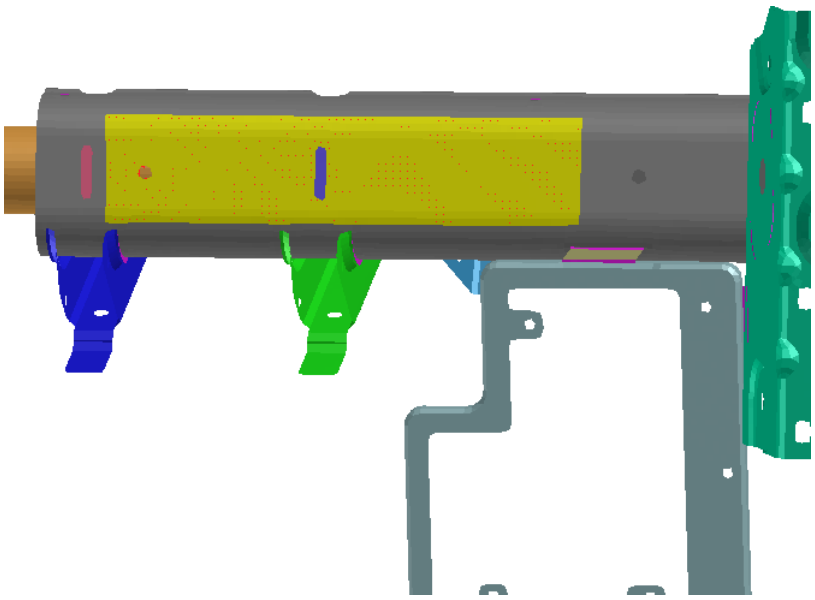

Figure 5.28: SMBC loading point of application.

boundary conditions visible. Gravity and decelaration g-force are suppressed in the figure because they are applied in all nodes.

5.4.7 Modal analysis model: explicit to implicit advisor

There are some adjustments that need be done to the explicit model in order to perform the modal analysis in PAM-CRASH implicit code. First, in the *Checks* menu, the *Explicit to Implicit*

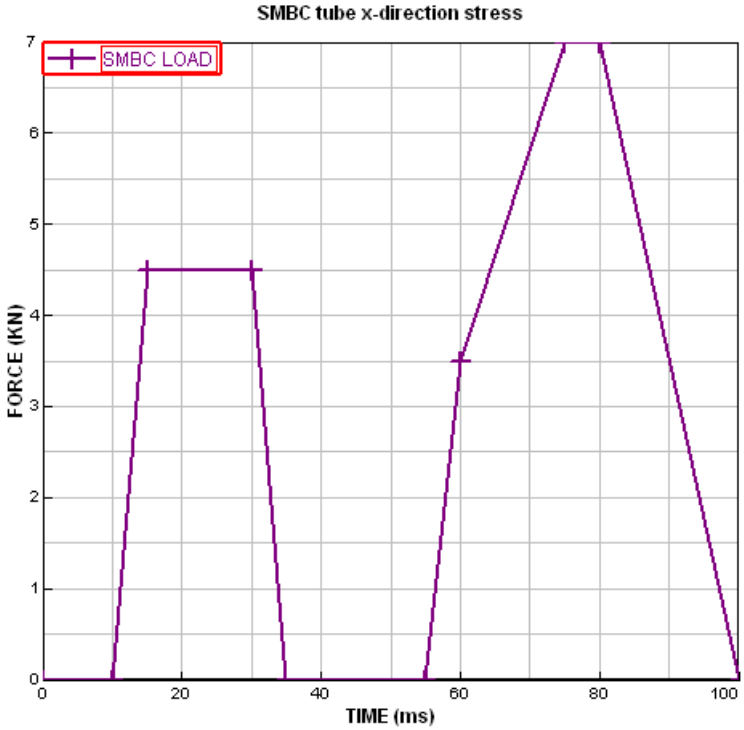

Figure 5.29: HVAC loading.

Advisor tool, Figure 5.35, warns the user to the necessary model changes to be compatible with implicit analysis. During this step, rigid bodies are replaced by multiple to one node constraints *(MTOCOs)* due to implicit code incompatibilities, specifically redundancy and inadequacy, [17]. After this step, material law is defined as elastic due computing costs, loads are eliminated and fixed boundary conditions are replaced by 6 DOF springs with linear stiffness. Localized body stiffness is defined in Table 5.12. Furthermore, boundary conditions were added to the A-pillar bracket LHS bolted area.

The spring beam elements are connected to the independent node of *MTOCO* at one tip and fixed at the opposite tip, as depicted in Figure 5.37. The *MTOCO* are defined as shown in Figure 5.37. The constraint dependent nodes are selected from the bolted area elements and the independent node is placed in the center of the circular hole, Figure 5.37. The beam direction is normal to the shell plane and its length simulates the bolted connection thickness. This length was defined as 4 mm at the A-pillars brackets bolted connections and 2 mm at the center legs.

The spring local coordinate system (R,S,T) was specified by the local coordinate frame (x,y,z), visible in Figure 5.38. These spring local directions can be also defined by four nodal points that define them as depicted in Figure 5.36. The spring frame is then taken to coincide with local frame directions. In implicit analysis, the frame is always treated as fixed orientation throughout the simulation. To finished the spring definition a material needs to be associated. In PAM-CRASH 6 DOF spring material designation is *220-NONLINEAR_6DOF_SPRING_DASHPOT*. Figure 5.38 shows one of the center legs springs material editor. Local stiffness is defined in this window.

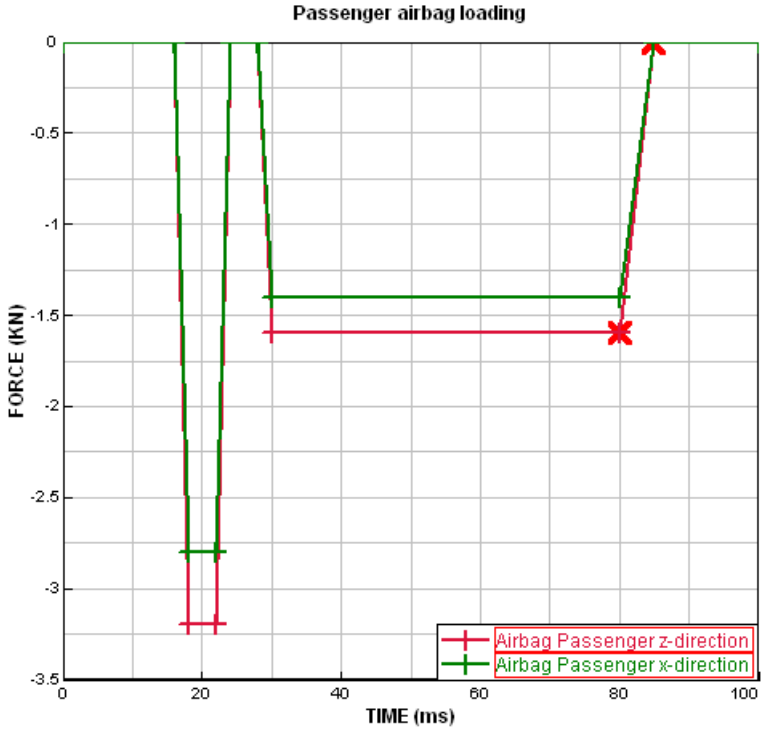

Figure 5.30: Passenger's airbag loading.

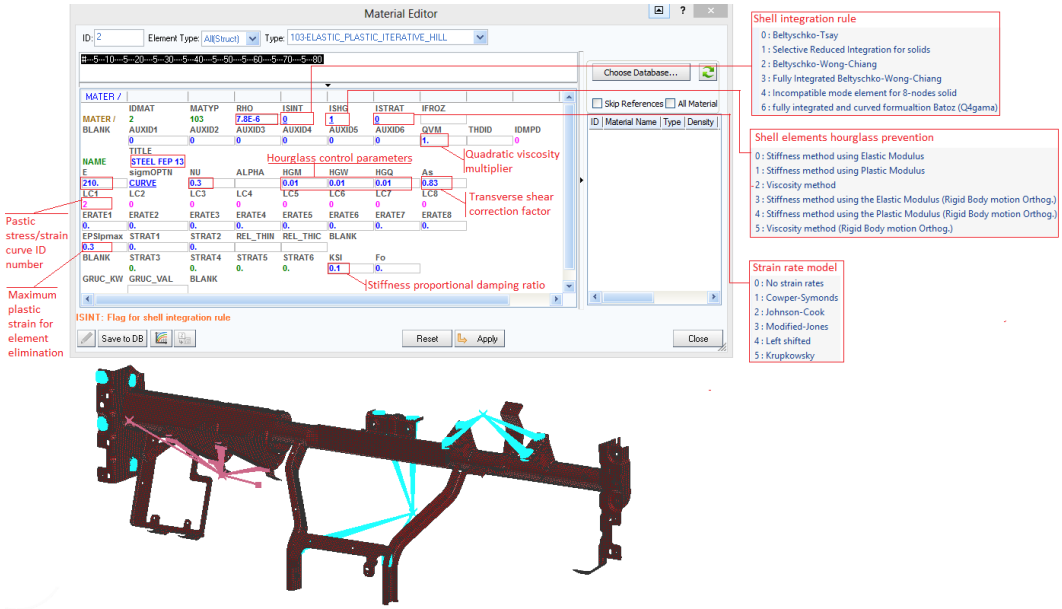

Figure 5.31: FE model material law definition in PAM-CRASH.

Last but not least, before exporting the modal analysis model, Figure 5.39, two control cards need to be defined. The first control card, ICTRL, is where the implicit analysis type is defined. Modal analysis is qualified as *Dynamics* and *linear* in this card. EIGEN control card defines the algorithm of eigen modes extraction and their number as shown in Figure 5.40.

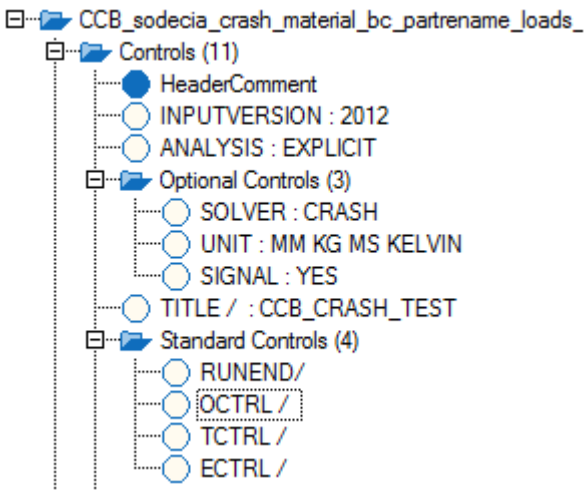

Figure 5.32: Control cards.

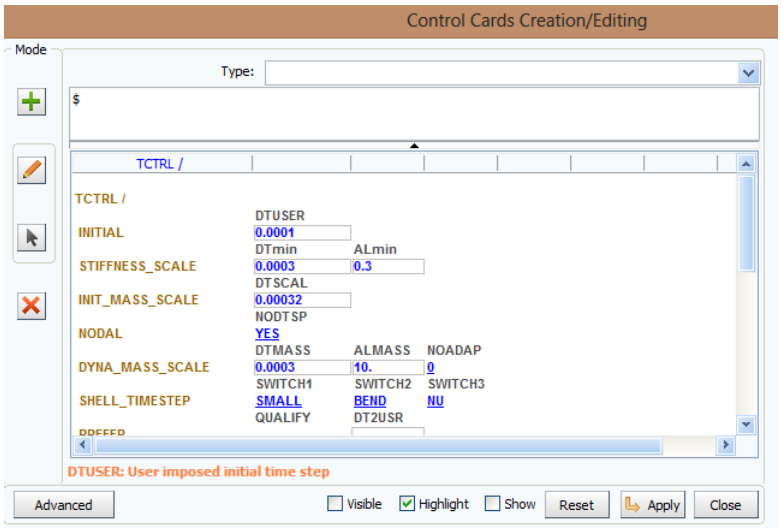

Figure 5.33: TCTRL card.

Table 5.7: First cardan loading.

First cardan loading			
Time (*ms*)	X-direction stress (*kN*)	Y-direction stress (*kN*)	Z-direction stress (*kN*)
0	0	0	0
39	0	0	0
40	1.348	-0.335	1.439
41	1.327	-0.339	1.457
42	1.306	-0.344	1.475
43	1.283	-0.348	1.494
44	1.260	-0.352	1.512
45	1.236	-0.357	1.531
46	1.212	-0.361	1.550
47	1.186	-0.365	1.569
48	1.159	-0.370	1.587
49	1.131	-0.374	1.606
50	1.103	-0.379	1.625
51	1.073	-0.383	1.644
52	1.042	-0.387	1.662
53	1.010	-0.392	1.681
54	0.978	-0.396	1.699
55	0.944	-0.400	1.717
56	0.909	-0.404	1.735
57	0.873	-0.408	1.753
58	0.836	-0.412	1.770
59	0.797	-0.416	1.786
60	0.758	-0.420	1.803
61	0.718	-0.424	1.818
62	0.676	-0.427	1.833
63	0.634	-0.430	1.847
64	0.591	-0.434	1.861
65	0.546	-0.437	1.874
66	0.501	-0.439	1.886
67	0.455	-0.442	1.897
68	0.408	-0.444	1.907
69	0.361	-0.446	1.916
70	0.313	-0.448	1.924
71	0.264	-0.450	1.931
72	0.215	-0.451	1.937
73	0.165	-0.452	1.941
74	0.115	-0.453	1.945
75	0.065	-0.454	1.947
76	0.015	-0.454	1.948
77	-0.035	-0.454	1.948
78	-0.085	-0.453	1.946
79	-0.135	-0.453	1.943
80	-0.185	-0.452	1.939

Table 5.8: HVAC loading.

HVAC loading	
Time (ms)	X-direction stress (kN)
0	0
20	0
30	4
60	4
65	0
100	0

Table 5.9: SMBC loading.

SMBC loading	
Time (ms)	X-direction stress (kN)
0	0
10	0
15	4
30	4
35	0
55	0
60	3
75	6.5
80	6.5
100	0

Table 5.10: Passenger's airbag loading.

Passenger's airbag loading		
Time (ms)	X-direction stress (kN)	Z-direction stress (kN)
0	0	0
16	0	0
18	-2.8	-3.2
22	-2.8	-3.2
24	0	0
28	0	0
30	-1.4	-1.6
80	-1.4	-1.6
85	0	0
100	0	0

Table 5.11: CCB accelaration fields.

CCB accelaration fields			
Time (ms)	Gravity (z-dir.) $\left(mm/ms^{-2}\right)$	Time (ms)	Deceleration in x-dir. $\left(mm/ms^{-2}\right)$
0	-0.0098	0	0.075460
150.01	-0.0098	22	0.075460
		25	0.17934
		40	0.17934
		43	0.49294
		67	0.49294
		70	0

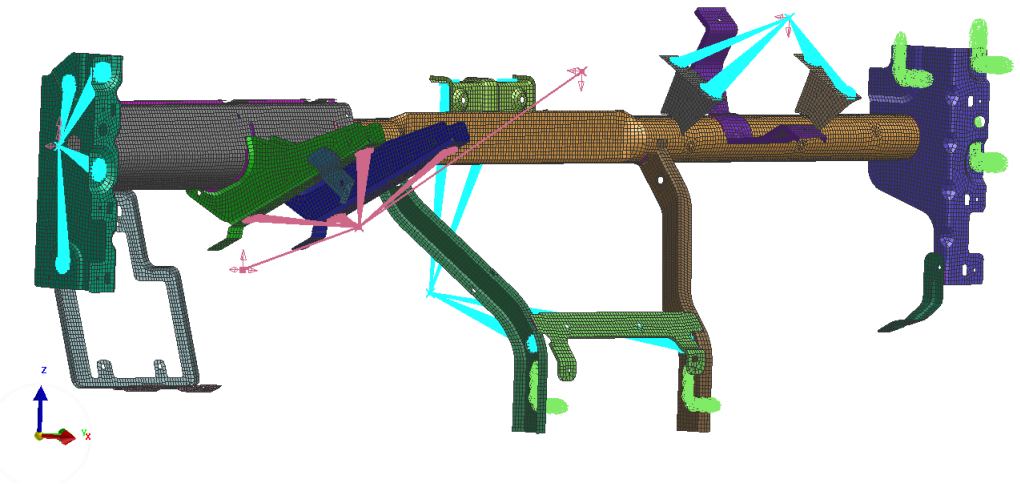

Figure 5.34: Crash simulation model. Rigid bodys are defined in blue, fixed boundary conditions are defined in green and *MTOCO*s are defined in pink as well as loads vectors.

Table 5.12: Localized body stiffness, .

Driver's Cowlside	
Kx	5 kN/mm
Ky	1 kN/mm
Kz	12 kN/mm
Passenger Cowlside	
Kx	5 kN/mm
Ky	1 kN/mm
Kz	12 kN/mm
Floor Tunnel	
Kx	12 kN/mm
Ky	5 kN/mm
Kz	1 kN/mm

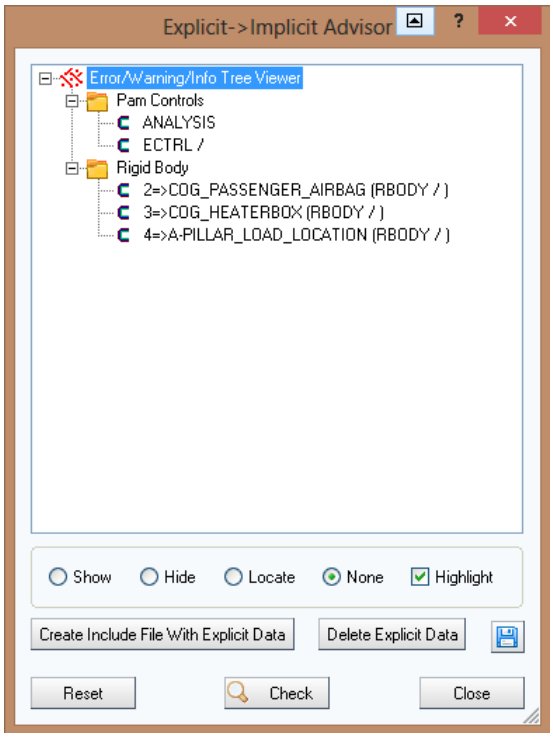

Figure 5.35: *Explicit to Implicit Advisor* window.

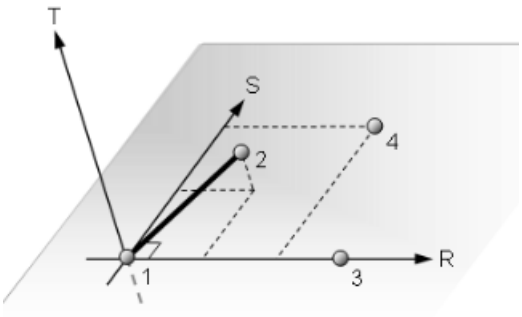

Figure 5.36: Four nodal points spring's direction definition.

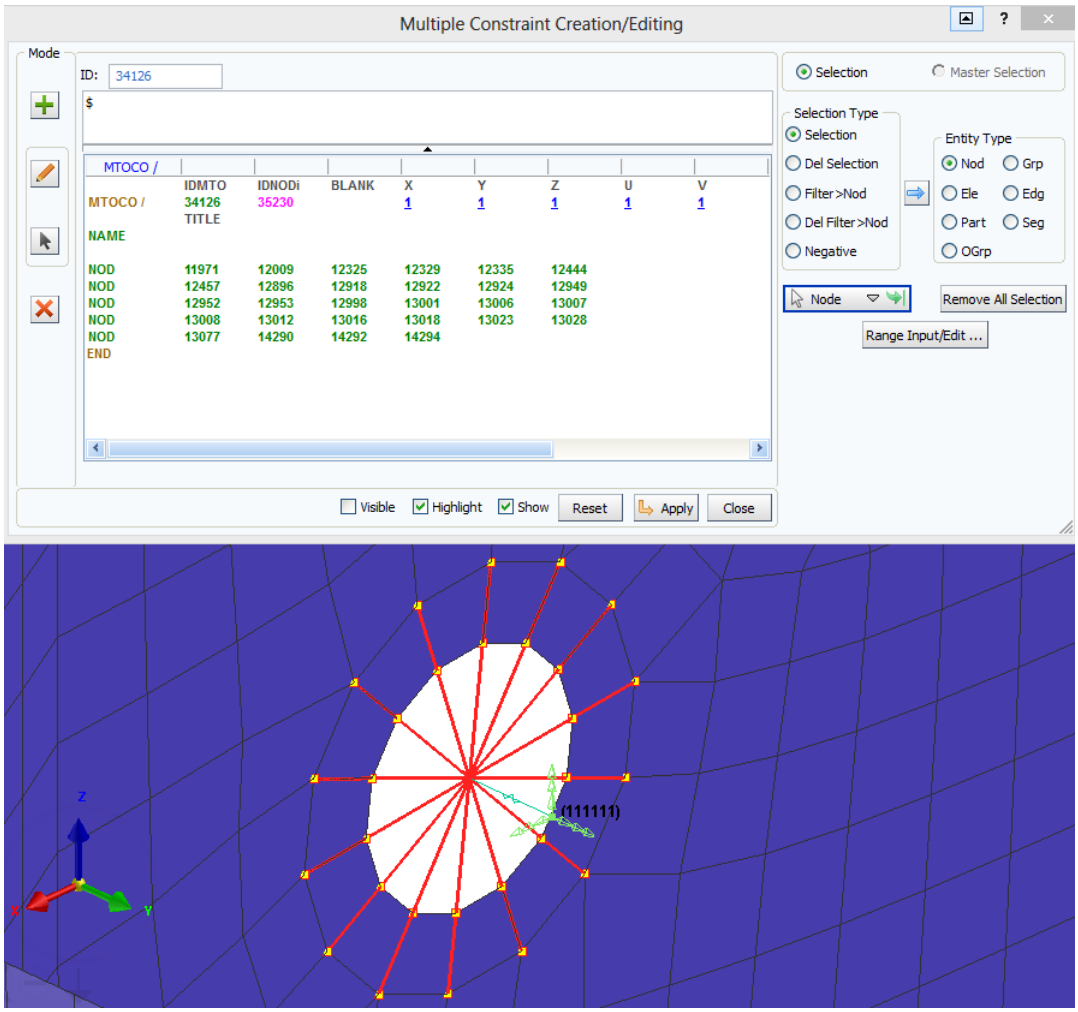

Figure 5.37: 6 DOF spring with linear stiffness boundary condition setting.

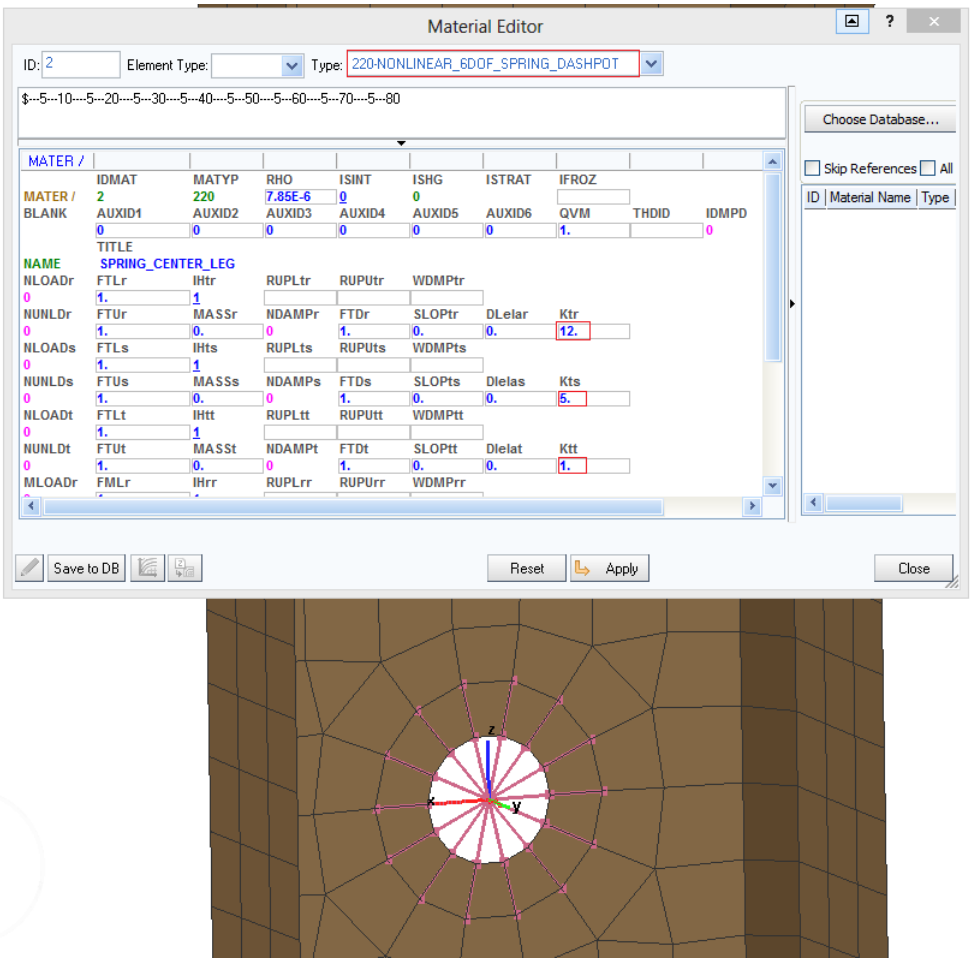

Figure 5.38: Spring material editor.

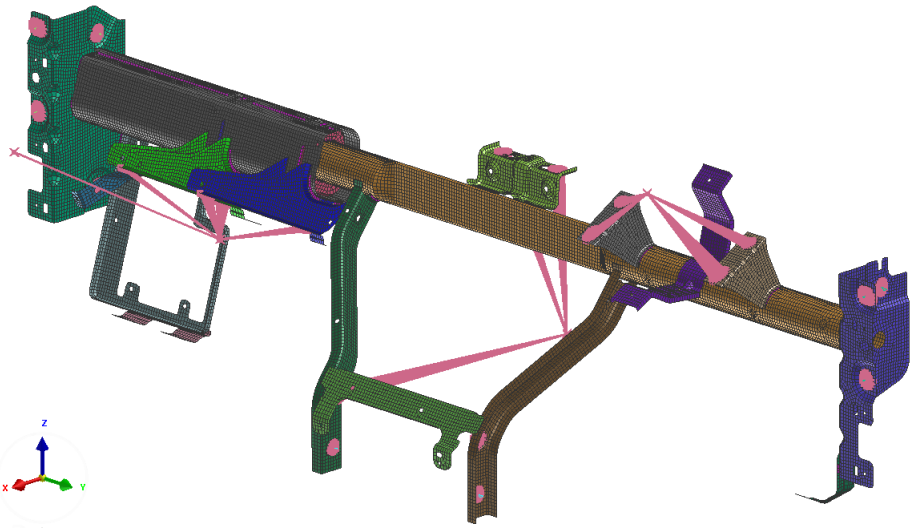

Figure 5.39: Modal analysis model.

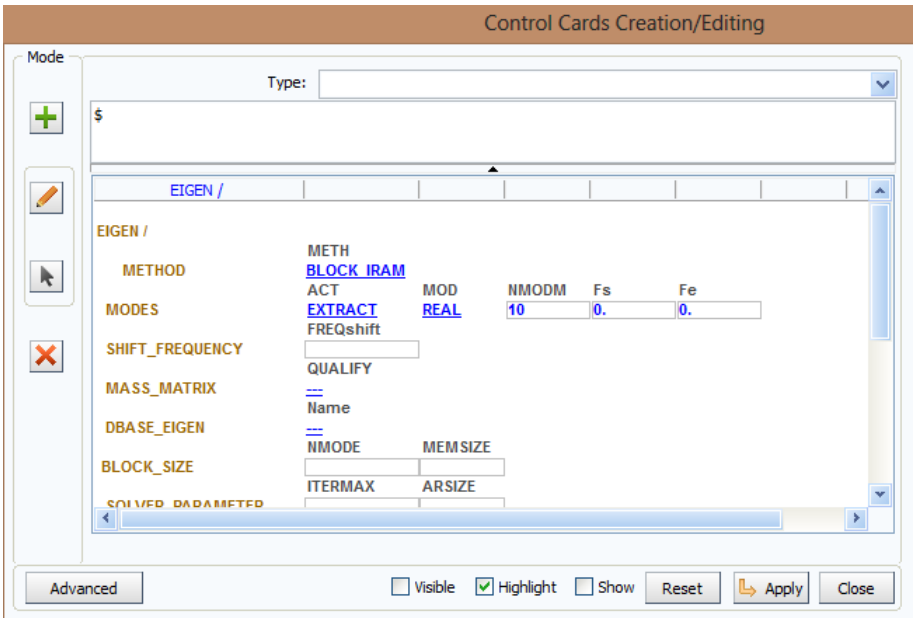

Figure 5.40: EIGEN control card.

PAM-CRASH Results

6.1 Crash simulation results

As previously mentioned, there is no available technical information about the present cross car beam crashworthiness. With the adapated loads from a Renault technical specification, the crash simulation results are presented in the following Figures 6.1, 6.2 and 6.3. The nodal displacements results, Figure 6.1, show that during the overlaped crash event of this CCB, there is a sigificant intrusion of the instrument pannel into the vehicle cabin of approximately 177 mm. The von Mises stress results, Figure 6.2, show that the center legs, passenger airbag brackets and the A-pillar brackets are the CCB components where the highest stress concentration points are located during the crash event. Last but not least, the maximum plastic strain results, Figure 6.3, revealed that the CCB connection to the vehicle's floor tunnel is a weak point, as rupture strain is predicted, as shown by element elimination arround fixed boundary nodes. Other weak points, where rupture strain is predicted, are the weld beads that connect the center legs to the generic beam. Figure 6.4 shows the global kinetic and internal energy balance. Unlike a typical crash test car in which a car moving at a certain speed crashes to a barrier and where its kinetic energy is completly transformed into internal energy, in this model exterior loads are applied to a stationary model. Thus, as the structure undergoes stresses, it starts to warp and moves and, therefore, internal energy increases and kinetic energy oscilates with some nodal points movement.

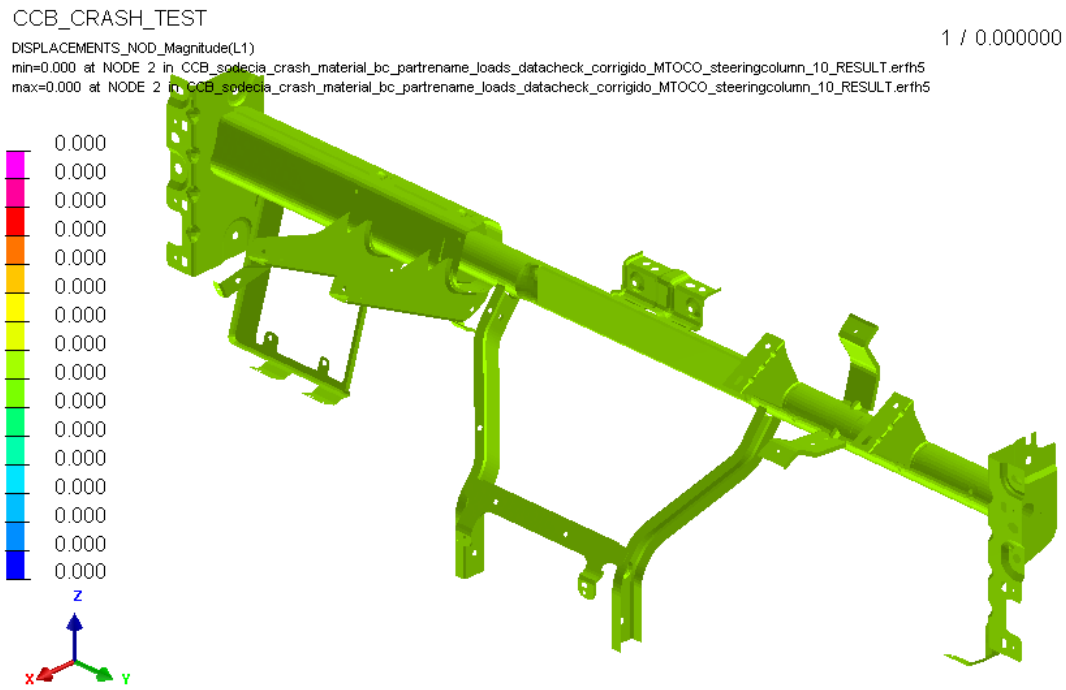

(a) Time: 0 ms.

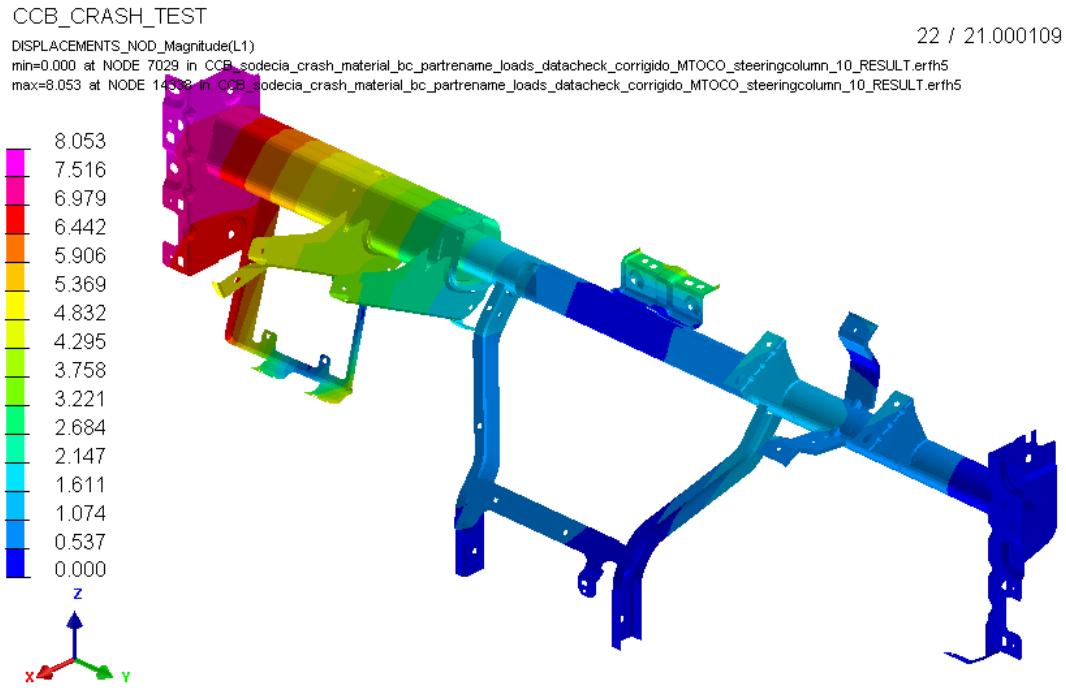

(b) Time: 21 ms.

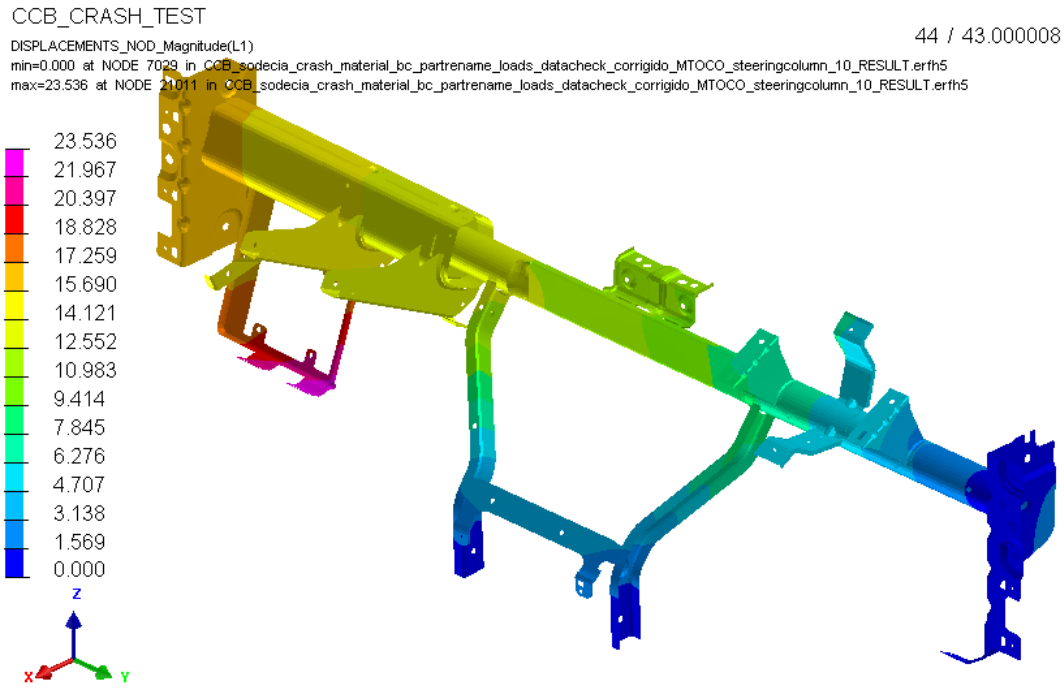

(c) Time: 43 ms.

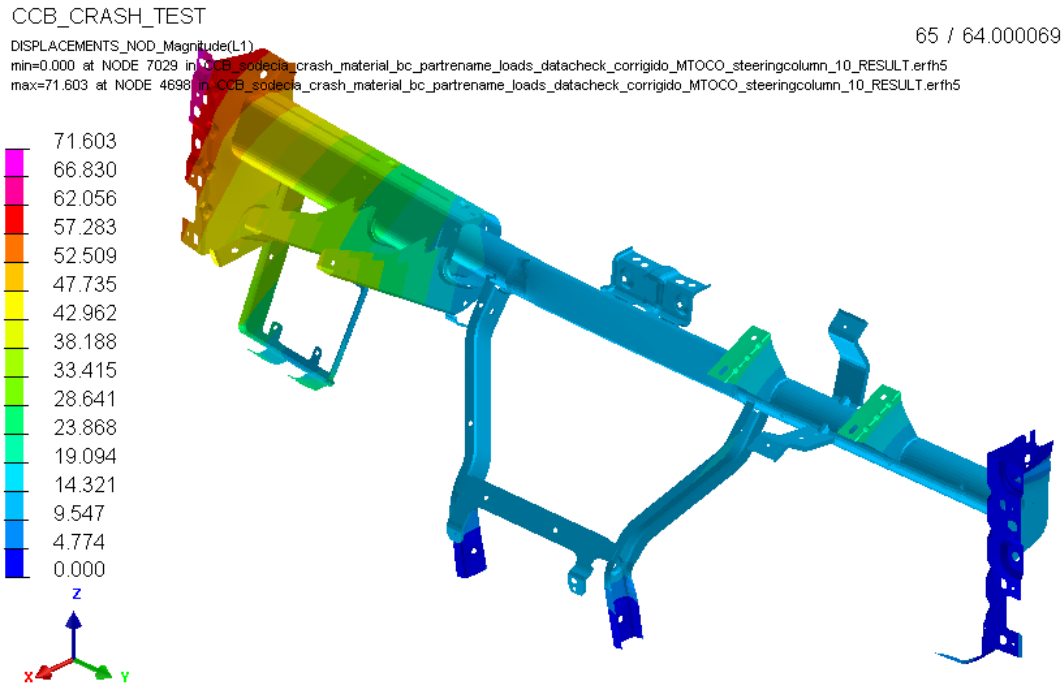

(d) Time: 64 ms.

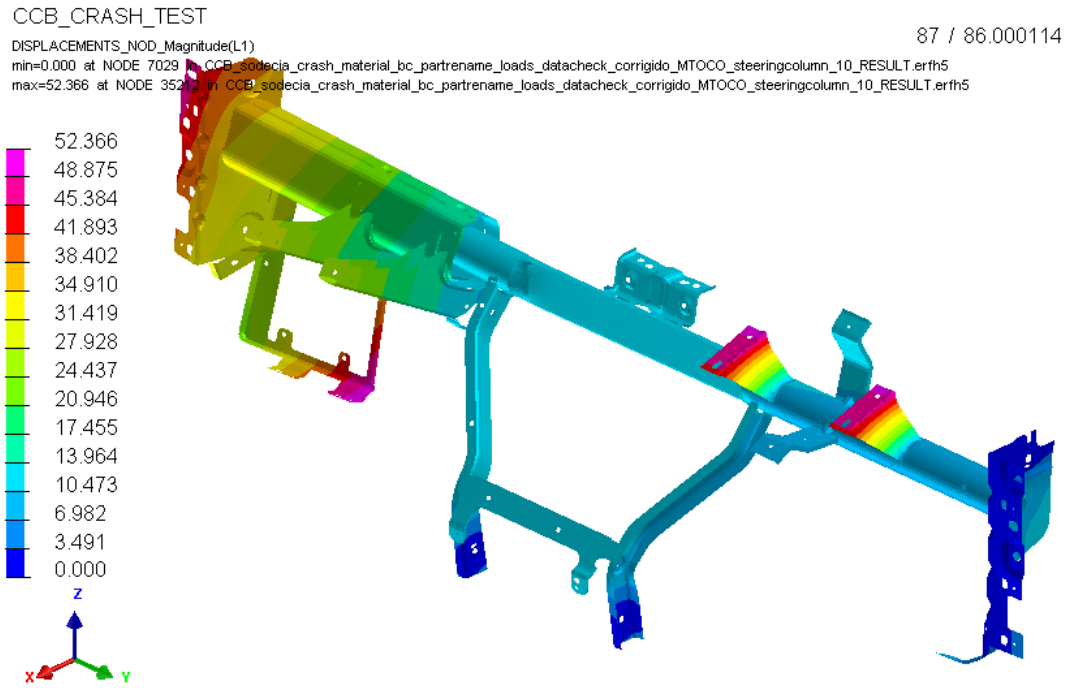

(e) Time: 86 ms.

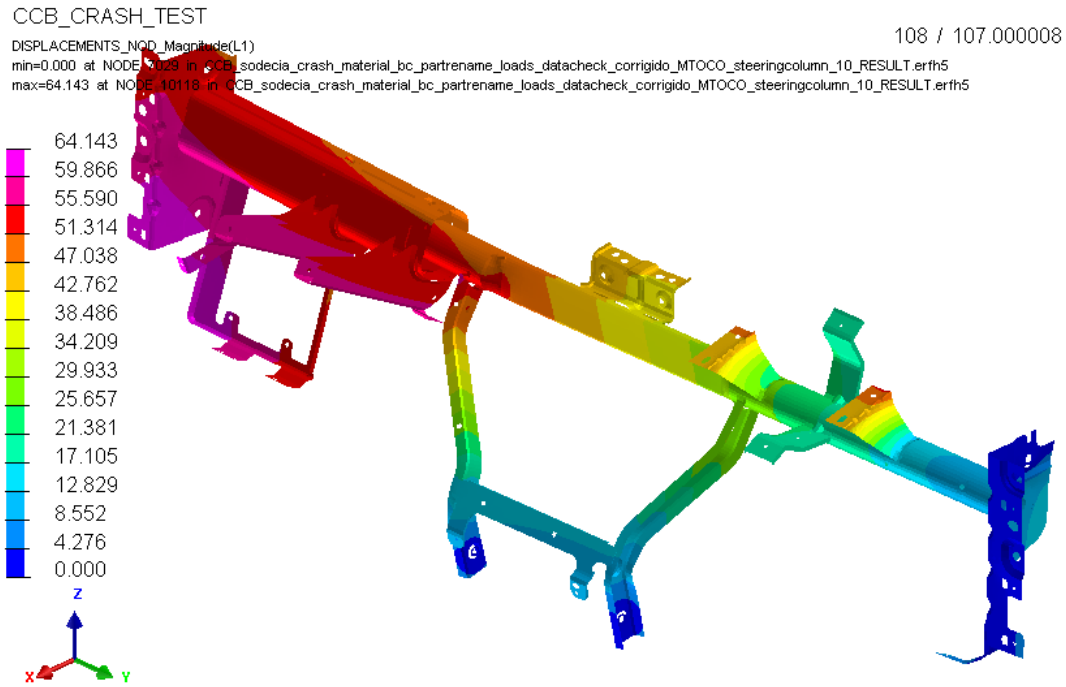

(f) Time: 107 ms.

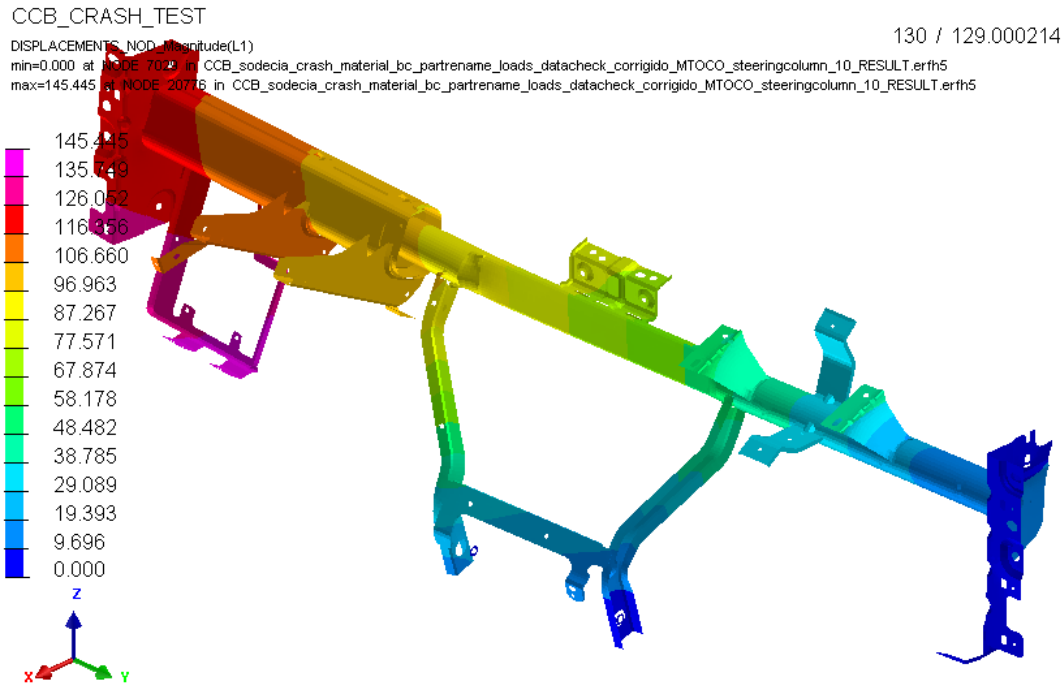

(g) Time: 129 ms.

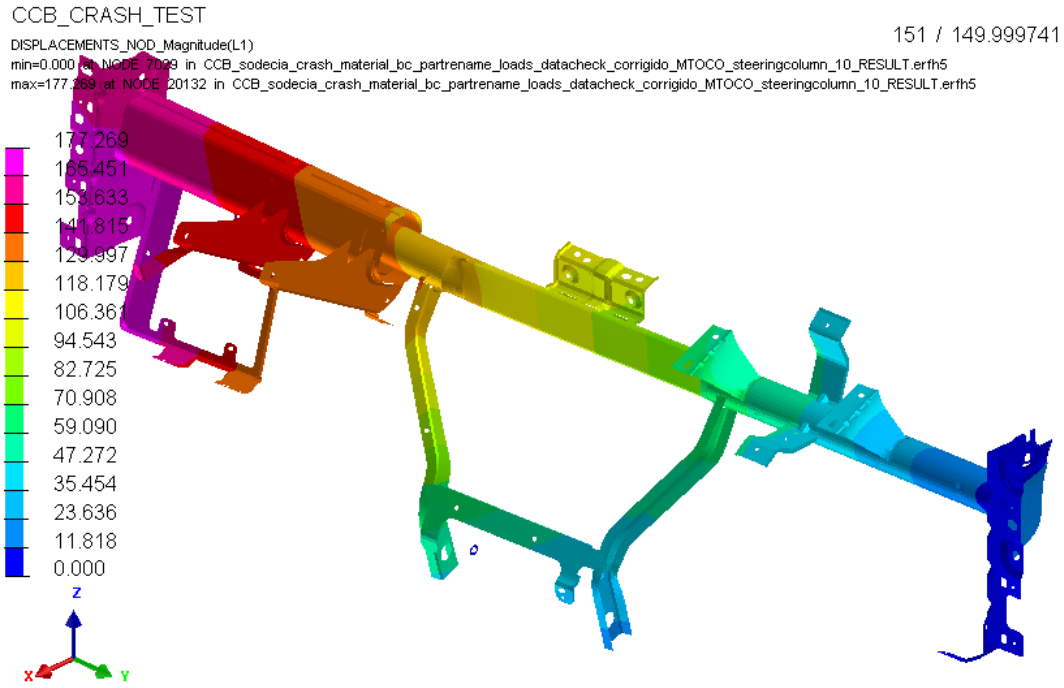

(h) Time: 150 ms

Figure 6.1: Nodal displacement magnitude during crash simulation.

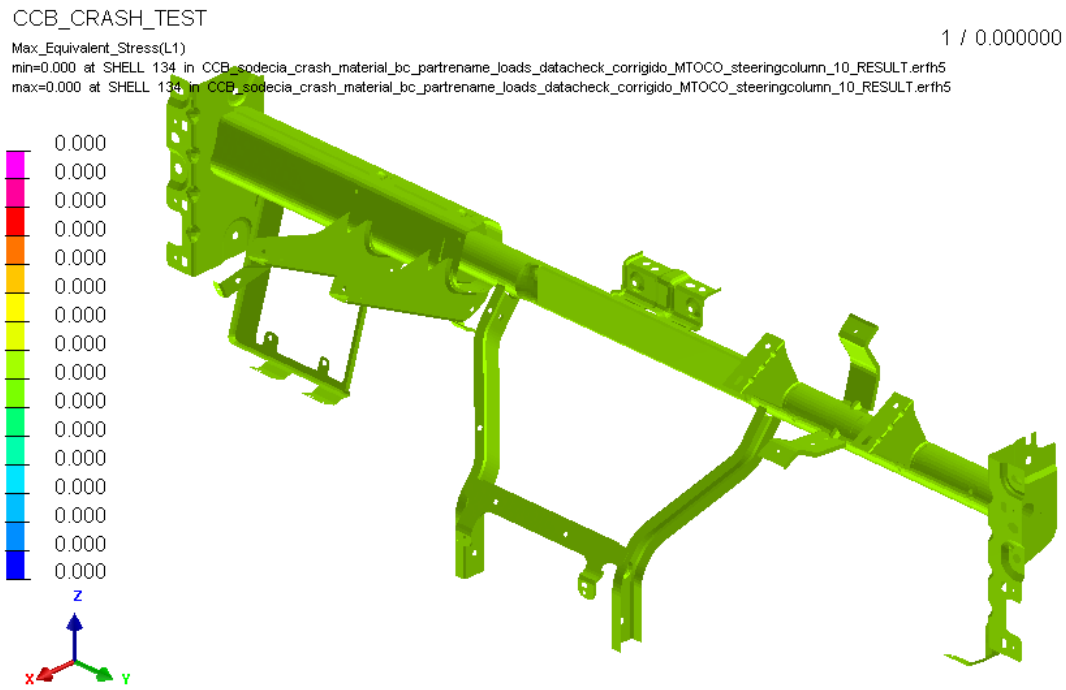

(a) Time: 0 ms.

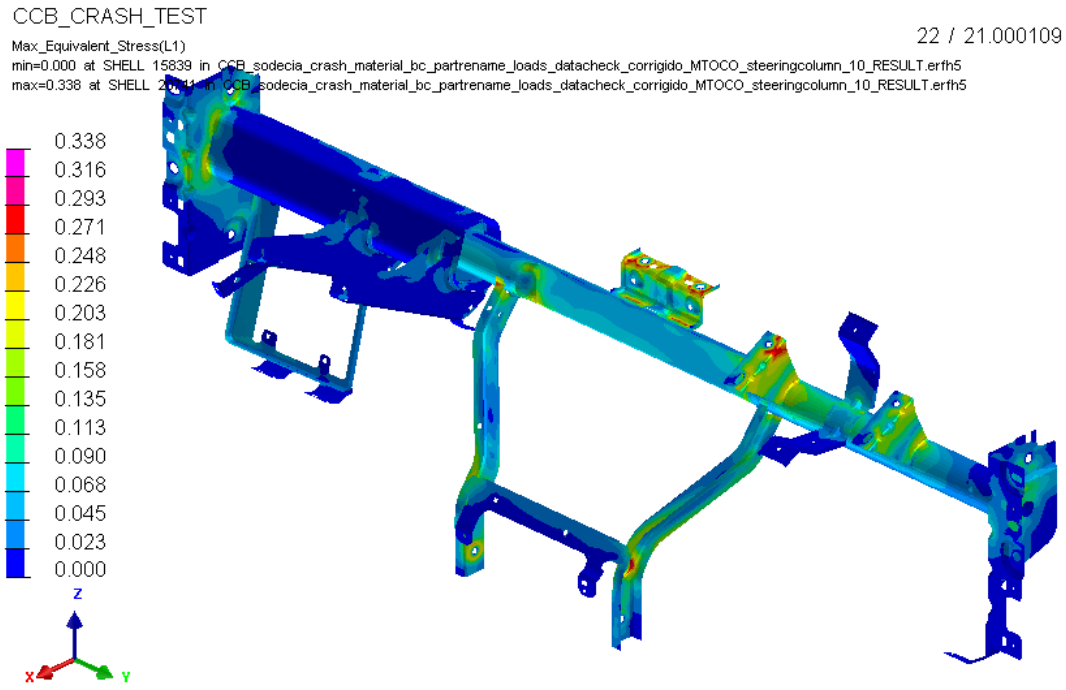

(b) Time: 21 ms.

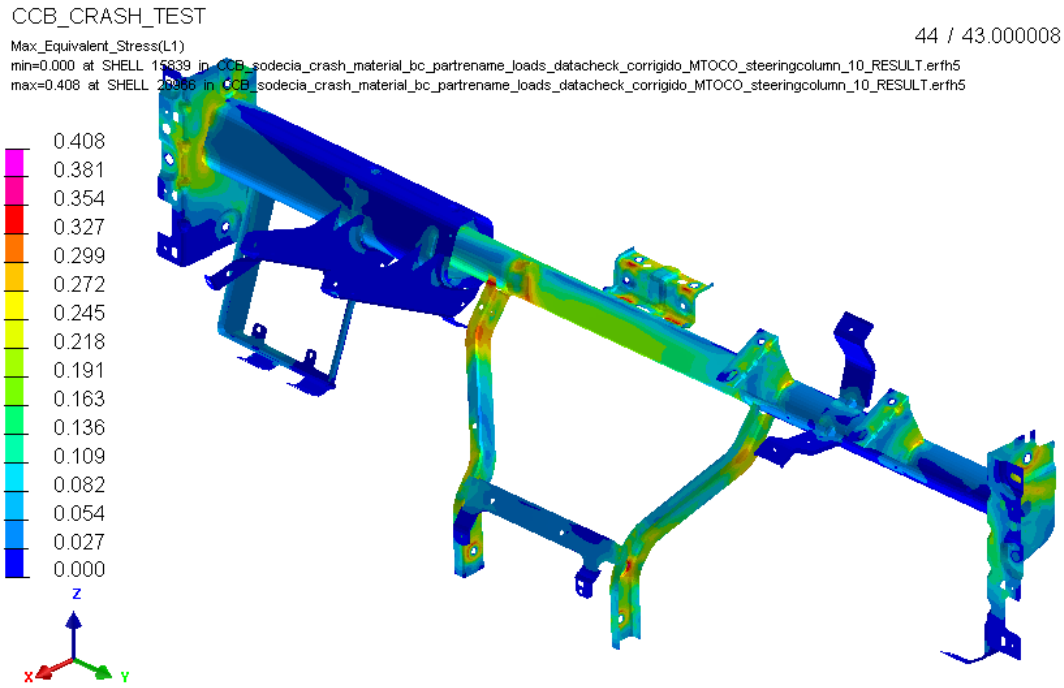

(c) Time: 43 ms.

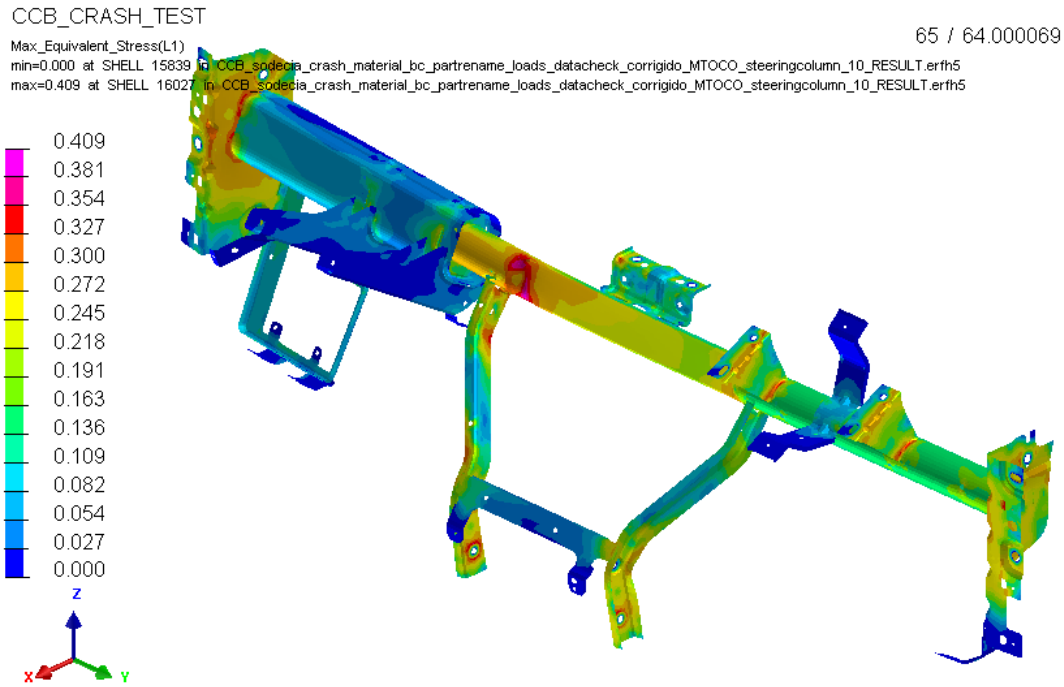

(d) Time: 64 ms.

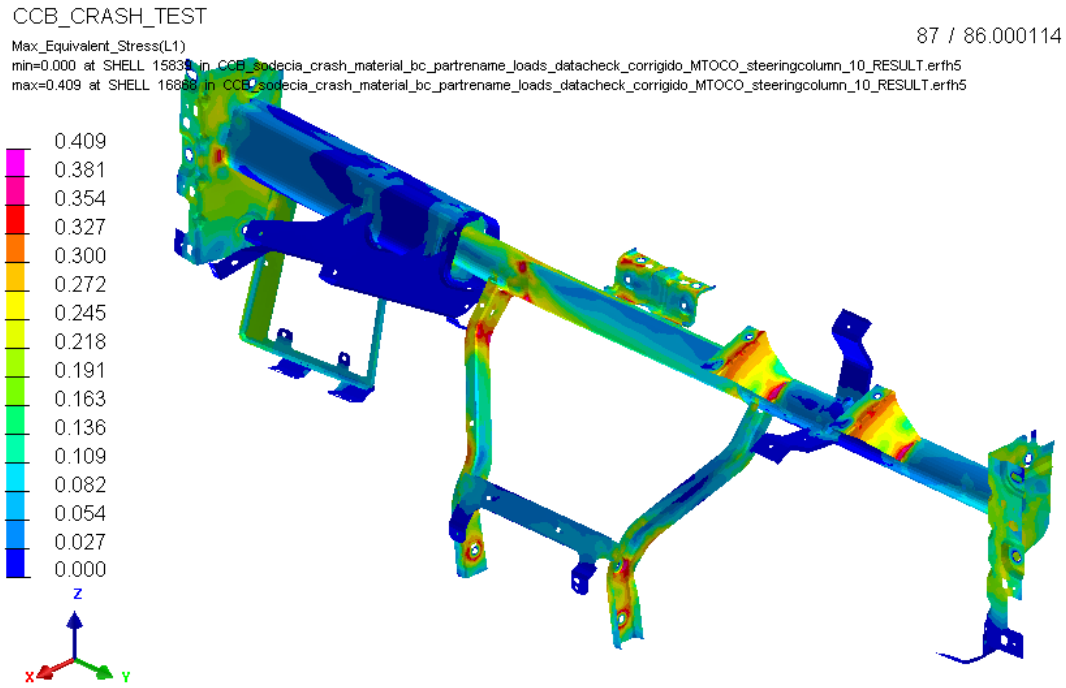

(e) Time: 86 ms.

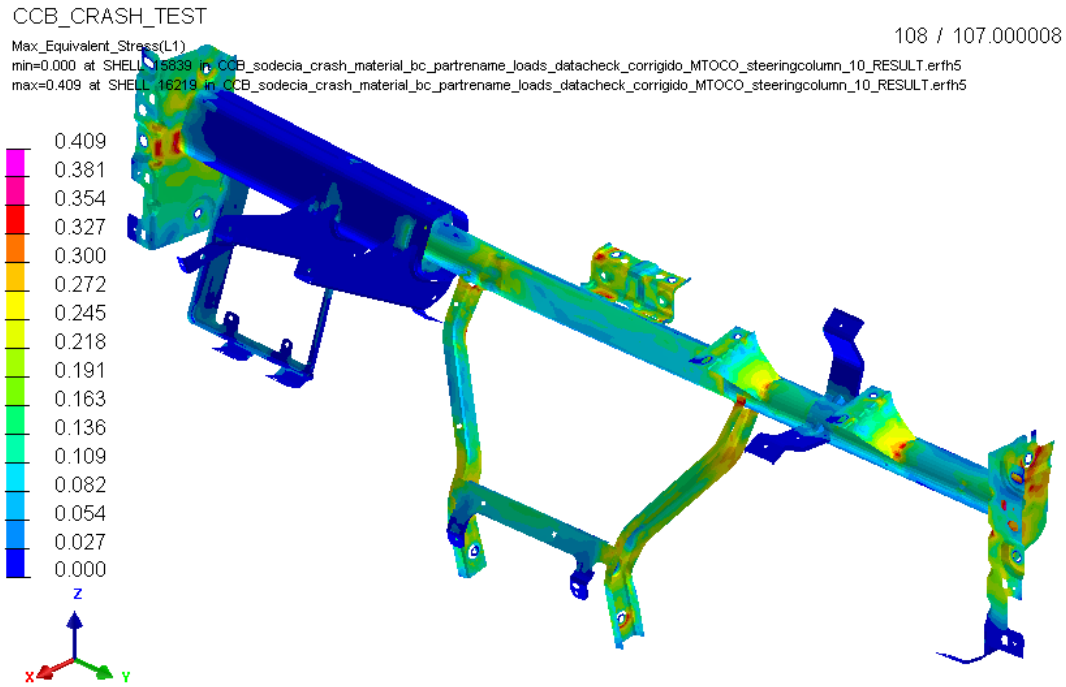

(f) Time: 107 ms.

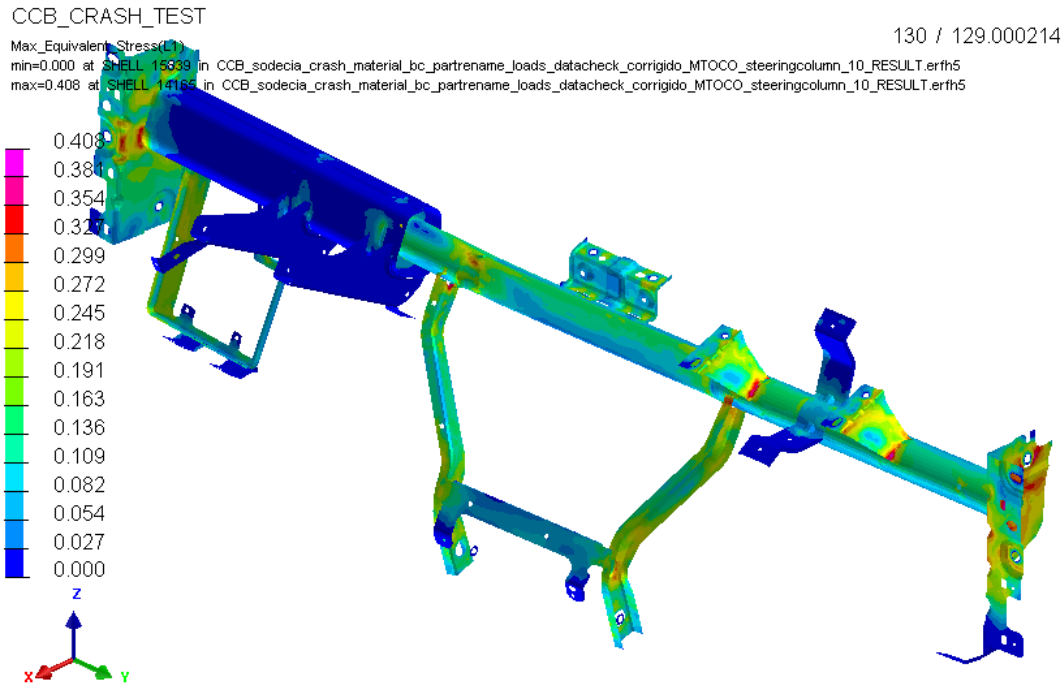

(g) Time: 129 ms.

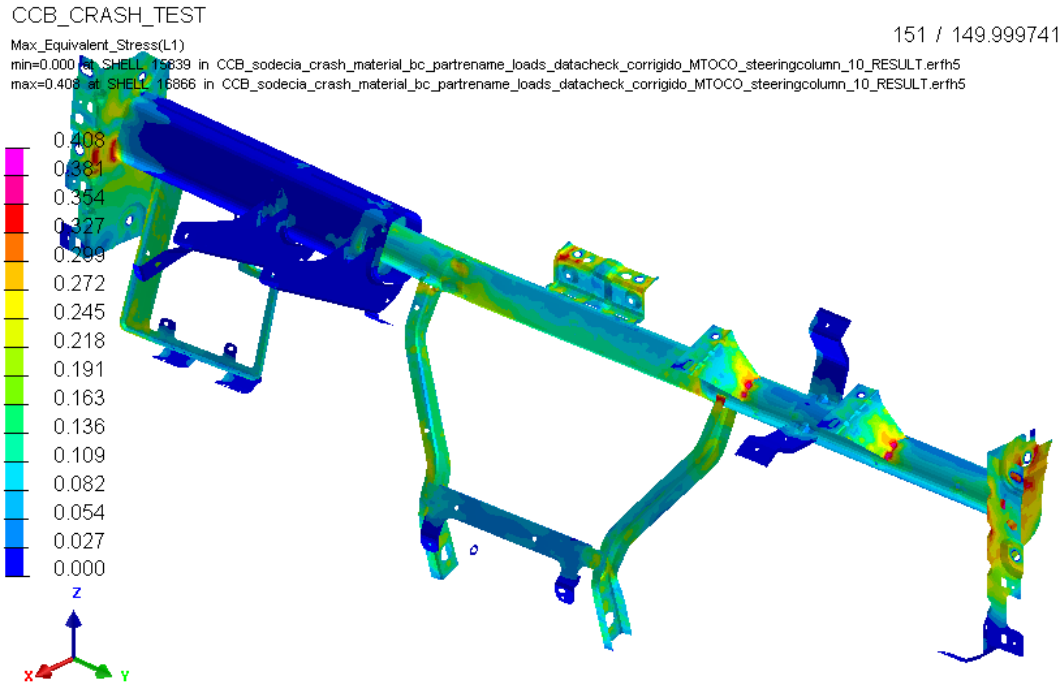

(h) Time: 150 ms

Figure 6.2: von Mises stress distribution during crash simulation.

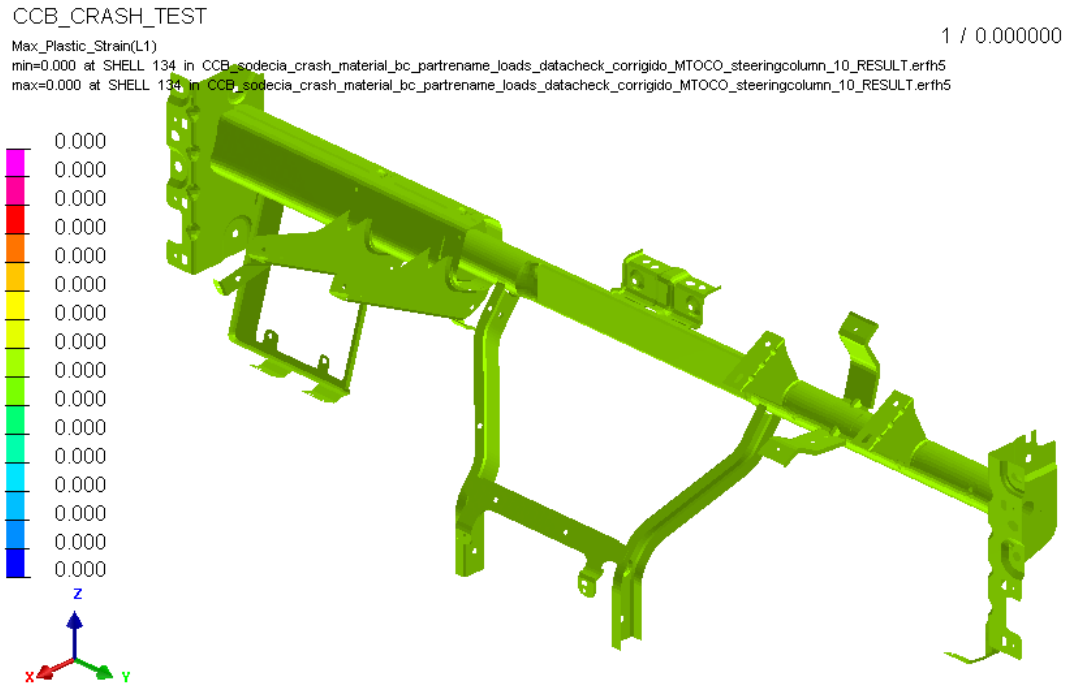

(a) Time: 0 ms.

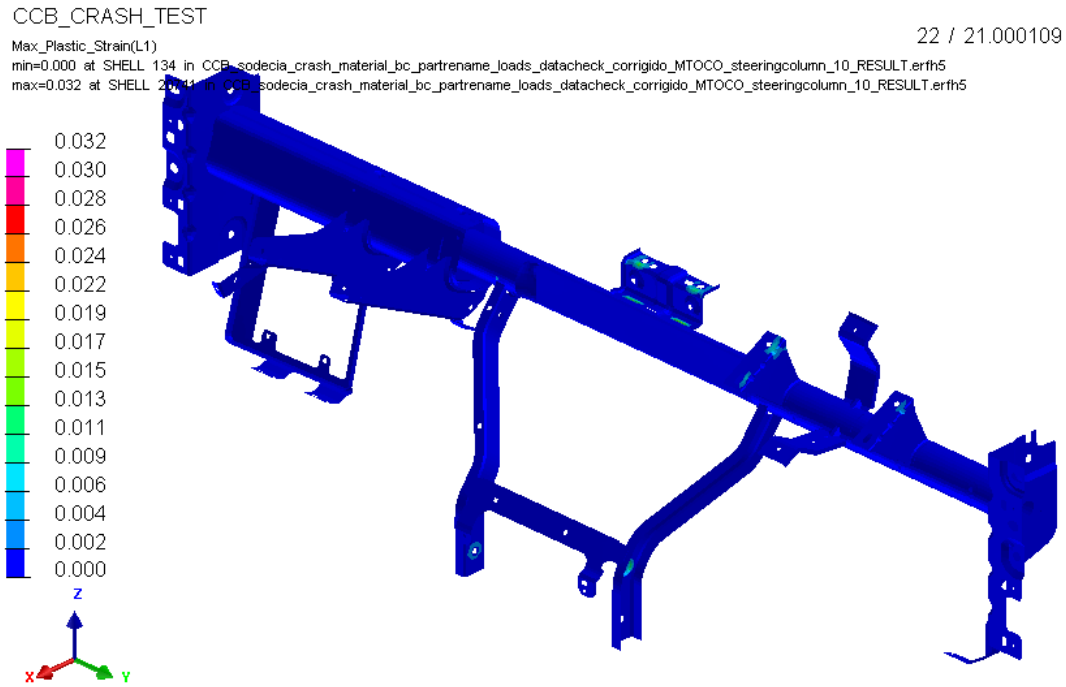

(b) Time: 21 ms.

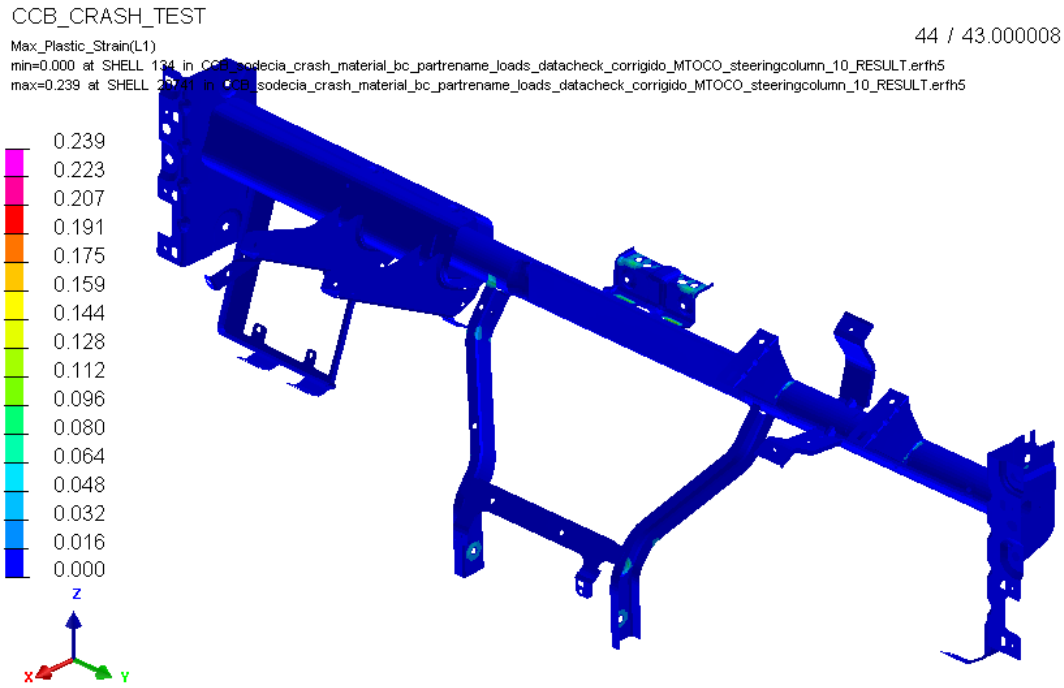

(c) Time: 43 ms.

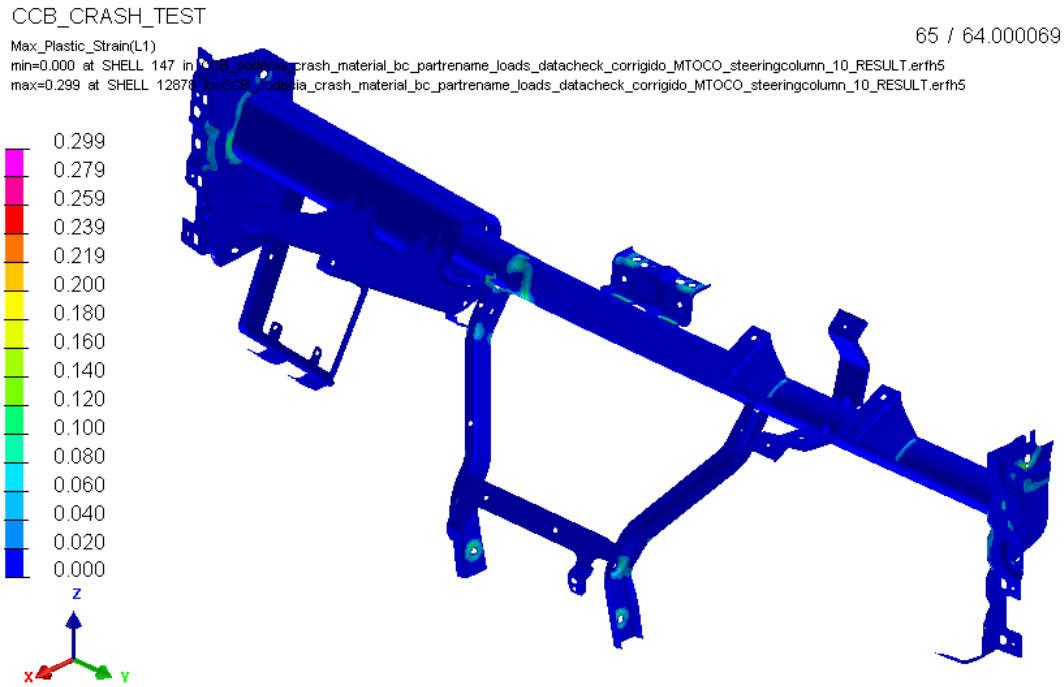

(d) Time: 64 ms.

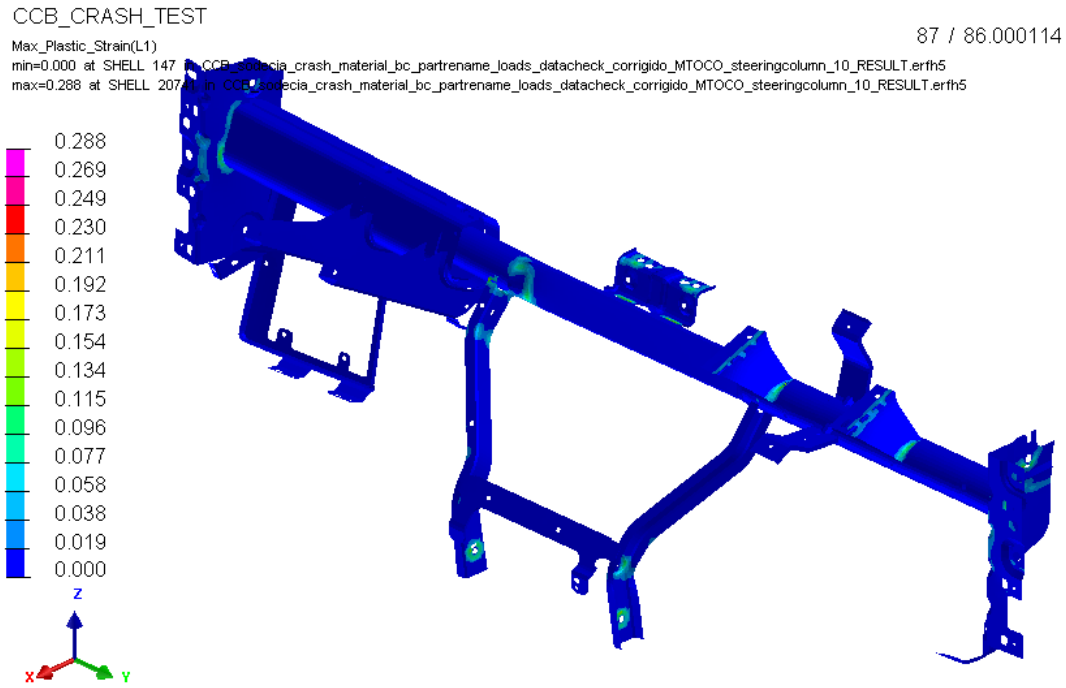

(e) Time: 86 ms.

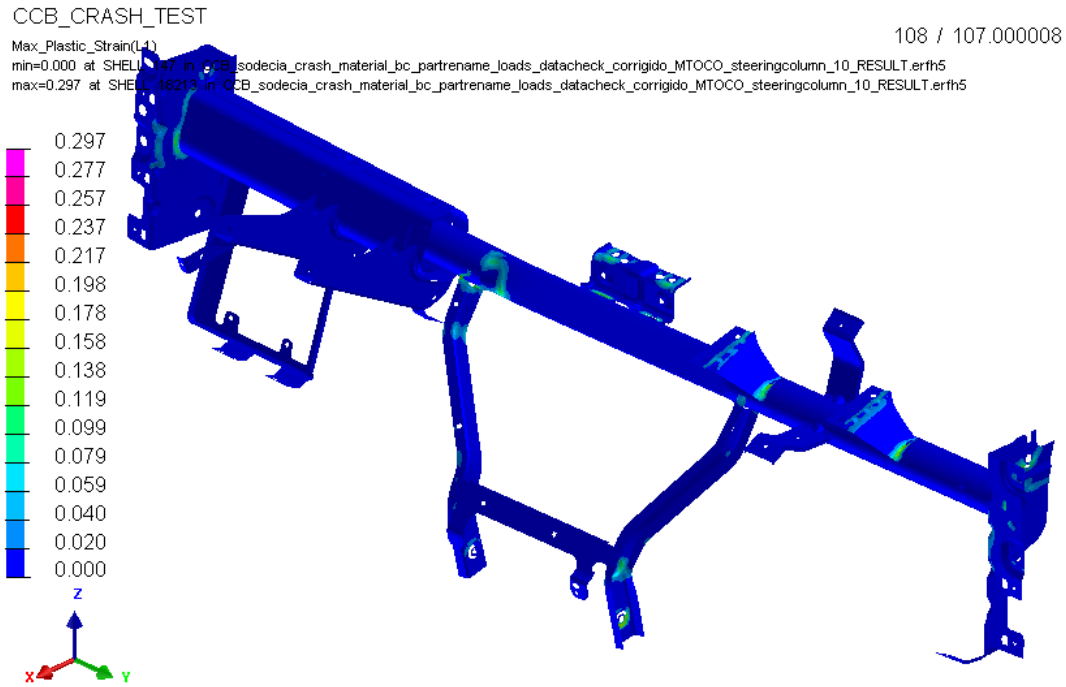

(f) Time: 107 ms.

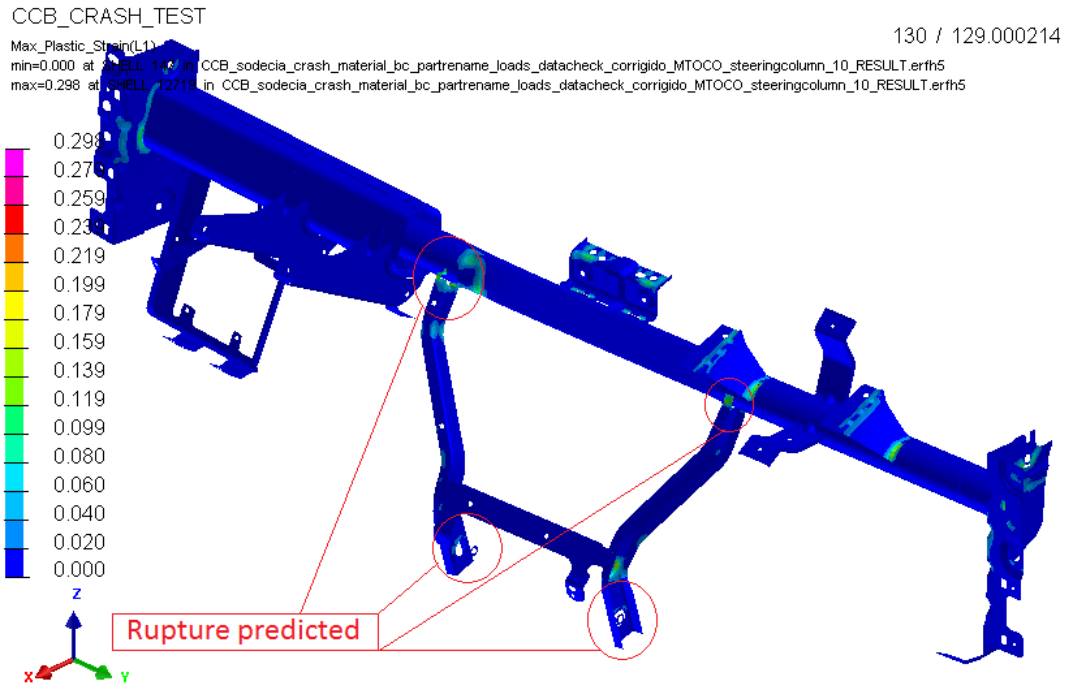

(g) Time: 129 ms.

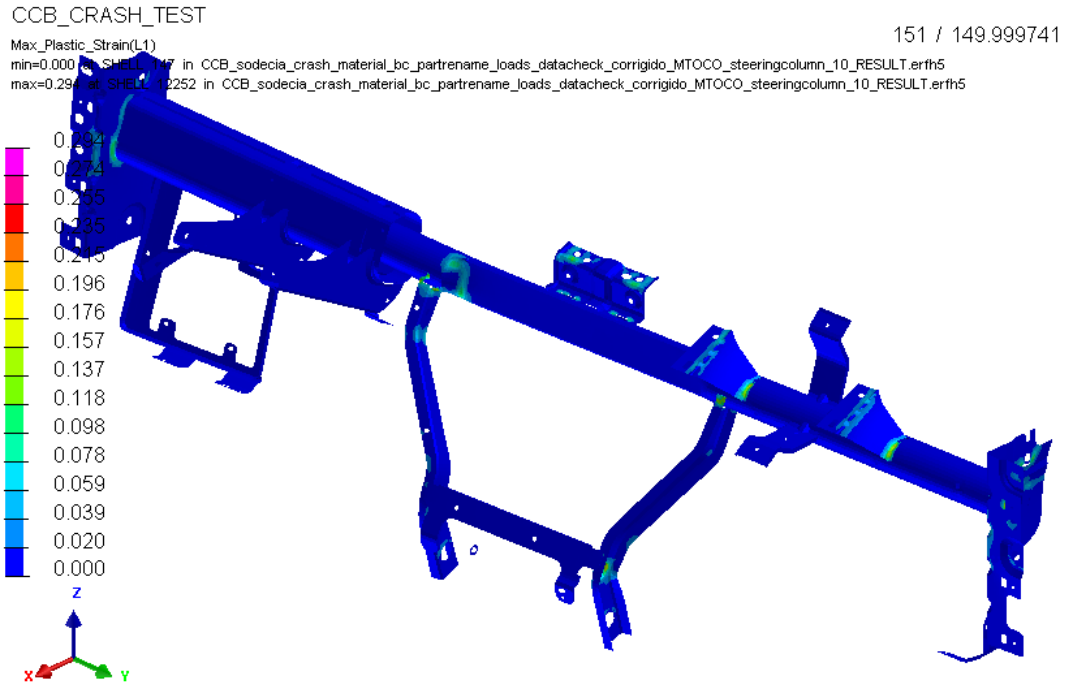

(h) Time: 150 ms

Figure 6.3: Maximum plastic strain during crash simulation.

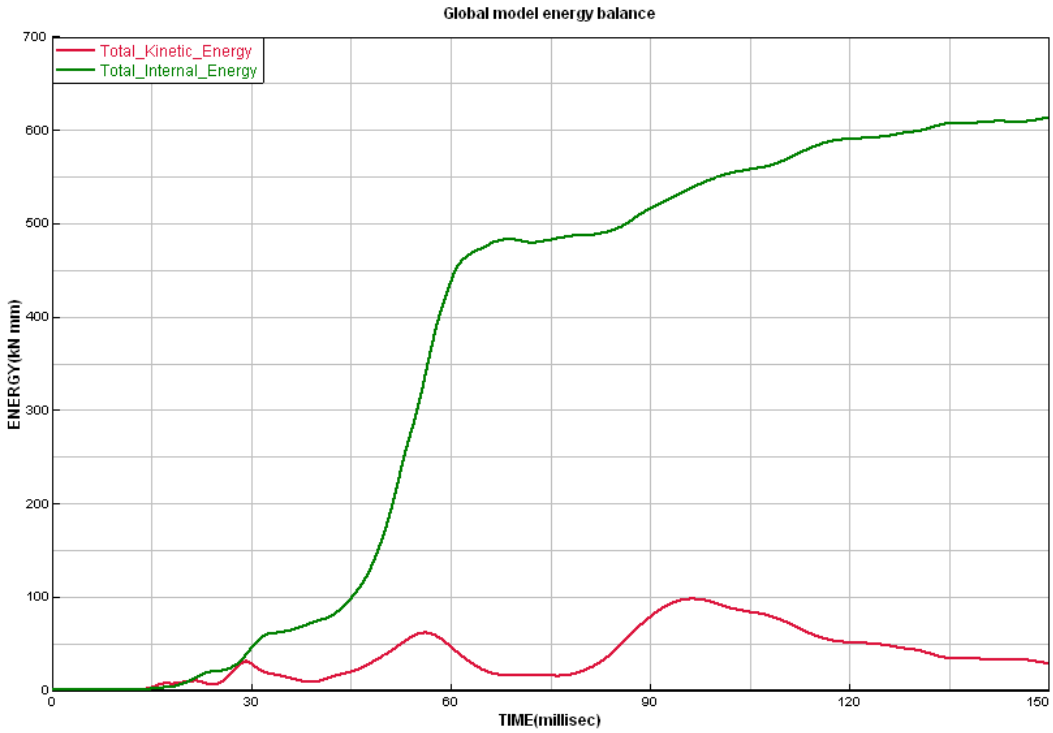

Figure 6.4: CCB global energy balance during crash simulation.

6.2 Modal analysis results

As a reference for the modal analysis results, Ford technical specification report states that the steering column first natural frequency design target is 32 Hz (data available for a similar ford CCB), [78]. Also concerning this natural frequence, it is written that, quoted from *System Design Specification,* [78], "The first vehicle I/P mode shall be separated from the first steering column mode by at least 5 HZ.".

Two modal analysis were performed in PAM-CRASH implicit, one local body stiffness (whereby the local stiffness of the body-in-white at the IP attachment locations is simulated by spring elements given in detail) and the other one with fixed boundary conditions. The following values were obtained:

- With localized body stiffness: $\omega_1 = 25.014\,Hz$ (fusebox bracket); $\omega_2 = 30.371\,Hz$ (steering column/heaterbox); $\omega_3 = 41.384\,Hz$ (passenger's airbag); $\omega_4 = 42.919\,Hz$ (passenger's airbag).

- With fixed boundary conditions: $\omega_1 = 25.560\,Hz$ (fusebox bracket); $\omega_2 = 40.776\,Hz$ (passenger's airbag); $\omega_3 = 45.058\,Hz$ (passenger's airbag); $\omega_4 = 49.186\ Hz$ (steering column/heaterbox/passenger's airbag).

The corresponding first modal shapes for the model with localized stiffness and for the fixed boundary conditions model are illustrated in Tables 6.1 and 6.2 and in Tables 6.3 and 6.4, respectively.

Examining the modal analysis results it is obvious that the fixed boundary conditions spoil

Table 6.1: CCB model with localized stiffness first two modal shapes.

CCB with localized body stiffness modal shapes
Mode 1
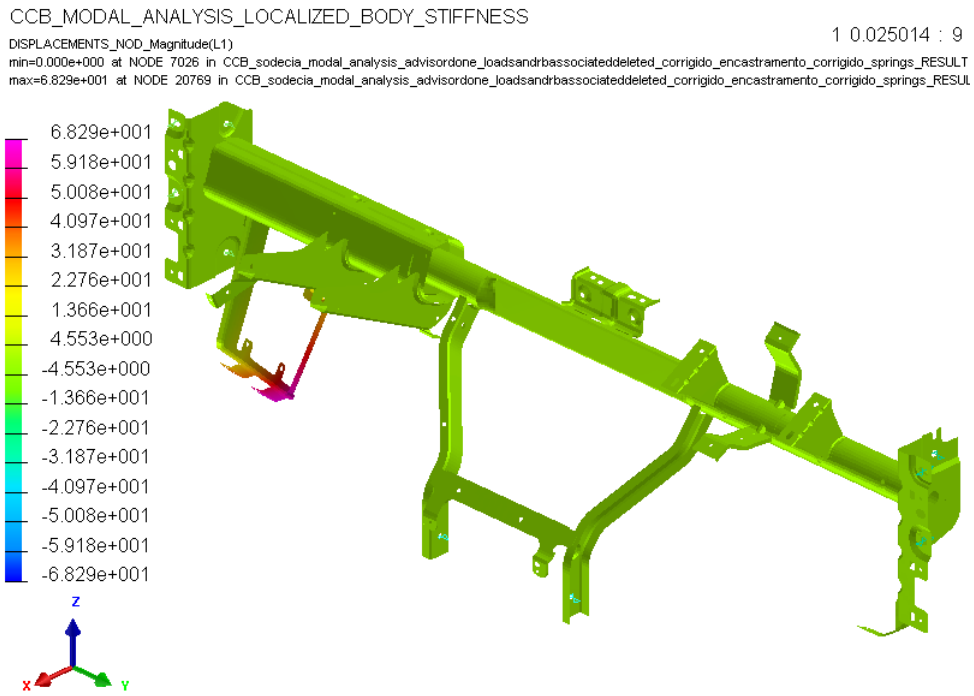
Mode 2
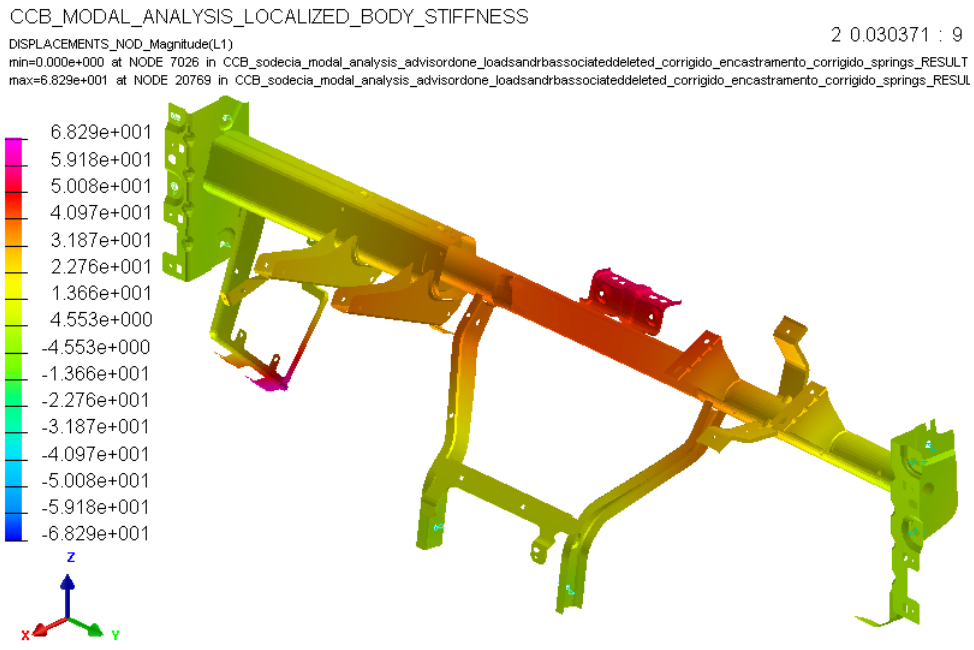

Table 6.2: CCB model with localized body stiffness third and fourth modal shapes.

CCB with localized body stiffness modal shapes
Mode 3
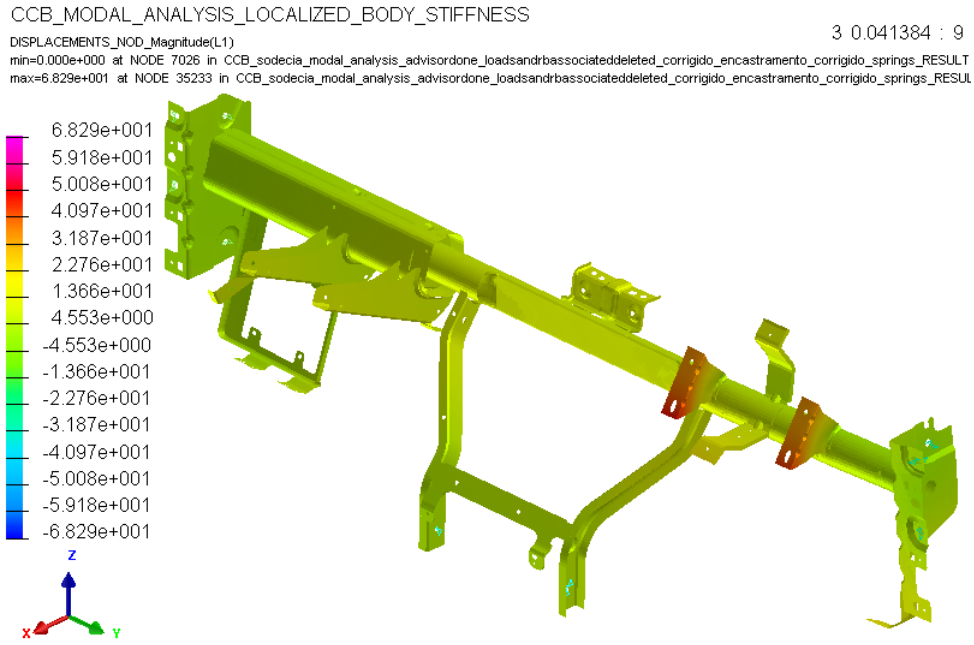
Mode 4
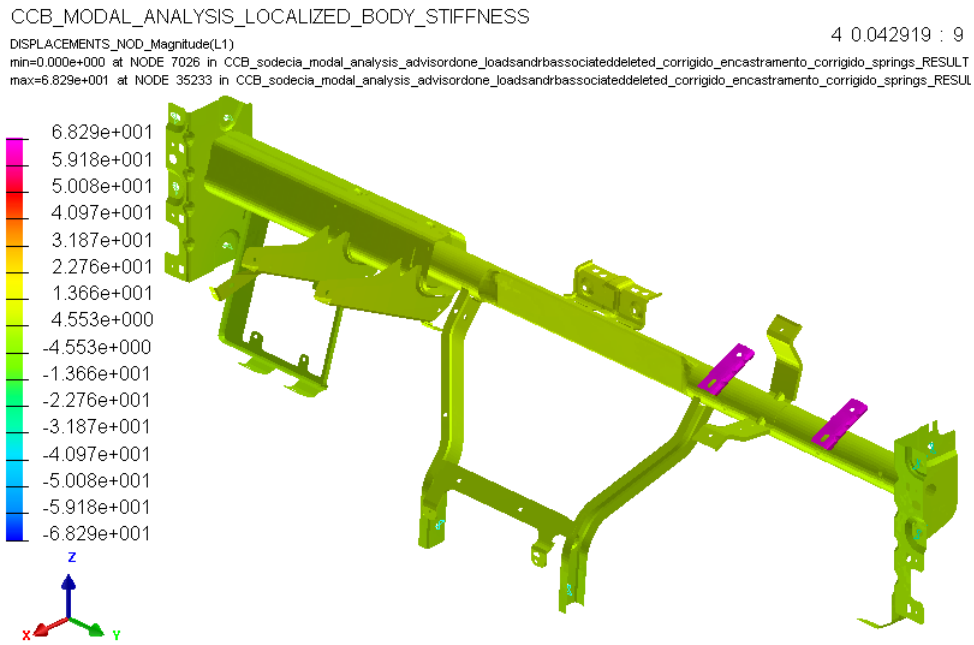

Table 6.3: CCB model with fixed boundary conditions first two modal shapes.

CCB with fixed boundary conditions modal shapes
Mode 1
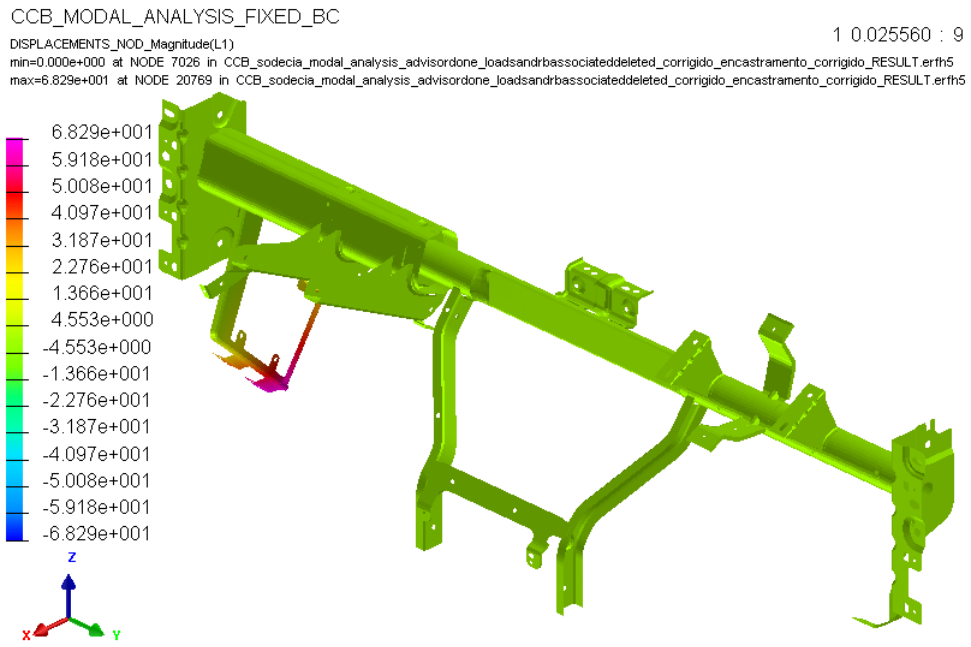
Mode 2
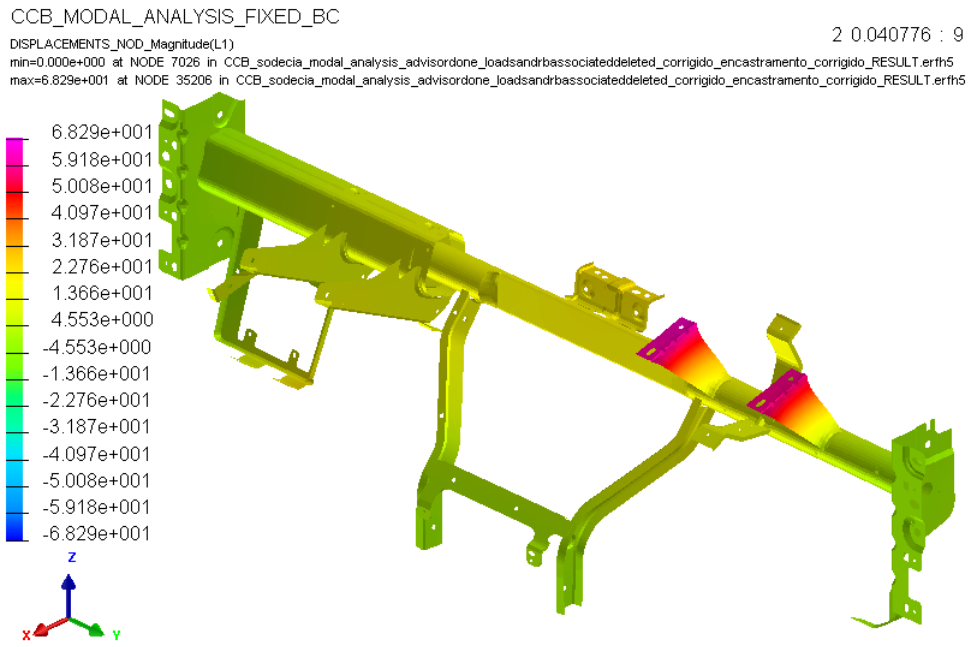

Table 6.4: CCB model with fixed boundary conditions third and fourth modal shapes.

CCB with fixed boundary conditions modal shapes
Mode 3
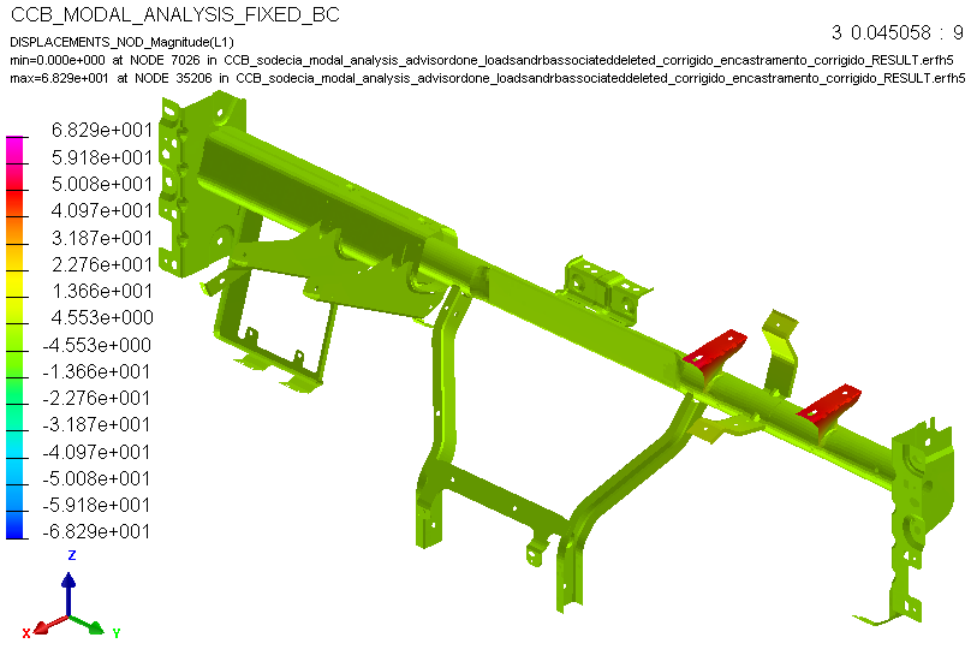
Mode 4
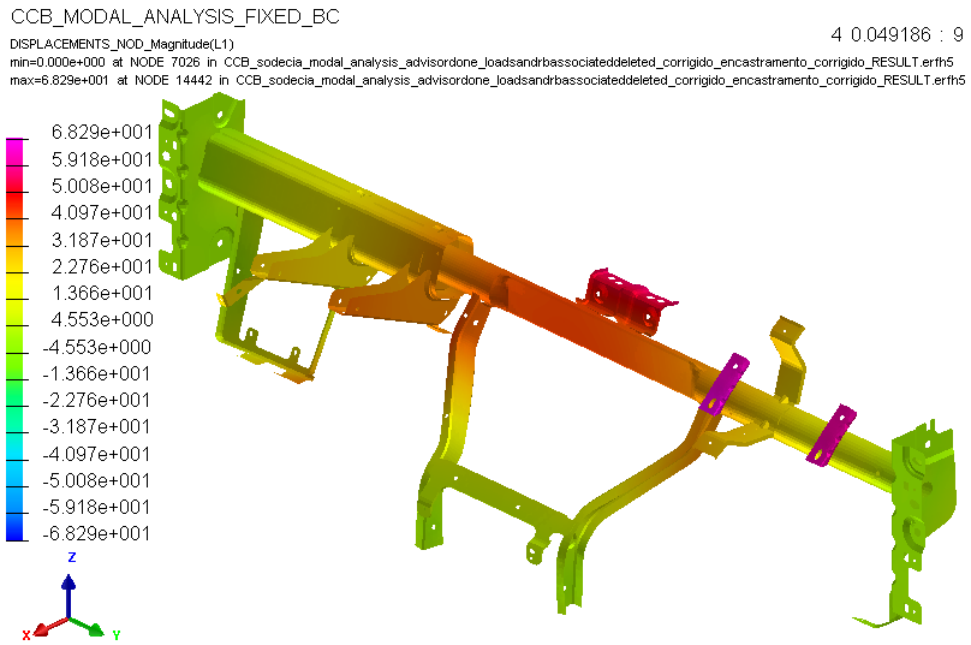

completely the natural frequences and modal shapes apart from the first mode that is not influenced by the CCB boundary conditions. Concerning the results from the model with localized stiffness, steering column first natural frequency computed is very close the design target with a percent error of 5.09%. The other requirement is completely achieved as the first CCB mode is separated from the first steering column mode by 5.357 *Hz*. These results attest the good quality of this modal analysis modeling.

Concluding remarks and suggestions for future work

In conclusion:

- There were no published results of technical studies concerning the crash behaviour of the present BV226 CCB model. In these circumtances the author adapted loadings specified for CCBs of vehicles of the same category. Using those loads in the present CCB, the crash behaviour identified was within the expected range, particulary as concerns displacements. The lack of available comparable data precludes direct comparison of von Mises equivalent stress and maximum plastic strains. Nevertheless, the present simulation of crash behaviour correctly identified the stress concentration areas as well as the points where material rupture is predicted. This results enphasize the need for validation of numerical simulations with experimental testing, to be carried out in a later stage of the R&D project of which the present work is an initial stage;
- As regards modal analyses, relevant for NVH, the present results are within the expected range for this type of product, *i.e.* the first steering column natural frequency has a 5.09% error relatively to the design target present in Ford technical specifications. Furthermore, the first CCB mode is separated from the first steering column mode by 5.357 *Hz.* According to Ford technical specifications, this value should be at least 5 *Hz,* thus confirming the quality of the present simulation;
- Although the main work presented is based on PAM-CRASH, the preliminarly work with Abaqus showed the wide applicability of that software, by comparison with the narrower scope of use of PAM-CRASH;
- The use of PAM-CRASH illustrated the importance of a good quality mesh for preventing subsequent difficulties with crash analysis, particulary as regards the time step stability over the full body mesh;
- The present work is further confirmation of the interest of numerical modeling as a first step before actual experimental testing, saving time and money;
- The present work suggests that the capability to model the crash behaviour of automotive structures subjected to time-dependent loads was indeed achieved. This capability is available, at the moment, to deal with any boundary conditions that might be of interest for car manufacturers.

Future works:

- Tune the FE model for crash simulation, aiming at identify the maximum magnitude of some load vectors that the CCB can sustain;
- Consider the behaviour of the CCB within a complete BIW crash simulation. This raises the need for another type of crash simulation. Instead of time dependent loads, the simulation will consist of evaluating the impact of complete BIW with a given initial speed against a rigid body;
- Incorporate in the model the residual stress system resulting from welding processes, and take into account the distortion originated by those processes;
- Improved constitutive laws of the relevant materials in the simulations.

References

[1] F. Volart and S. Faria. GESTAMP, Cross car beam optimization, ppt presentation, Dynamore Forum 2012.

[2] R&D - Cross-Car Beam 360º, ppt presentation, SODECIA.

[3] H. Cheong. Setting the euroncap facts straight, July 2012, http://www.cbt.com.my/2012/07/03/setting-the-euroncap-facts-straight/.

[4] EuroNCAP. Frontal impact, 2013, http://www.euroncap.com/tests/frontimpact.aspx.

[5] Insurance Institute for Highway Safety and Highway Loss Data Institute. Frontal crash test: moderate overlap and small overlap, 2013, http://www.iihs.org/ratings/frontal_test_info.html.

[6] EuroNCAP. Pole side impact, 2013, http://www.euroncap.com/Content-Web-Page/90769bbc-bb74-4129-a046-e586550c3ece/pole-side-impact.aspx.

[7] EuroNCAP. Car to car side impact, 2013, http://www.euroncap.com/Content-Web-Page/106f41f7-d486-46bf-bfbc-80fb4c79f679/car-to-car-side-impact.aspx.

[8] I. Wright. Universidade do Porto Visual/VPS Training. Technical report, ESI Group, April 2012.

[9] G. A. Keoleian. Is environmental improvement in automotive component design highly constrained? *Journal of Industrial Ecology*, 2(2):103–118, 1998.

[10] J. C. Brown, A. J. Robertson, and S. T. Serpento. *Motor vehicle structures: concepts and fundamentals*. Butterworth-Heinemann, 2002.

[11] P. Duysinx. Conception et analyse structurale des chassis, Université de Liège, Année académique 2011-2012, ppt presentation.

[12] K. McLean. Chevrolet Sonic, ppt presentation at: Great Designs in Steel Seminar, May 17, 2013, available in www.autosteel.org.

[13] H. E. Friedrich and B. L. Mordike. *Magnesium Technology: Metallurgy, Design Data, Applications*. Springer, 2006.

[14] N. Li, X. Chen, T. Hubbert, and R. Berkmortel. 2005 Ford GT magnesium instrument panel cross car beam. *SAE paper 2005-01-0341*.

[15] C. Hartl. Research and advances in fundamentals and industrial applications of hydroforming. *Journal of Materials Processing Technology*, 167:383–392, 2005.

[16] J. Killing, B. W. Surgenor, and C. K. Mechefske. A machine vision system for the detection of missing fasteners on steel stampings. *The International Journal of Advanced Manufacturing Technology*, 41(7-8):808–819, 2009.

[17] ESI Group. *Virtual Performance Solution 2012, Solver Reference Manual, Volume I, General Simulation Procedure*. ESI Group, June 2012.

[18] D. Broek. *Elementary engineering fracture mechanics*. Martinus Nijhoff Publishers, 1982.

[19] S. P. Timoshenko and J. N. Goodier. *Theory of elasticity*. McGraw-Hill Kogakusha, Ltd., Tokyo, 3rd edition, 1970.

[20] P. K. Mallick, editor. *Materials, design and manufacturing for lightweight vehicles*. CRC and Woodhead Publishing Limited, 2010.

[21] C. D. Horvarth. *Materials, design and manufacturing for lightweight vehicles*, chapter 2: Advanced steels for lightweight automotive structures, pages 35–78. CRC and Woodhead Publishing Limited, 2010.

[22] Specifiche di modellazione f.e.m. per carrozzeria. Technical Specification C2301, Fiat Auto, January 2003.

[23] W. Johnson and A. G. Mamalis. *Crashworthiness of vehicles*. Mechanical engineering Publications Ltd, London, 1978.

[24] Insurance Institute for Highway Safety and Highway Loss Data Institute. Side crash test program, 2013, `http://www.iihs.org/ratings/side_test_info.html`.

[25] Insurance Institute for Highway Safety and Highway Loss Data Institute. Procedures for rating roof strength, 2013, `http://www.iihs.org/ratings/roof/information.html`.

[26] ESI Group. Crash, impact and safety, June 2013, `http://www.esi-group.com/products/crash-impact-safety/pam-crash`.

[27] SODECIA. About us, 2013, `http://www.sodecia.com/en/group`.

[28] G. Slik. Evolution of structural instrument panels. *SAE paper 2002-01-1270*.

[29] A. Deb. *Materials, design and manufacturing for lightweight vehicles*, chapter Crashworthiness design issues for lightweight vehicles, Chapter 10, pages 332–356. CRC and Woodhead Publishing Limited, 2010.

[30] K. P. Lam, K. Behdinan, and W. L. Cleghorn. A material and gauge thickness sensitivity analysis on the NVH and crashworthiness of automotive instrument panel support. *Thin-Walled Structures*, 41(11):1005–1018, 2003.

[31] S. Tabacu, I. Tabacu, and A. Hadar. Computational modelling of vehicle interior components for impact applications: Thickness analysis. *International Journal of Crashworthiness*, 16(4):421–438, 2011.

[32] D. A. Ardayfio. Principles and practices of design innovation. *Technological Forecasting and Social Change*, 64:155–169, 2000.

[33] P. R. Frise. *Advances in Integrated Design and Manufacturing in Mechanical Engineering*, chapter Integrating design and manufacturing processes in automotive suppliers, pages 227–242. Springer, 2005.

[34] J. Baumeister, J. Banhart, and M. Web. Aluminium foams for transport industry. *Materials & Design*, 18(4/6):217–220, 1997.

[35] K. Y. G. McCullough, N. A. Fleck, and M. F. Ashby. The stress-life fatigue behaviour of aluminium alloy foams. *Fatigue and Fracture of Engineering Materials and Structures*, 23(3):199–208, 2000.

[36] L. Lorenzo and H. Koelman. Instrument panel weight reduction via structural optimization. *SAE paper 982936 E*, 1998.

[37] Y. Hu, X. Liu, C. E. Neal-Sturgess, and C. Y. Jianga. Lower leg injury simulation for euroncap compliance. *International Journal of Crashworthiness*, 16(3):275–284, June 2011.

[38] Reinforced Plastics, June 1997, p.6.

[39] L. F. M. Silva, A. Öchsner, and R. D. Adams, editors. *Handbook of adhesion technology*. Springer, 2011.

[40] P. M.G. P. Moreira, L. F. M. da Silva, and P. M. S. T. de Castro, editors. *Structural connections for lightweight metallic structures*. Springer, 2012.

[41] P. Camanho and L. Tong, editors. *Composite joints and connections: Principles, modelling and testing*. Woodhead, 2011.

[42] G. Sauer. *Extrusion*, chapter 2: Extruded products, pages 9–58. ASM International, 2006.

[43] A. A. Luo and A. K. Sachdev. *Advances in wrought magnesium alloys - Fundamentals of processing, properties and applications*, chapter 12: Applications of magnesium alloys in automotive engineering, pages 423–426. Woodhead Publishing Limited, 2012.

[44] R. S. Beals, C. Tissington, X. Zhang, K. Kainer, J. Petrillo, M. Verbrugge, and M. Pekguleryuz. Magnesium global development: outcomes from the TMS 2007 annual meeting. *JOM*, pages 39–42, August 2207.

[45] G. Byrne, D. Dornfeld, and B. Denkena. Advancing cutting technology. *CIRP Annals-Manufacturing Technology*, 52(2):483–507, 2003.

[46] S. Xu, W. R. Tyson, R. Bouchard, and V. Y. Gertsman. Effects of strain rate and temperature on tensile flow behavior and energy absorption of extruded magnesium am30 alloy. *Journal of Materials Engineering and Performance*, 18(8):1091–1101, 2009.

[47] D. A. Steenkamer and J. L. Sullivan. The performance of calcium carbonate filled, random fiber composites. *Polymer Composites*, 20(3):392–405, 1999.

[48] D. Mann, J. C. Van den Bos, and A. Way. *Automotive plastics and composites: worldwide markets and trends to 2007*. Elsevier, 2nd edition, 1999.

[49] Reinforced Plastics, November 2000, pp.24-27.

[50] Not just another road trip. Reinforced Plastics, Sept-Oct. 2011, pp.18-23.

[51] R. Maruthayppan, P. Balakrishnan, V. Gupta, and A. W. Chan. Comparison of thermoplastic composite vs. conventional-steel instrument panel systems for side-impact energy management. *SAE paper 980962*, 1998.

[52] K. Kendall, C. Mangin, and E. Ortiz. Discrete event simulation and cost analysis for manufacturing optimisation of an automotive lcm component. *Composites Part A: Applied Science and Manufacturing*, 29(7):711–720, 1998.

[53] A. Kocańda and H. Sadłowska. Automotive component development by means of hydroforming. *Archives of Civil and Mechanical Engineering*, 8(3):55–72, 2008.

[54] M. H. Parsa and P. Darbandi. Experimental and numerical analyses of sheet hydroforming process for production of an automobile body part. *Journal of Materials Processing Technology*, 198(1):381–390, 2008.

[55] D. Havrilla. TRUMPF. Laser based manufacturing in the automotive industry, ppt presentation, University of Virginia - November 2010.

[56] J. Sun, Q. Sun, and B. W. Surgenor. An adaptable automated visual inspection scheme through online learning. *The International Journal of Advanced Manufacturing Technology*, 59(5-8):655–667, 2012.

[57] S. Das. *Materials, design and manufacturing for lightweight vehicles*, chapter Recycling and life cycle issues for lightweight vehicles, Chapter 9, pages 309–331. CRC and Woodhead Publishing Limited, 2010.

[58] A. Tharumarajah and P. Koltun. Improving environmental performance of magnesium instrument panels. *Resources, Conservation and Recycling*, 54(12):1189–1195, 2010.

[59] D. Doran, A. Hill, K. S. Hwang, and G. Jacob. Supply chain modularisation: cases from the french automobile industry. *International Journal of Production Economics*, 106:2–11, 2007.

[60] G. Herrigel, V. Wittke, and U. Voskamp. The process of chinese manufacturing upgrading: transitioning from unilateral to recursive mutual learning relations. *Global Strategy Journal*, 3:109–125, 2013.

[61] A. Chawla. Finite element analytical techniques and applications to techniques and applications to structural design, 2013, `http://web.iitd.ac.in/~achawla/public_html/736/9-Finite_Element_analytical_tecniques.pdf`.

[62] R. D. Cook, D. S. Malkus, M. E. Plesha, and R. J. Witt. *Concepts and Applications of Finite Element Analysis*. John Wiley and Sons, Inc., 4th edition, 2002.

[63] A. Pickett. Tutorial 1 and 2, end loaded cantilever and shell element studies. Technical report, ESI GmbH/Institute for Aircraft Design, Stuttgart, November 2007, http://www.ifb.uni-stuttgart.de/FEM/PDF_FILES/Tutorial1-2_ElasticCantilever_V4.pdf.

[64] O. C. Zienkiewicz, R.L. Taylor, and J.Z. Zhu. *The Finite Element Method: Its basis and fundamentals*. Elsevier, sixth edition, 2005.

[65] T. J. R. Hughes. *The finite element method: linear static and dynamic finite element analysis*. Prentice-Hall international editions, 1987.

[66] K.-J. Bathe. *Finite element procedures*. Prentice-Hall international editions, 1996.

[67] TWI. What is reduced integration in the context of finite element analysis?: frequently asked questions, 2013, http://www.twi.co.uk/technical-knowledge/faqs/structural-integrity-faqs/faq-what-is-reduced-integration-in-the-context-of-finite-element-analysis/.

[68] LS-DYNA support. Hourglass, 2013, http://www.dynasupport.com/howtos/element/hourglass.

[69] ESI Group. *Virtual Performance Solution 2012, Solver Reference Manual, Volume II, Core Modeling*. ESI Group, June 2012.

[70] L. Swiercz. Abaqus frequency tutorial, October 2009, http://www.youtube.com/watch?v=tQsmgVsfKfw.

[71] Dassault Systèmes. *Abaqus 6.11 Online Documentation*, April 20011.

[72] K. Nazir. Abaqus tutorial - part 2: Modelling a masonry wall under a blast explosion, April 2012, http://www.youtube.com/watch?v=5Us4zLLuzgA.

[73] G. Irwin. Analysis of stresses and strains near the end of a crack traversing a plate. *Journal of Applied Mechanics*, 24:361–364, September 1957.

[74] W. F. Brown and J. E. Srawley. *Plane strain crack toughness testing of high strength metallic materials*. ASTM STP 410, American Society For Testing and Materials, 1966.

[75] A. Pickett. Tutorial and material calibration examples for PAM-CRASH, PAM-FORM and PAM-OPT, January 2013, http://www.ifb.uni-stuttgart.de/FEM/TutorialsAndMaterialCalibration.htm.

[76] F. T. Dias, J. P. da Cruz, R. A. F. Valente, and R. J. A. de Sousa. *Método dos elementos finitos: técnicas de simulação numérica em engenharia*. Edições Técnicas e Profissionais, Fevereiro 2010.

[77] Cahier des charges: specifications dimensionnement crash et vibratoire traverse poste de conduite b95. Technical report, Normalisation Renault Automobiles, March 2006.

[78] J. P. Webb. System design specification: instrument panel and console subsystem. Technical report, Ford Motor Company, July 2004.

Appendix 1

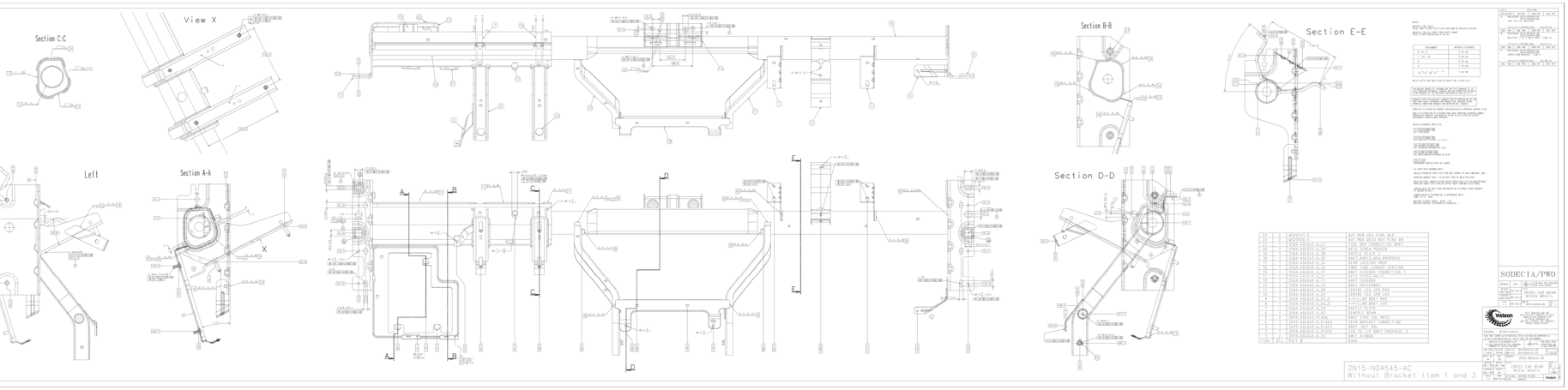

ITEM NAME	MATERIAL THICKNESS
A, B, C	5.0 mm
D, E, F, G	4.00 mm
H	3.00 mm
I	2.50 mm
J, K, L, M, N, O, P, Q	1.90 mm

ITEM	QTY	PART #	DESCRIPTION
17	1	W0220125.5	NUT M20 PETERS NUT
16	1	W0220125.5	NUT M20 WELD NUT WING SR
15	1	1564-4043A15-A-01	SIDE RAIL CONNECTING BRACE
14	1	1564-4043A15-A-06	WELD STAKA MOUNTS
13	1	1564-4043A15-A-05	BODY MOUNTING
12	1	1564-4043A15-A-04	BODY CROSS MEMBER(PROFILE)
11	1	1564-4043A15-A-03	BEAM ISOLATOR PAPER
10	1	1564-4043A15-A-02	SIDE RAIL CHOICE VERSION
9	1	1564-4043A15-A-01	BODY FIXINGS CONNECTING 1
8	1	1564-4043A15-A-07	BODY FIXINGS
7	1	1564-4043A15-A-08	BODY FIXINGS 2
6	1	1564-4043A15-A-09	BODY HEATERBOX
5	1	1564-4043A15-A-10	A-PILLAR BRC LHS
4	1	1564-4043A15-A-11	HEATER SIDE RAIL LHS
3	1	1564-4043A15-A-12	A-PILLAR BRC RHS
2	1	1564-4043A15-A-13	REPEAT PLATE
1	1	1564-4043A15-A-14	HEATER SIDE RAIL RHS
8	1	2N15-N04545-AA	BODY STRAP TO FRAME - PNTD
7	1	2N15-N04545-A_PAGE	SKIN BRACKET CONNECTING
6	1	2N15-N04545-A_PAGE	BODY FIXINGS
5	1	2N15-N04545-A_PAGE	SIDE TO TOP BODY PROVISIONS_2
4	1	2N15-N04545-AA	BODY LOCKERS
3	1	2N15-N04545-AA	BODY

2N15-N04545-AC
Without Bracket Item 1 and 3

SODEC1A/PWO

FRONT CAB REAR WIDER BRACES

2N15-N04545-AC